LAWRENCE
LIVERMORE
NATIONAL
LABORATORY

UCRL-TH-221547

Understanding How Femtosecond Laser Waveguide Fabrication in Glasses Works

W. J. Reichman

May 22, 2006

This work was performed under the auspices of the U.S. Department of Energy by University of California, Lawrence Livermore National Laboratory under Contract W-7405-Eng-48.

Understanding How Femtosecond Laser Waveguide Fabrication in Glasses Works

BY

Wilbur Jordan Reichman II
B.S. (University of Missouri – Rolla, Rolla, MO) 2001
M.S. (University of California – Davis, Davis, CA) 2004

DISSERTATION

Submitted in partial satisfaction for the requirements for the degree of

DOCTOR OF PHILOSOPHY

in

Applied Science

in the

OFFICE OF GRADUATE STUDIES

of the

UNIVERSITY OF CALIFORNIA

DAVIS

Approved:

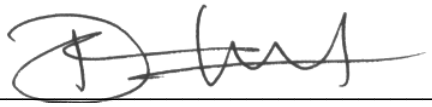

Denise M. Krol, Ph. D.

Atul N. Parikh, Ph. D.

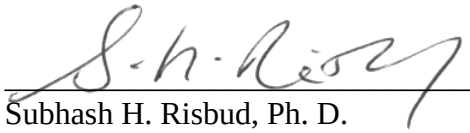

Subhash H. Risbud, Ph. D.

Committee in Charge

2006

Wilbur Jordan Reichman
June 2006
Applied Science

Understanding How Femtosecond Laser Waveguide Fabrication in Glasses Works

Abstract

In order to understand the physical processes associated with fs-laser waveguide writing in glass, the effects of the laser repetition rate, the material composition and feature size were studied. The resulting material changes were observed by collecting Raman and fluorescence spectra with a confocal microscope. The guiding behavior of the waveguides was evaluated by measuring near field laser coupling profiles in combination with white light microscopy.

Waveguides and Bragg gratings were fabricated in fused silica using pulse repetition rates from 1 kHz to 1 MHz and a wide range of scan speeds and pulse energies. Two types of fluorescence were detected in fused silica, depending on the fabrication conditions. Fluorescence from self trapped exciton ($E_{\delta}^{'}$) defects, centered at 550 nm, were dominant for conditions with low total doses, such as using a 1 kHz laser with a scan speed of 20 μm /s and pulse energies less than 1 μJ. For higher doses a broad fluorescence band, centered at 650 nm, associated with non-bridging oxygen hole center (NBOHC) defects was observed. Far fewer NBOHC defects were formed with the 1 MHz laser than with the kHz lasers possibly due to annealing of the defects during writing. We

also observed an increase in the intensity of the 605 cm^{-1} Raman peak relative to the total Raman intensity, corresponding to an increase in the concentration of 3-membered rings for all writing conditions. The magnitude of this increase in waveguides fabricated with a 1 MHz laser was nearly twice that of waveguides fabricated with a 1 kHz laser.

Additional waveguides were fabricated in soda lime silicate glasses to assess the effects of changing the glass composition. These waveguides formed around, not inside the exposed regions. This is distinctly different from fused silica in which the waveguides are inside the exposed regions.

A comprehensive analysis of all the experimental results indicates that good waveguides are formed below the actual damage threshold of the glass. The rapid quenching model, which correlates the refractive index of the modified material to its cooling rate, explains the effect of composition on waveguide behavior.

Acknowledgements

I would like to thank several people who helped me conduct the research presented in this dissertation. I would like to thank my predecessor, James Chan, for conducting the background work upon which my research is built, and for showing me the basic lab procedures required to continue his work. I would like to thank my fellow student, Francisco Rafael Leon, who assisted me in designing and finding parts for my confocal microscope system, and who could always be counted upon to come up with interesting, entertaining distractions. I would like to thank my advisor, Denise M. Krol, for the freedom she allowed me in guiding my own work, for her support in sending me to a variety of conferences, for her trust in allowing me to form and manage my own research collaborations, and for her assistance in crafting readable publications.

I would like to thank the various collaborators whose work contributed to almost every aspect of my research. Christopher Smelser and Stephen Mihailov at the Communications Research Centre Canada provided the fiber Bragg Gratings studied in chapter 4. Eric Mazur, Rafael Gattass and Prissana Thamboon at Harvard University provided the waveguides fabricated with 10 to 250 kHz repetition rate femtosecond lasers studied in chapter 5. Lawrence Shah, Fumiyo Yoshino and Alan Arai at IMRA America, Inc., and Shane Eaton and Peter Herman at the University of Toronto provided the waveguides fabricated with a 1 MHz repetition rate femtosecond laser studied in chapter 5. Alan deserves special thanks for his administrative negotiations, which

allowed us to publish these results. And, Carol Click at Schott North America, Inc. provided the soda-lime silicate glasses studied in chapter 6.

I would like to thank my “lab advisor,” Thomas Huser, who again allowed me the freedom to pursue my own research interests, and who would throw interesting supplemental research projects my way. While these projects did not contribute my dissertation, they helped keep my interest in science alive.

Finally, I would like to thank all of my friends and associates with whom I relaxed in the evenings, and who arguably helped preserve my sanity.

This work was performed under the auspices of the US Department of Energy by the University of California Lawrence Livermore National Laboratory, through M Division within Physics and Applied Technology, under contract W-7405-Eng-48, UCRL-TH-221547. Financial support was provided through National Science Foundation grant DMR - 03070.

Table of Contents

Chapter 1

Introduction

1.1 Laser induced refractive index changes in glass

Touch something in the sun and it feels warm; leave something in the sun and its color fades. These are basic observations of light affecting matter. Science works by making such observations and then asking questions. Why does something in the sun feel warm? Can the warmth of the sun be used for something?

In the early 1970s it was discovered that lasers could cause noticeable, permanent refractive index changes in glass; or more simply put, the laser could make a spot [1.1]. Hill et al. used this "photoinduced" change for optical device fabrication. In 1978 his group demonstrated that a blue laser could be employed to fabricate Bragg grating reflectors inside glass fibers [1.2]. Further studies by Garside et al. [1.3-1.4], explained that this refractive index change was induced by a nonlinear absorption process, in which two blue photons are absorbed simultaneously. Unfortunately, the two photon process was not practical for industrial scale device fabrication.

It was theorized that the linear absorption of a UV laser source could be used to alter the glass more efficiently. The linear absorption of a UV laser is possible because a single UV photon has the same energy as two blue photons. The experimental confirmation of

this theory by Meltz et. al. in 1989 [1.5] opened the door to using photoinduced refractive index changes for practical device fabrication. However, strong laser absorption was required for the process to work, limiting its initial applicability to certain doped glasses. As a result research efforts evolved to develop new UV lasers that could affect existing glasses; and to develop new photosensitive, doped glasses that would absorb existing lasers.

1.2 Femtosecond laser induced refractive index changes

The development of femtosecond lasers in the 1990s provided a method to induce refractive index changes in most glasses, including undoped glasses. A femtosecond (fs) pulsed laser has pulses that are orders of magnitude shorter than conventional lasers, only lasting 10s or 100s of femtoseconds (10^{-15} s). These pulses have very high peak intensities, with relatively low energies. This combination allows for efficient highly nonlinear processing, in which several near-infrared photons are absorbed simultaneously to modify a glass. Nonlinear, femtosecond laser processing has three important advantages compared with linear, UV laser processing: It creates less collateral damage. It can be used to fabricate devices inside bulk materials. And as mentioned earlier, it works in most glasses.

1.2.1 Device fabrication

Waveguides were the first optical device fabricated using femtosecond laser induced refractive index changes [1.6]. A waveguide, sketched in figure 1.1, is a simple device, which causes light to follow a set path and prevents the light from spreading out as it travels. The successful creation of waveguides demonstrated the viability of femtosecond laser writing as a technique for fabricating optical devices. Many research groups subsequently used femtosecond writing to produce a wide variety of optical components that can be incorporated into integrated optical devices [1.7-1.14]. These include several types of splitters [1.8,1.9] and couplers [1.10] that can be used to separate and combine beams of light; Bragg gratings [1.11] that serve as mirrors for specific colors of light;

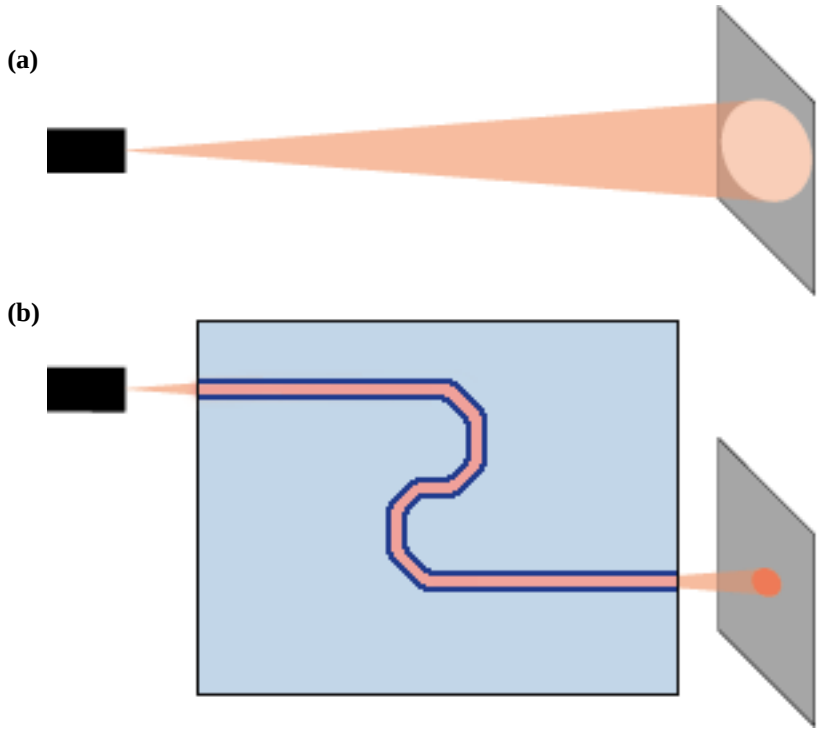

Figure 1.1 A cartoon of a) a light in air, and b) the same light passing through a waveguide. The waveguide is outlined in dark blue.

amplifiers [1.13] that increase the intensity of light passing through them; and lasers [1.7, 1.14] that generate coherent light for use in a variety of applications. Most of these devices were manufactured using two-dimensional configurations identical to devices manufactured on material surfaces with conventional techniques. However, Nolte et al. took advantage of the ability of femtosecond processing to fabricate devices inside bulk materials to create a three-dimensional, 3-way splitter [1.12]. This achievement exemplifies the potential of femtosecond waveguide writing to produce novel architectures that could be used to increase the efficiency of existing devices, or to create entirely new devices.

1.3 Understanding the refractive index change

Despite this success in fabricating various devices using a femtosecond laser, the underlying mechanisms of how the refractive index change is induced are still uncertain. And, more questions continue to arise as people study the effects of different materials and lasers upon the modification process. This section provides a brief overview of the current theory and its problems. Chapter 2 provides a more detailed technical discussion.

The mechanisms of femtosecond laser induced refractive index changes are normally divided into two processes: energy absorption and energy dissipation. The energy absorption process has been fairly well characterized through a series of fs laser surface ablation studies [1.15-1.19]. A combination of multiphoton absorption and avalanche photoionization result in highly localized absorption of the femtosecond laser. If enough

energy is absorbed, the energy density will reach a critical threshold after which a plasma forms within the exposed region.

The energy dissipation process is less well understood. This uncertainty arises because studying the tiny modified regions inside bulk glasses is akin to hunting for a needle in a haystack, difficult but not impossible if one has the correct tools. A few techniques, including confocal spectroscopy which was vital for most of my research as described in chapter 3, are capable of detecting changes within the micron scale modified regions inside centimeter blocks of glass. From this information a rough picture of the energy dissipation process has begun to emerge. It is likely that energy dissipates through a combination of thermal diffusion and shock wave generation [1.20], but it is uncertain which process is dominant and how long the processes take. In either case, the end result is a localized refractive index change.

It was originally proposed that the results of femtosecond laser modification would be the same in any optical glass. This assumption was based on early results which showed that femtosecond lasers could modify every glass tested [1.6]; and it was already known that the results for femtosecond laser ablation were similar for most glasses. Earlier work in our group rebutted this belief. Specifically, it was found that waveguides written in a phosphate glass (IOG-1), have different guiding characteristics than those written in fused silica [1.21]. Waveguides written in IOG-1 appear to have a lower refractive index core surrounded by a higher refractive index shell; in contrast the waveguides written in fused silica appear to have a higher refractive index core. Our group proposed that these

different behaviors are determined by the relationship between the cooling rate used to produce the glass and the resulting density of the glass. However, IOG-1 and fused silica belong to drastically different glass systems, between which too many material properties change to draw firm conclusions about the validity of our explanation. Confirming this explanation would facilitate the fabrication of devices in diverse, application specific glasses.

More questions have arisen from recent studies which have shown that the pulse repetition rate of the laser has a substantial effect on the femtosecond laser writing process [1.22-1.24]. Traditionally, amplified fs lasers with kilohertz repetition rates have been used for fs device fabrication because oscillators did not have sufficient peak intensities. However, the development of high pulse energy oscillators and other high repetition rate fs sources that operate with megahertz repetition rates have overcome this barrier. Several differences have been reported when using MHz instead of kHz repetition rate lasers to fabricate devices. These include the formation of a spherical modified region that extends beyond the focal volume of the laser due to thermal diffusion and heat accumulation [1.22-1.23], and a potentially greater refractive index modification [1.24]. Additionally, it has been observed that megahertz systems provide better quality waveguides in some glasses, while kilohertz systems work better in others.

1.4 Project Summary

The objective of my dissertation is to further explore how femtosecond laser modification of glasses works. Specifically, it focuses on using spectroscopic tools to analyze the effects of pulse repetition rate and glass composition on the writing process. This information will facilitate the creation of new devices using femtosecond laser writing. The dissertation is divided into eight chapters.

Chapter 2 provides detailed background information on the mechanics and mechanisms of femtosecond waveguide fabrication; and on the spectroscopic characterization of femtosecond laser modified glass.

Chapter 3 describes the equipment and procedures we used to fabricate and analyze waveguides and other devices.

Chapter 4 contains high spatial resolution, spectral analyses of structural modifications caused by femtosecond laser waveguide fabrication. Individual waveguides and more complex devices with micron scale features were studied.

Chapter 5 describes a spectroscopic comparison between waveguides fabricated in fused silica using different laser repetition rates to determine the effects of pulse repetition rate on the modification process.

Chapter 6 compares waveguides fabricated in fused silica and soda-lime-silicate glasses. Studying these similar glasses allows us to assess which glass properties relate to the material dependent effects of femtosecond laser modification.

Chapter 7 discusses a revised model of the femtosecond laser waveguide writing process based on the results described in chapters 4-6.

Finally, Chapter 8 provides a summary of the work described in this thesis.

Parts of this dissertation have been or will be published in several journal and conference articles listed below:

- W. Reichman, J. W. Chan and D. M. Krol, "Confocal fluorescence and Raman microscopy of femtosecond laser-modified fused silica," *Journal of Physics: Condensed Matter*, **15**, pp. S2447–S2456, (2003).

- W. J. Reichman, C. A. Click, D. M. Krol, "Fabrication of Waveguides in Sodium Silicate Glasses Using Ultrafast Laser Pulses," *Proceedings of the International Society for Optical Engineering (SPIE)*, Photonics West, San Jose, CA, 2005.

- W. J. Reichman, D. M. Krol, C. W. Smelser, S. J. Mihailov, "Fluorescence Spectroscopy of Fiber Gratings Written with an Ultrafast Infrared Laser and a Phase Mask" *Proceeding of the Conference on Lasers and Electro-Optics (CLEO)*, Baltimore, MD, 2005.

- W. J. Reichman, D. M. Krol, L. Shah, F. Yoshino, A. Arai, S. M. Eaton, and P. R. Herman, "A Spectroscopic Comparison of Femtosecond Laser Modified Fused Silica using kHz and MHz Laser Systems," *Journal of Applied Physics*, accepted, in press.

References

1.1 R. F. Kydd and F. J. Bryant, "Photosensitivity of Cadmium Telluride," *Physica Status Solidi A-Applied Research* **23**(1), pp. K49-K54, (1974).

1.2 K. O. Hill, Y. Fujii, D. C. Johnson and B. S. Kawasaki, "Photosensitivity in Optical Fiber Waveguides - Application to Reflection Filter Fabrication," *Applied Physics Letters* **32**(10), pp. 647-649, (1978).

1.3 D. K. W. Lam and B. K. Garside, "Characterization of single-mode optical fiber filters," *Applied Optics*, **20**(3), pp. 440-445, (1981).

1.4 K. O. Hill, "Photosensitivity in Optical Fiber Waveguides: From Discovery to Commercialization," *IEEE Journal On Selected Topics In Quantum Electronics*, **6**(6), pp. 1186-1189, (2000).

1.5 G. Meltz, W. W. Morey, and W. H. Glenn, "Formation of Bragg gratings in optical fibers by a transverse holographic method," *Optics Letters*, **14**(15), pp. 823–825, (1989).

1.6 K. M. Davis, K. Miura, N. Sugimoto and K. Hirao, "Writing waveguides in glass with a femtosecond laser" *Optics Letters*, **21**(21), pp. 1729-1731, (1996).

1.7 R. Osellame, S. Taccheo, M. Marangoni, R. Ramponi and P. Laporta, "Femtosecond writing of active optical waveguides with astigmaticaly shaped beams." *Journal of the Optical Society of America B*, **20**(7), pp. 1559-1567, (2003).

1.8 D. Homoelle, S. Wielandy, A. L. Gaeta, N. F. Borrelli and C. Smith, "Infrared photosensitivity in silica glasses exposed to femtosecond laser pulses" *Optics Letters* **24**(18), pp. 1311-1313, (1999).

1.9 K. Minoshima, A. M. Kowalevicz, I. Hartl, E. P. Ippen and J. G. Fujimoto, "Photonic device fabrication in glass by use of nonlinear materials processing with a femtosecond laser oscillator" *Optics Letters* **26**(19), pp. 1516-1518, (2001).

1.10 A. M. Streltsov and N. F. Borrelli, "Fabrication and analysis of a directional coupler written in glass by nanojoule femtosecond laser pulses" *Optics Letters* **26**(1), pp. 42-43, (2001).

1.11 Y. Kondo, K. Nouchi, T. Mitsuyu, M. Watanabe, P. G. Kazansky and K. Hirao, "Fabrication of long-period fiber gratings by focused irradiation of infrared femtosecond laser pulses" *Optics Letters* **24**(10), pp. 646-648, (1999).

1.12 S. Nolte, M. Will, J. Burghoff and A. Tuennermann, "Femtosecond Waveguide writing: a new avenue to three-dimensional integrated optics" *Applied Physics A* **77**, pp. 109-111, (2003).

1.13 Y. Sikorski, A. A. Said, P. Bado, R. Maynard, C. Florea and K. A. Winick, "Optical waveguide amplifier in Nd-doped glass written with near-IR femtosecond laser pulses" *Electronics Letters* **36**(3), pp. 226-227, (2000).

1.14 S. Taccheo, G. Della Valle, R. Osellame, G. Cerullo, N. Chiodo, P. Laporta, and O. Svelto, "Er:Yb-doped waveguide laser fabricated by femtosecond laser pulses." *Optics Letters*, **29**(22), pp. 2626-2628, (2004).

1.15 S. C. Jones, P. Braunlich, R. T. Casper, X. A. Shen and P. Kelly, "Recent progress on laser-induced modifications and intrinsic bulk damage of wide-gap optical-materials," *Optical Engineering*, **28**, pp. 1039–1068, (1989).

1.16 X. Liu, D. Du, and G. Mourou, "Laser Ablation and Micromachining with Ultrashort Laser Pulses," *IEEE Journal of Quantum Electronics*, **33**(10), pp. 1706-1716, (1997).

1.17 C. B. Schaffer, A. Brodeur and E. Mazur, "Laser-induced breakdown and damage in bulk transparent materials induced by tightly focused femtosecond laser pulses," *Measurement Science and Technology*, **12** 1784–1794, (2001).

1.18 B. C. Stuart, M. D. Feit, S. Herman, A. M. Rubenchik, B. W. Shore and M. D. Perry, "Nanosecond-to-femtosecond laser-induced breakdown in dielectrics," *Physics Review* B, **53**(4), pp. 1749–61, (1996).

1.19 D. Du, X. Liu, G. Korn, J. Squier and G. Mourou, "Laser-induced breakdown by impact ionization in SiO_2 with pulse widths from 7 ns to 150 fs," *Applied Physics Letters*, **64**(23), pp. 3071–3073, (1994).

1.20 E. N. Glezer and E. Mazur, "Ultrafast-laser driven micro-explosions in transparent materials," *Applied Physics Letters*, **71**(7)**,** pp. 882–884, (1997).

1.21 J. W. Chan, T. R. Huser, S. H. Risbud and D. M. Krol, "Waveguide fabrication in phosphate glasses using femtosecond laser pulses," *Applied Physics Letters*, **82**(15)**,** pp. 2371-2373, (2003).

1.22 C. B. Schaffer, A. Brodeur, J. F. Garcia and E. Mazur, "Micromachining bulk glass by use of femtosecond laser pulses with nonojoule energy," *Optics Letters*, **26**(2), pp. 93-95, (2001).

1.23 R. Osellame, N. Chiodo, V. Maselli, A. Yin, M. Zavelani-Rossi, G. Cerullo, P. Laporta, L. Aiello, S. De Nicola, P. Ferraro, A. Finizo and G. Pierattini, "Optical properties of waveguides written by a 26 MHz stretched cavity Ti:sapphire femtosecond oscillator," *Optics Express*, **13**(2), pp. 612-620, (2005).

1.24 L. Shah, A. Y. Arai, S. M. Eaton, and P. R. Herman, "Waveguide writing in fused silica with a femtosecond fiber laser at 522 nm and 1 MHz repetition rate," *Optics Express*, **13**(6) 1999-2006, (2005).

Chapter 2

Background on Waveguide Fabrication and Characterization

2.1 Overview

This chapter begins with a description of different femtosecond (fs) laser fabrication methods, and discusses some of the advantages and disadvantages of each method. It discusses the potential modification mechanisms, including how each mechanism functions and what requirements each mechanism imposes on the modification process. The chapter concludes with an overview of how spectroscopy has been used to experimentally investigate the modification mechanisms.

2.2 Waveguide fabrication methods

Most femtosecond waveguide fabrication systems follow similar principles. A pulsed femtosecond laser is focused through a microscope objective, and a transparent sample is moved relative to the focal point to directly write devices. A very high threshold intensity must be reached to initiate the modification process, as will be discussed in section 2.3. Thus, the intensity of the laser can be adjusted such that it is only capable of modifying the glass in the focal volume of the microscope objective and passes through the rest of the transparent sample without causing any changes, as depicted in figure 2.1.

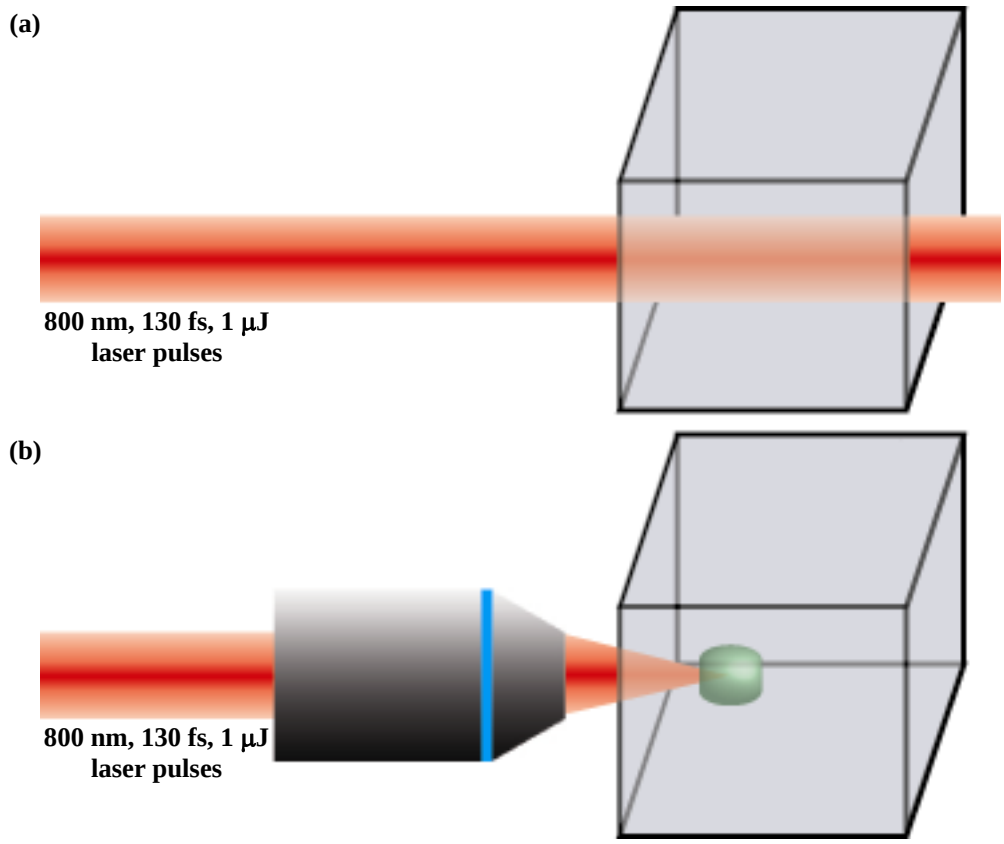

Figure 2.1 a) An unfocused femtosecond laser passes through a glass block; b) focusing the laser increases the intensity resulting in localized modification of the glass within the focal volume.

Four major variables control the femtosecond modification process in all fabrication systems: the speed and direction with which the sample is moved; the laser repetition rate; the laser wavelength; and the laser fluence. The different writing configurations discussed below vary in how they handle these variables.

2.2.1 Longitudinal and transverse writing

The direction with which the sample is moved relative to the direction of laser propagation is the defining difference between longitudinal and transverse writing. In longitudinal writing the sample is moved parallel to the direction of laser propagation; in

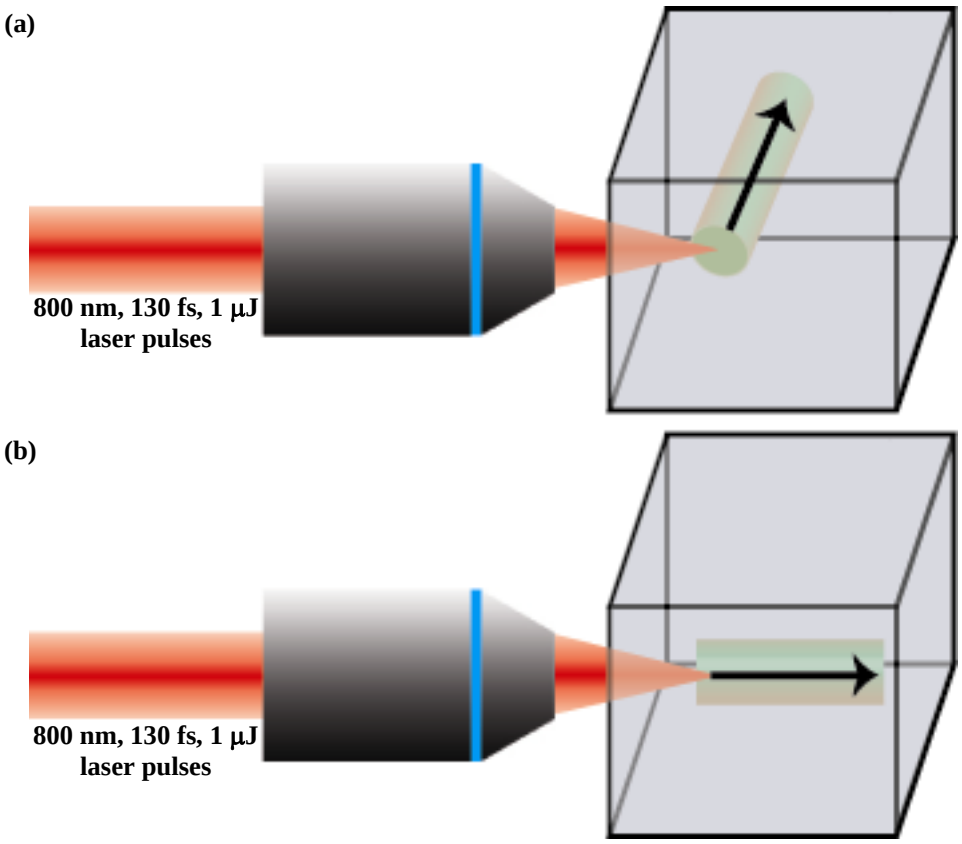

Figure 2.2 a) Transverse and b) longitudinal waveguide writing. The black arrows indicate the direction in which the sample is moved.

transverse writing the sample is moved perpendicular to the direction of laser propagation. This difference is illustrated in figure 2.2.

Femtosecond waveguide writing was initially developed using the longitudinal writing orientation. This orientation creates circular waveguides because a focused Gaussian beam is radially symmetric, as shown in figure 2.3a. However for longitudinal writing, the waveguide length is physically limited to the working distance of the microscope objective and only minor deviations from the direction of laser propagation are possible using this technique. Transverse writing was developed to overcome these limitations. It allows for arbitrary waveguide length and arbitrarily sharp turns in the plane perpendicular to the laser beam, but transversely written waveguides frequently have an

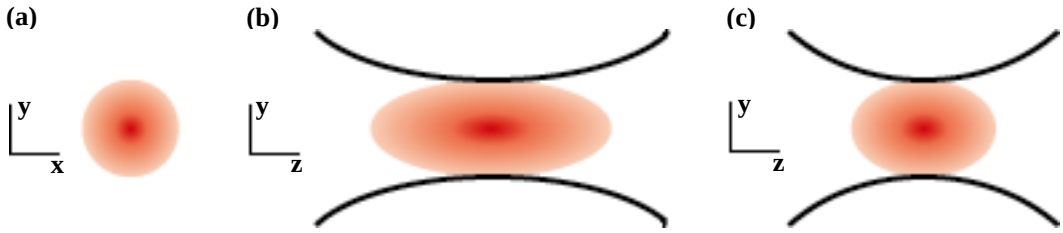

Figure 2.3 Intensity profiles of a focused Gaussian beam propagating in the z direction; in b) the beam is focused with a low NA objective, and in c) it is focused with a higher NA objective.

elliptical profile due to the elongation of a Gaussian focus, as shown in figure 2.3b. The elongation can be reduced by using very high numerical aperture (NA) objectives, as shown in figure 2.3c. The working distance of microscope objectives decreases as the NA increases, so this solution involves a tradeoff between the resulting waveguide symmetry and the depth at which devices can be fabricated. Another way to eliminate the elongation in one direction is by using a cylindrical lens to create an elliptical beam [2.1]. Unfortunately, this results in the waveguide profile having a strong dependence on the scanning direction, so it is very difficult to fabricate anything besides straight waveguides with this technique.

2.2.2 High and low repetition rate writing

The laser repetition rate is the defining characteristic between "high" and "low" repetition rate femtosecond laser writing. A functional definition of high repetition rate writing is "writing in which substantial thermal accumulation occurs between subsequent laser pulses, affecting the modification process." And, low repetition rate writing occurs whenever this statement is false. In high repetition rate writing thermal accumulation melts the glass in a sphere around the focal volume [2.2-2.3]. This leads to a circular

waveguide profile that is not dependent upon the writing direction or the exact shape of the focal spot. Several groups have also reported that high repetition rate writing causes an increase in the diameter of the modified line due to thermal diffusion and accumulation [2.2-2.5], and that it results in a greater refractive index change [2.6].

Despite the simple functional definition of high repetition rate writing, it is difficult to precisely define a repetition rate at which high repetition rate writing starts. It is often unclear what constitutes "substantial" thermal accumulation, and the boundary between high and low repetition rate writing is material dependent; varying with the heat capacity, thermal conductivity, and band gap of the glass being modified. The boundary is also affected by all of the laser writing parameters mentioned in section 2.2, further complicating efforts to form a precise definition. A working definition of what constitutes a high repetition rate is a rate greater than $1 / \tau_o$, where τ_o is the time it takes for heat to diffuse out of the focal volume. Writing with a 1 MHz system falls into the high repetition rate regime, and writing with a 1 kHz system falls within the low repetition rate regime. The differences between these regimes are studied in further detail in chapter 5.

2.2.3 Patterned writing

Patterned writing is based on carefully controlling the laser fluence to create a specific spatial pattern. In this technique the total laser intensity at every point within a sample is controlled such that modification only occurs where there are intensity peaks from

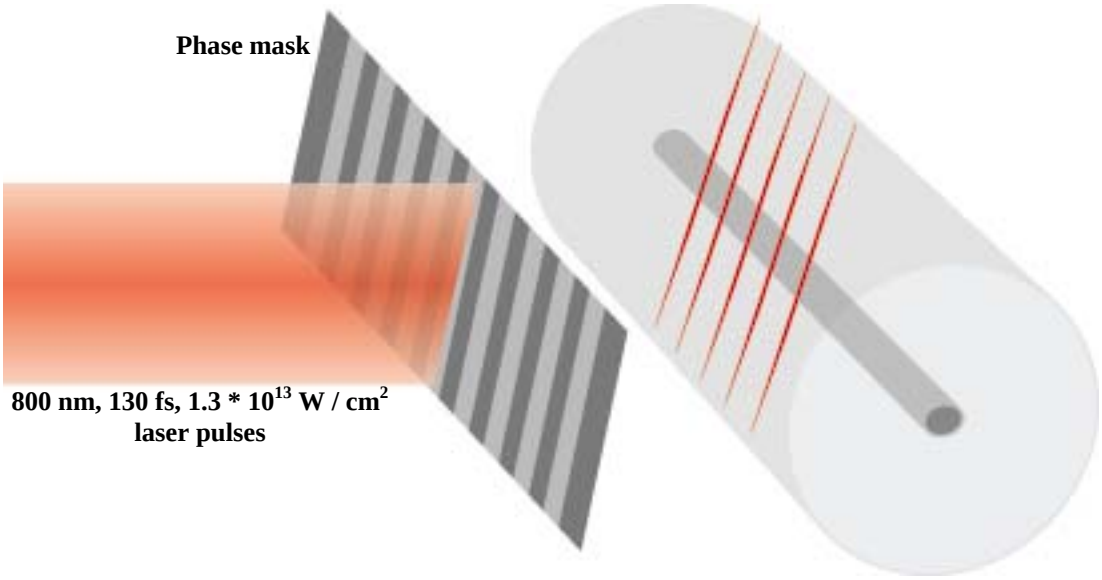

Figure 2.4 Writing setup for patterned writing. Note, that for patterned writing the average power per area is normally specified instead of the pulse energy.

multiple beams constructively interfering, or where high intensity regions are generated by a phase mask, as shown in figure 2.4. Unlike the translational writing techniques discusses so far; in patterned writing an entire pattern is formed at the same time without moving the sample [2.7-2.8]. This technique is much faster than the translational writing methods, and it is ideal for fabricating repetitive structures such as gratings or photonic crystals. However, it is very difficult to fabricate non-repetitive structures, such as point defects, using patterned writing.

2.2.4 The effects of changing the pulse fluence

Of the four variables used to control the femtosecond modification process, the laser fluence is typically the most influential experimental variable for all of the writing configurations. Adjusting the laser fluence by an order of magnitude can cause dramatically different results: from no modification, to the controlled modification used

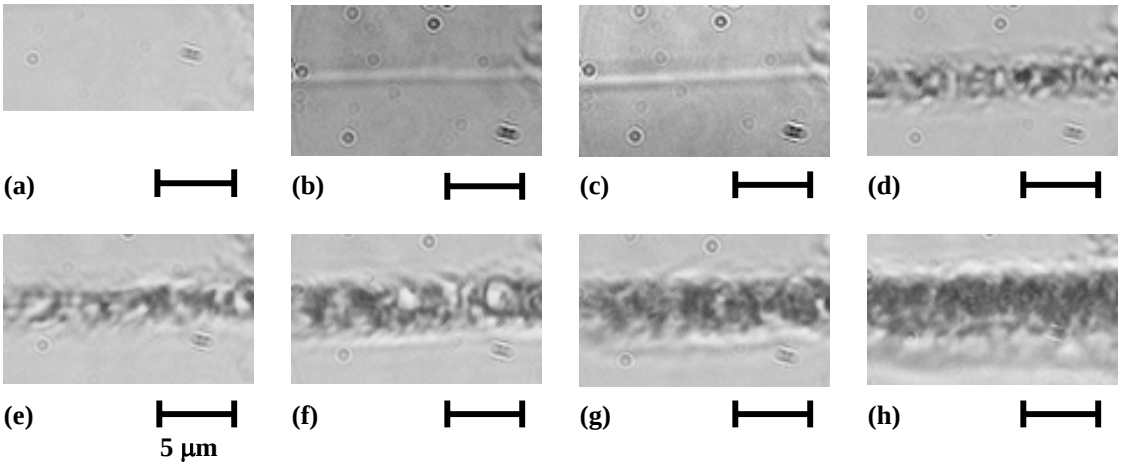

Figure 2.5 Waveguides produced by transverse writing with a 50X microscope objective and a pulse energy of a) 0.00 μJ, b) 0.15 μJ, c) 0.25 μJ, d) 0.70 μJ, e) 1.3 μJ, f) 2.0 μJ, g) 2.7 μJ, and h) 5.9 μJ [2.9].

for producing optical devices, to uncontrolled damage as shown in figure 2.5 [2.9]. This sensitivity results from the modification process having a highly nonlinear dependence on the peak intensity (I), which is directly proportional to the fluence (F) for a fixed pulse width as described in equation 2.1, where τ is the temporal pulse width.

$$F = I\tau \qquad \text{Eq 2.1}$$

Since most femtosecond laser systems have pulse widths of ~100 fs, the laser fluence (J / cm^2) has become the standard parameter for describing experimental conditions. The laser fluence is related to the laser pulse energy (E) and the focusing conditions by equation 2.2, where A is the exposed area, M^2 is the beam quality factor, λ is the wavelength, and NA is the numerical aperture of the microscope objective. For constant focusing conditions it is common for papers to list the pulse energy instead of the fluence.

$$F = \frac{E}{A} = \frac{\pi E (NA)^2}{\lambda^2 (M^2)^2} \qquad \text{Eq 2.2}$$

2.3 Waveguide Fabrication Mechanisms

Femtosecond laser waveguide writing has developed as an experimental discipline. Various groups have reported enormous success in fabricating many devices, in many materials, using many different writing configurations. Despite this success, the underlying mechanisms of the modification process are still poorly understood. My work has focused on understanding these mechanisms.

As they are currently understood, the writing mechanisms can be divided into two parts: energy absorption and energy dissipation. The energy absorption process is assumed to have the same mechanisms as femtosecond laser ablation. Laser ablation has been well studied by many groups [2.10-2.16, 2.18]. In it, energy is absorbed through a combination of multiphoton absorption and avalanche photo-ionization leading to plasma formation. The energy dissipation process is less well understood, though thermal diffusion and shock wave generation are the most popular proposed mechanisms. Further questions remain about how processing variables – the laser pulse energy, the laser repetition rate, and the glass composition – affect the modification process.

2.3.1 Multiphoton ionization

Multiphoton absorption is a nonlinear process in which several photons are absorbed by a material simultaneously to excite an electron. It is a very common process that can occur in any material, but it is frequently ignored because it typically contributes a negligible

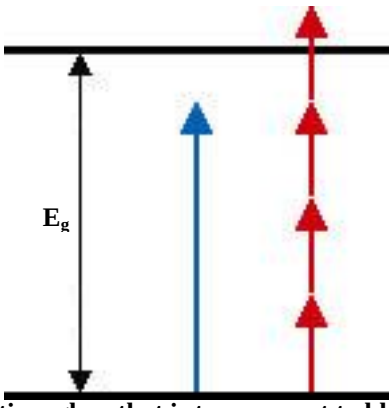

Figure 2.6 Multiphoton absorption, glass that is transparent to blue light can absorb infrared light through multiphoton absorption (4 photon multiphoton absorption shown).

fraction of the total absorption. Two conditions are required for multiphoton ionization to become the primary absorption process: The material must have a band gap that is greater than the energy of a single photon, and the light must have a very high intensity. Both of these requirements can be understood in terms of the absorption rate equation, equation 2.3,

$$\frac{dN}{dt} = \alpha I + \beta I^2 + \ldots + \gamma I^m \qquad \text{Eq 2.3}$$

where dN/dt is the number of photon excited per unit time, I is the intensity of the incident light, and α, β and γ are frequency dependent absorption coefficients for the 1st, 2nd, and mth order absorption modes. Terms with m > 1 are individually referred to as m photon multiphoton absorption, or collectively as nonlinear absorption. Higher order terms, with greater values of m, have orders of magnitude smaller absorption coefficients; reflecting the low probability of multiple photons interacting with an atom at once. This leads to the requirement that the light must have a very high intensity for substantial nonlinear absorption to occur.

Increasing the intensity of the light causes an increase in both linear and nonlinear absorption. For multiphoton absorption to be the dominant absorption mechanism it is necessary to almost eliminate linear absorption by reducing α to zero. This requirement can be achieved by adjusting the excitation frequency, which controls the energy of individual photons. A material that has a band gap greater than the energy of the incident photons – as shown in figure 2.6 – is transparent to those photons, and its linear absorption coefficient (α) is zero. In a material with a band gap of energy E_g and photon energy $h\nu$, the m photon multiphoton absorption will be dominant, where m is the lowest integer value satisfying equation 2.4 [2.11-2.12]. For femtosecond laser waveguide writing, values of m are typically in the range of 3 to 6.

$$mh\nu \geq E_g \qquad \text{Eq 2.4}$$

This discussion of multiphoton absorption focuses on the peak intensity of the laser, without indicating why it important to have short, femtosecond laser pulses. Using femtosecond laser pulses has two advantages compared with using longer laser pulses. The first is that for a given peak intensity, shorter pulses have less total energy resulting in far less collateral damage to the surrounding glass [2.13]. The second is that the above discussion of multiphoton absorption assumes a perfectly pure, defect free transparent material at 0 K; or simply put, a material with no conduction electrons. Clearly, none of these conditions hold true in real materials. High purity glasses normally have 10^8 to 10^{10} free conduction electrons primarily from intrinsic defects and metal impurities [2.14]. These intrinsic electrons, and any electrons excited by multiphoton absorption serve as seed electrons for a second excitation process known as avalanche photo-ionization, which is highly dependent on the laser pulse duration [2.11-2.16, 2.18].

2.3.2 Avalanche photo-ionization

Avalanche photo-ionization causes a rapid increase in the concentration of conduction electrons through a cyclic combination of inverse Bremsstrahlung absorption and impact ionization [2.15-2.16]. Free conduction electrons oscillate in electromagnetic fields (such as light) without any net gain or loss in energy. In inverse Bremsstrahlung absorption or Joule heating, electron / lattice interactions disrupt the oscillations of a free electron, allowing the electron to linearly absorb photons. The rate at which the electron gains energy (P) is quantitatively given in cgs units by equation 2.5 [2.16], where τ is the mean time between electron / lattice collisions, e is the charge of the electron, I is the intensity of the laser, n is the refractive index of the glass, c is the speed of light, and m is the effective mass of the electron.

$$P = \frac{2\pi e^2 I \tau}{ncm} \qquad \text{Eq 2.5}$$

Once an electron has twice the band gap energy of the glass it is possible for the electron to collide with a second bound electron, exciting the second electron to the conduction band, as depicted in figure 2.7. Both electrons are then free to absorb more energy through inverse Bremsstrahlung absorption, restarting the avalanche photo-ionization cycle.

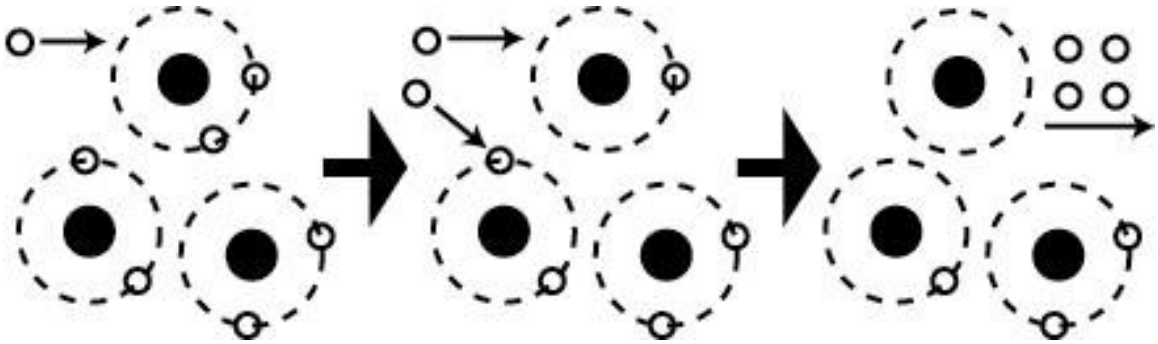

Figure 2.7 Avalanche photoionization (represented by the large arrows) causes an exponential increase in the free electron population once a free seed electron has been generated.

As a linear absorption process, avalanche photo-ionization occurs everywhere the material is exposed to the laser. It is limited by the concentration of free seed electrons and the time the cycle is allowed to repeat over (the pulse length). In order to limit the modification to the focal volume of the microscope objective, the intensity and duration of the laser pulse must be controlled such that there is sufficient time for avalanche photo-ionization seeded by electrons from multiphoton absorption to reach the modification threshold, yet that there is insufficient time for avalanche photo-ionization seeded by intrinsic, free electrons to reach the modification threshold elsewhere in the material. In general the shorter the pulse the easier it is to meet this criterion.

Unlike conventional methods in which seed electrons come from randomly distributed defects and impurities, in femtosecond laser writing, multiphoton ionization generates seed electrons from the bulk material. This difference results in the femtosecond laser fabrication process being insensitive to minor local glass variations, and creates a deterministic intensity threshold for material modification [2.13, 2.16]. The threshold is material and frequency dependent. Because of this threshold behavior, it is possible to fabricate features that are smaller than the diffraction limit of the microscope objective

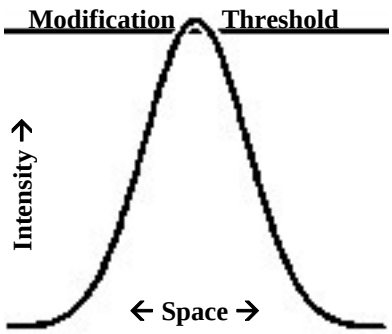

Figure 2.8 Very small features can be fabricated by controlling the total intensity with respect to a modification threshold that is dependent on the laser frequency and the material.

[2.18]. These small features can be formed because the intensity distribution for a focused Gaussian beam is well known and the peak intensity can be adjusted with respect to the deterministic modification threshold to control the feature size, as illustrated in figure 2.8. So far, research groups have used this technique to fabricate devices with features as small as 100 nm in diameter [2.19].

2.3.3 Plasma formation

The modification threshold for permanent material changes is normally associated with the critical electron density required to form plasma, after which the material becomes highly absorbent. This occurs when the plasma frequency of the electrons generated by multiphoton absorption and avalanche photo-ionization equals the frequency of the femtosecond laser. For a femtosecond laser with a wavelength of 800 nm, an electron density of approximately 10^{21} electrons cm^{-3} is required to trigger plasma formation. In the literature, this threshold is frequently referred to as the threshold for laser induced breakdown [2.11, 2.14]. If the pulse intensity is significantly greater than the modification threshold, the extra energy absorbed is believed to lead to micro-crack type damage or filamentation [2.20].

There are two schools of thought regarding whether it is necessary to create plasma in order to fabricate good waveguides. The first is that plasma must form in order for any permanent material changes to occur. The second is that micro-crack type damage results after forming plasma; and that femtosecond laser induced refractive index changes occur at slightly lower energies, before plasma forms [2.21].

2.3.4 Energy dissipation

The energy dissipation process is less well understood, than the energy absorption process. It is known that the dissipation process occurs on a timescale of hundreds of nanoseconds to a few microseconds; this is substantially longer than the hundreds of femtoseconds required for the energy absorption process. And, it is believed that the primary dissipation mechanisms are a combination of thermal diffusion [2.22] and shockwave generation [2.23], though it is uncertain which process is dominant. Both of these processes could lead to the rapid cooling, or quenching of the modified region as our group has proposed.

2.3.4.1 Thermal diffusion and accumulation

In thermal diffusion, heat flows from the "hot" excited region around the focal point to the "cool" bulk sample. The rate of thermal diffusion ($\delta T/\delta t$) without any heat sources or sinks is given by equation 2.6, where D is the diffusion coefficient, and T is the

temperature as a function of position [2.24]. This equation works well for describing the sample temperature during low repetition rate writing in which a single pulse generates a hot spot that cools off without external interactions. For high repetition rate writing in which thermal accumulation occurs, a comb source term is added to represent the periodic laser pulses.

$$\frac{\partial T}{\partial t} = D\nabla^2 T \qquad \text{Eq 2.6}$$

Thermal diffusion is believed to be the dominant cooling mechanism in the case of high repetition rate laser writing. If a single point is exposed to a high repetition rate laser, a spherical modified region that is substantially larger than the focal volume of the laser forms [2.25-2.26]. This constitutes clear evidence that thermal diffusion and accumulation occur, causing an increase in the temperature of the surrounding material.

For low repetition rate writing in which the modified region can be smaller than the focal volume of the laser, it is less certain whether thermal diffusion plays a substantial role. It is possible that thermal diffusion is still the dominant cooling mechanism, and that there is too much time between laser pulses for an increase in the temperature of the surrounding material to occur, though this is far from certain.

2.3.4.2 Shockwave propagation

A second possible modification mechanism for low repetition rate writing is that a shockwave is generated within the glass. The formation of plasma leads to a large charge separation within the exposed region. This charge separation may be sufficient to cause a

coulomb explosion, which would generate a shockwave [2.27]. The shockwave would then carry matter and energy away from the focal volume, compressing the surrounding material and leaving a rarified central region.

The strongest evidence that shockwaves occur are observations of voids forming at very high pulse energies. Scanning electron microscope (SEM) and atomic force microscope (AFM) images of polished surfaces and fracture planes have shown the presence of voids [2.23]. It is possible that polishing or fracturing the glass created these voids; so further evidence for the presence of shockwave-generated voids was collected from intact samples. Voids were formed, translated, and merged within a solid glass sample by slowly moving the focal point of a high intensity femtosecond laser [2.28]. The white light transmission images used in this experiment were hazy, showing dark spots; however the ability to translate and merge these spots indicates that they were voids.

Voids do not form at lower pulse energies [2.29]. Again, it is possible that shockwave generation is still the dominant modification mechanism. A shockwave could compress the material, causing local densification and a positive refractive index change as it travels outwards [2.30]. Unfortunately, it is difficult to explain recent results showing that the modification process is dependent on the glass composition using shockwaves.

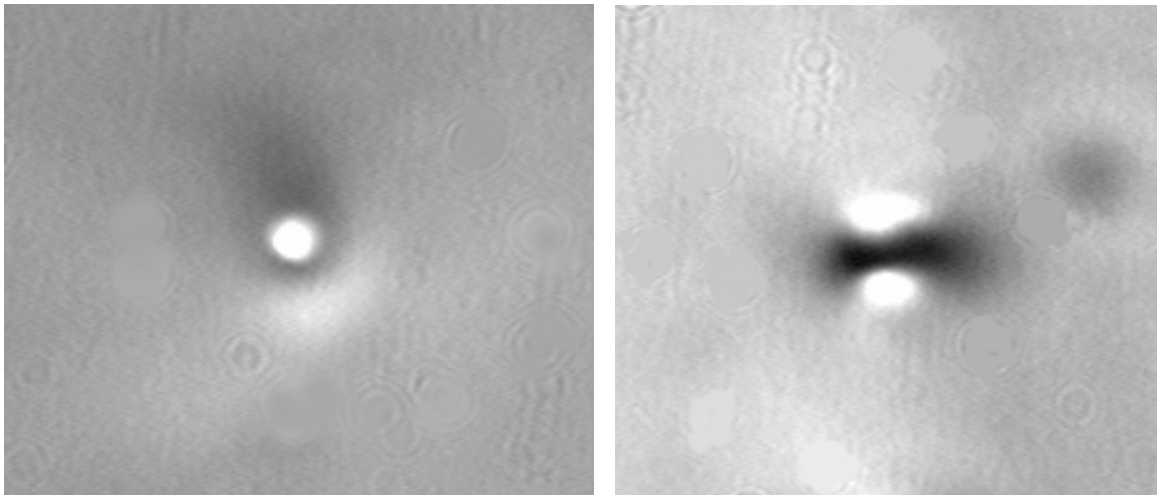

Figure 2.9 White light images of waveguides in fused silica (left), and IOG-1 (right) [2.31].

2.3.4.3 Effects of the Glass Composition

Recent work in our group has shown that waveguides written in different materials behave differently. Waveguides fabricated in a phosphate glass, Schott Integrated Optical Glass 1 (IOG-1), guide around the modified region with the exact structure being highly dependent on the laser alignment during fabrication [2.31]; in contrast waveguides written in fused silica guide light within the center of the modified region, as shown in figure 2.9. This behavior indicates different refractive index profiles. In IOG-1 the modification results in a lower refractive index inside the exposed region, and a higher refractive index surrounding peripheral regions [2.31]. In fused silica the modification results in a higher refractive index core, that may be surrounded by a lower refractive index peripheral region.

2.3.4.4 Fast quenching

Both types of behavior can be explained by fast quenching. The quenching rate refers to how fast a piece of glass is cooled. A fast quench is the result of a high cooling rate, and a slow quench is the result of a low cooling rate. Bulk, commercial glass is normally fabricated with a very low cooling rate of several degrees per minute. In contrast, both of the mechanisms proposed for energy dissipation during femtosecond laser writing would involve very high cooling rates, on the order of thousands of degrees per minute.

It is our belief that the material dependence of low repetition rate femtosecond laser waveguide writing can be elucidated by the relationship between the refractive index of the glass and the quenching rate. If the refractive index of a glass increases with increasing cooling rate, we would expect the modified material to have a higher refractive index than the bulk material. Likewise, if the refractive index of a glass decreases with increasing cooling rate, we would expect the modified material to have a lower refractive index than the bulk material.

Conservation of matter must also be taken into account because the interior of a glass block is a closed system. For a constant composition, the refractive index of a glass is almost always directly proportional its density. Thus in the case that the refractive index of a glass increases with increasing cooling rate, its density would also increase with increasing cooling rate. The law of conservation of matter stipulates that if part of the

modified material has a higher density; then another part (the surrounding material) must have a lower density, and hence a lower refractive index.

This mechanism can explain the different guiding behaviors observed in both fused silica and IOG-1. It is known that rapidly quenched bulk fused silica has a higher refractive index than slowly cooled fused silica [2.32-2.33], and it was measured that rapidly quenched bulk IOG –1 has a lower refractive index than slowly cooled IOG-1 [2.31]. Further support for this belief comes from additional work discussed in chapter 6, and from high resolution refractive index profiles of waveguides written in different glasses [2.34].

2.4 Spectroscopic Analysis of the fs Laser Modified Material

Laser spectroscopy is a method that can be used to further characterize the structural changes that are associated with waveguide behavior. In addition to the refractive index change, the femtosecond laser modification process causes structural changes within the material which can be detected using Raman and fluorescence spectroscopy. Thus, spectroscopy allows for direct imaging of the modified regions; these images can then be compared with the position of waveguides, as shown in figure 2.10 [2.31]. Comparing the two images, it can be concluded that the fluorescence is only coming from the dark central region in the white light image, and that the femtosecond laser did not directly modify the guiding regions.

Using spectroscopy, it is also possible to determine the molecular level changes that occur during the writing process. Femtosecond lasers have been used to modify large volumes of fused silica. Spectra of these large volumes indicate that there is a substantial increase in fluorescence that scales with increasing irradiance in the modified region due to the formation of non-bridging oxygen hole centers (NBOHC) [2.35]. These defects are a clear indication that the femtosecond laser writing process disrupts the structure of the material. However, the refractive index change remains after the NBOHC defects have been destroyed by annealing or photobleaching the glass. This indicates that the defects are not responsible for the refractive index change, and that other changes must also occur.

Raman spectra of the same large modified volumes indicate that the concentration of three- and four-membered ring structures are as much as 5× higher in the modified glass than in the unmodified material. The concentration of three-membered rings scales with the laser fluence, as shown in figure 2.11 [2.9]. This increase in the population of ring structures is consistent with densification inside the modified region [2.30, 2.36-2.38],

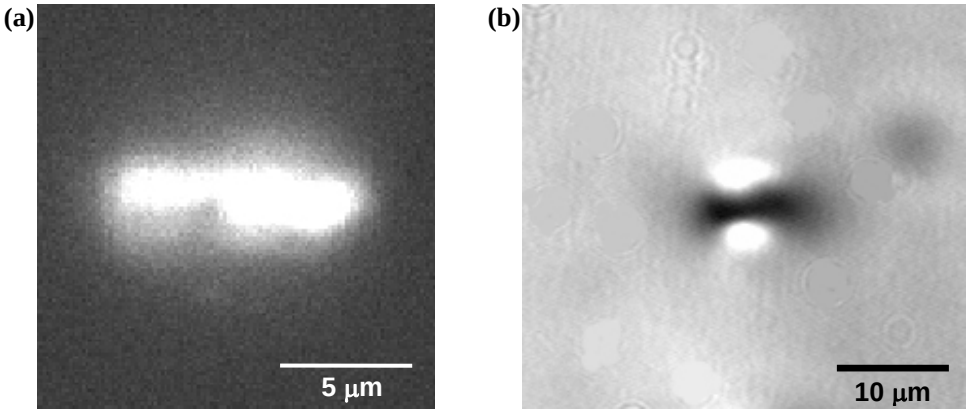

Figure 2.10 a) fluorescence and b) white light images of a waveguide fabricated in IOG-1. Note, the different scale bars.

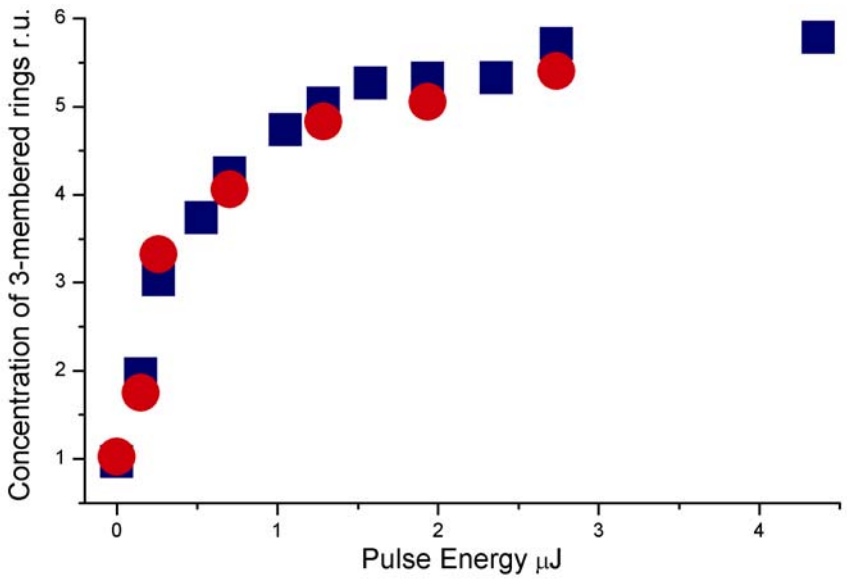

Figure 2.11 Concentration of 3-membered rings in fused silica after exposure to a femtosecond laser. The data is normalized to the concentration in unmodified glass.

and there is a high probability that this structural change is the underlying cause of the refractive index change.

2.4.1 A Brief Description of Raman Spectroscopy

Raman spectroscopy measures light that is inelastically scattered by its interactions with electrons in matter. Electrons are charged particles that oscillate in electro-magnetic fields, such as light. These oscillations temporarily polarize the bonds in molecules, allowing for energy to be transferred from a photon of light to the vibrational state of a molecule. The resulting shift in the wavelength of the light is then measured, indicating how much energy was transferred to the molecule. The magnitude of this change is known as the Raman shift. It is typically recorded in units of inverse centimeters (cm^{-1}), and can be used to determine the molecular structures of many materials.

It is important to remember that the Raman shift is the result of a scattering process. This means that the excitation light is never actually absorbed by the material, and that the excitation frequency is not resonant with any transitions in the material. In a Jablonski diagram (figure 2.12) the temporary polarization that allows for Raman scattering is represented by a dashed line and is referred to as a "virtual state."

For energy to be transferred from a photon to the vibrational state of a material, the material must have vibrational modes whose total polarizability changes as a function of the bond distance or orientation. For example the symmetric stretching mode of carbon dioxide, figure 2.13 (left), is Raman active because the total polarizability changes. The

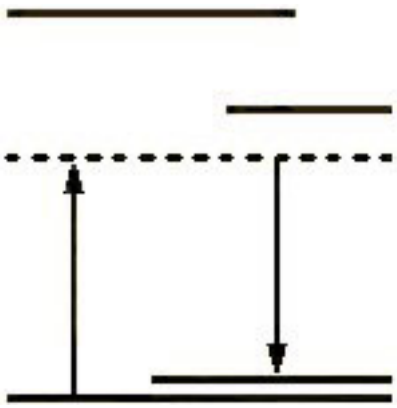

Figure 2.12 Jablonski Diagram of Stokes shifted Raman scattering.

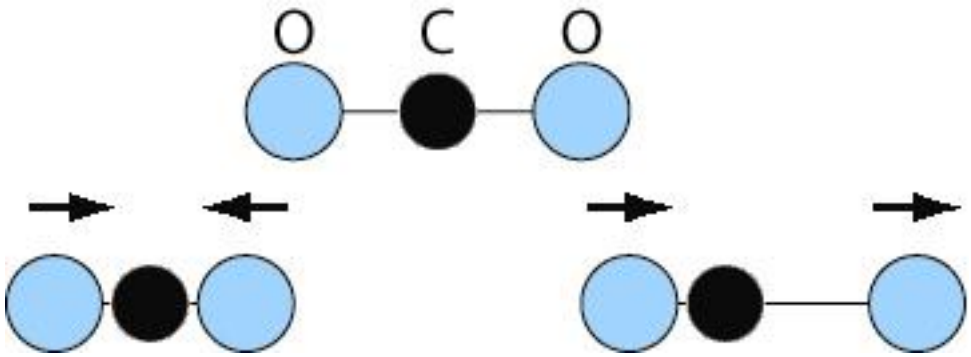

Figure 2.13 Symmetric (left) and asymmetric (right) stretching vibrational modes of CO_2.

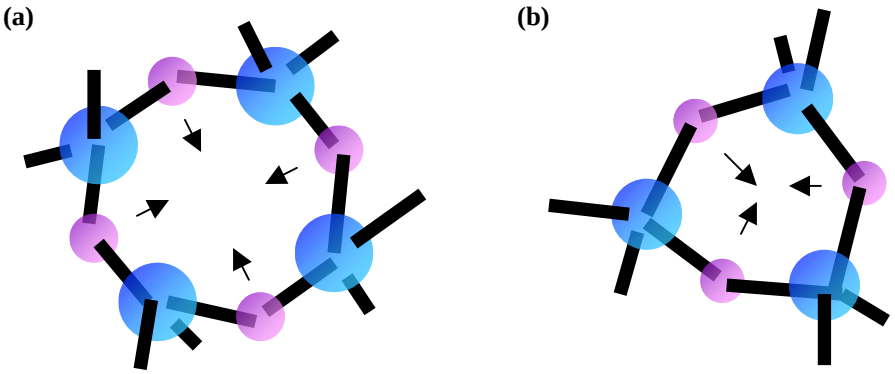

Figure 2.14 An atomistic representations of a) four- and b) three-membered rings that correspond to the D_1 and D_2 breathing modes at 490 and 605 cm^{-1} in fused silica. The silicon atoms are shown in blue, and the oxygen atoms are shown in purple.

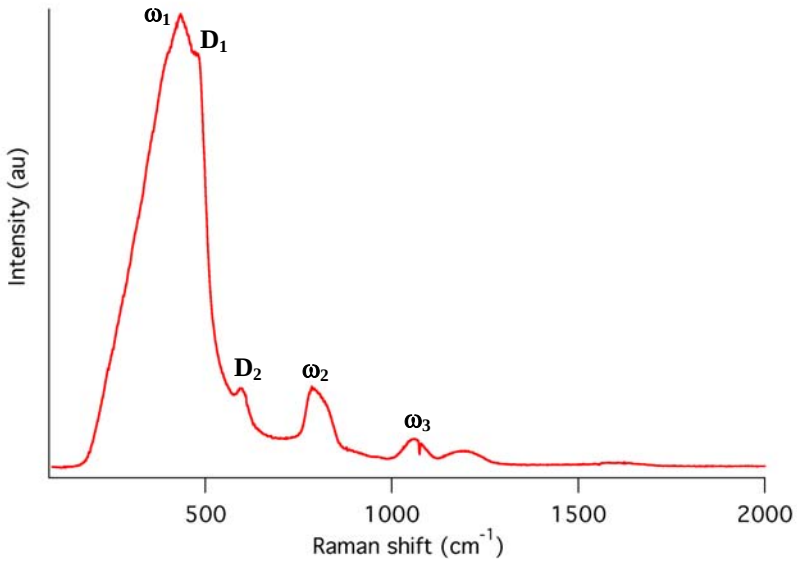

Figure 2.15 Sample Raman spectrum of fused silica. The ω_1, ω_2, and ω_3 peaks are vibrational modes of the silica network.

asymmetric stretching mode, figure 2.13 (right), is not Raman active because as one bond lengthens the other contracts with the total polarizablity remaining constant [2.39].

The three- and four-membered rings mentioned earlier have Raman lines at 605 cm^{-1} and 490 cm^{-1} respectively as a result of breathing vibrational modes [2.36-2.38]. In these breathing modes, shown in figure 2.14, the entire ring expands and contracts with all of the bonds lengthening or shortening together, causing a large change in the polarizability.

The relative concentration of three and four-membered rings is determined by measuring the area under the 605 cm^{-1} and 490 cm^{-1} (D_2 and D_1) peaks, and dividing by the Raman signal from the fused silica, which is taken to be either the total Raman signal strength (which is dominated by the silica network) or the area of the ω_2, Si-O vibrational peak at 800 cm^{-1}. All of these peaks are labeled on the sample spectrum shown in figure 2.15.

2.4.2 A Brief Description of Fluorescence Spectroscopy

Fluorescence occurs when light of one frequency is absorbed by an atom or molecule, causing an electronic excitation. The excited state then undergoes non-radiative energy loss, and light of a second frequency is emitted, as shown in figure 2.16. Fluorescence spectroscopy involves measuring this emitted light as a function of frequency. Like Raman scattering, fluorescence emissions provide information about the microstructure of a material.

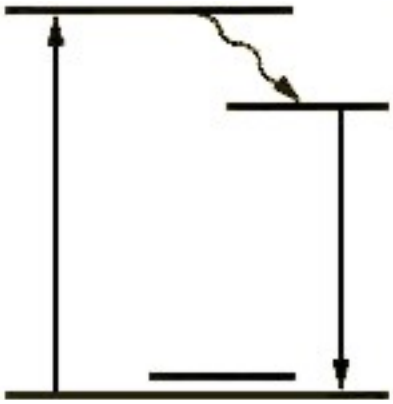

Figure 2.16 Jablonski Diagram of Fluorescence Emission.

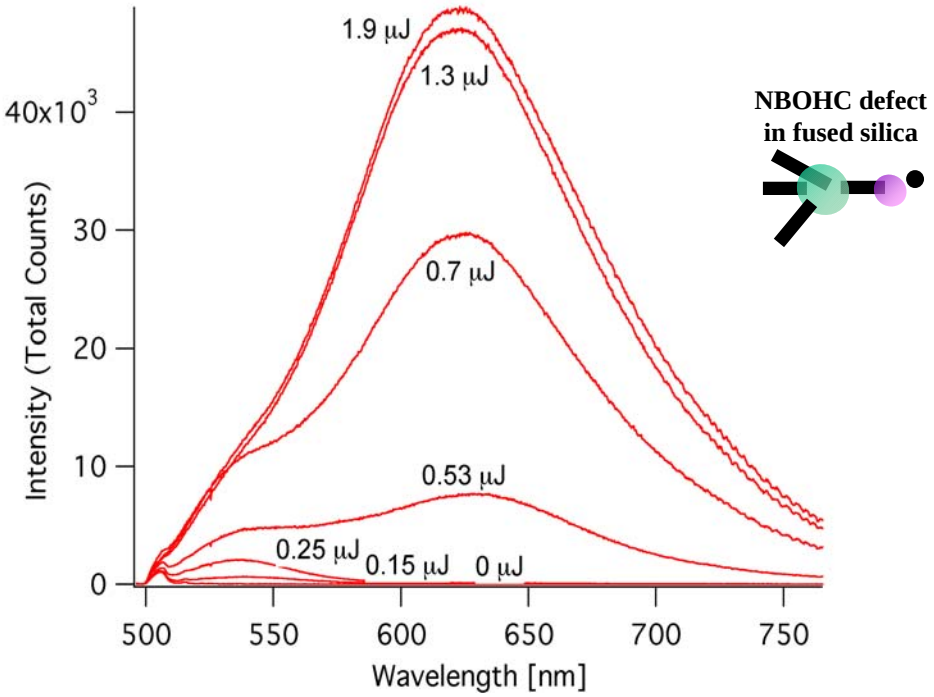

Figure 2.17 Sample spectra and atomistic depiction of NBOHC defects in fused silica [ref]. The silicon atoms are shown in green, and the oxygen atoms are shown in purple.

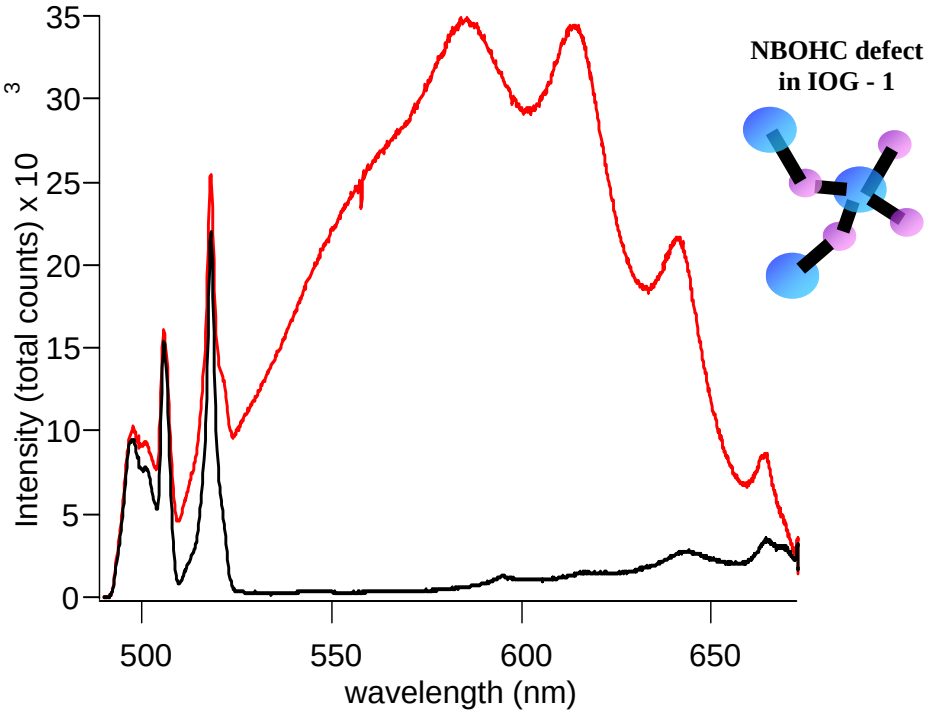

Figure 2.18 Sample spectrum and atomistic depiction of NBOHC defects in IOG – 1 [2.31]. The phosphorous atoms are shown in blue, and the oxygen atoms are shown in purple.

Most of the glasses studied have minimal intrinsic fluorescence, though highly fluorescent defect states arise during the modification process. The fluorescence signals for fused silica and IOG-1 both show non-bridging oxygen hole center (NBOHC) type defects [2.31, 2.35]. Depictions of these NBOHC defects and sample spectra for fused silica and IOG-1 are shown in figures 2.17 and 2.18 respectively. The strength of the fluorescence signal is directly proportional to the defect concentration. Thus, the fluorescence intensity can be used to determine what areas have been modified, and to a more limited extent how much modification has occurred.

References

2.1 R. Osellame, S. Taccheeo, M. Marangoni, R. Ramoni and P. Laporta, "Femtosecond writing of active optical waveguides with astigmatically shaped beams," *Journal of the Optical Society of America B*, **20**(7), pp. 1559-1567, (2003).

2.2 C. B. Schaffer, A. Brodeur, J. F. Garcia and E. Mazur, "Micromachining bulk glass by use of femtosecond laser pulses with nonojoule energy," *Optics Letters*, **26**(2), pp. 93-95, (2001).

2.3 R. Osellame, N. Chiodo, V. Maselli, A. Yin, M. Zavelani-Rossi, G. Cerullo, P. Laporta, L. Aiello, S. De Nicola, P. Ferraro, A. Finizo and G. Pierattini, "Optical properties of waveguides written by a 26 MHz stretched cavity Ti:sapphire femtosecond oscillator," *Optics Express*, **13**(2), pp. 612-620, (2005).

2.4 S. Juodkazis, H. Misawa and I. Maksimov, "Thermal accumulation effect in three-dimensional recording by picosecond pulses," *Applied Physics Letters*, **85**(22), pp. 5239-5241, (2004).

2.5 S. Nolte, M. Will, J. Burghoff and A. Tunnermann, "Ultrafast laser processing: new options for three-dimensional photonic structures," *Journal of Modern Optics*, **51**(Sp. SI), pp. 2533-2542, (2004).

2.6 L. Shah, A. Y. Arai, S. M. Eaton, and P. R. Herman, "Waveguide writing in fused silica with a femtosecond fiber laser at 522 nm and 1 MHz repetition rate," *Optics Express*, **13**(6) 1999-2006, (2005).

2.7 S. J. Mihailov, C. W. Smelser, P. Lu, R. B. Walker, D. Grobnic, H. Ding and J. Unruch, “Fiber Bragg gratings made with a phase mask and 800-nm femtosecond radiation,” *Optics Letters*, **28**(12), pp. 995-997, (2003).

2.8 S. J. Mihailov, C. W. Smelser, P. Lu, R. B. Walker, D. Grobnic, H. Ding and J. Unruch, “Bragg Gratings Written in All-SiO_2 and Ge-Doped Core Fibers With 800-nm Femtosecond Radiation and a Phase Mask,” *Journal of Lightwave Technology*, **22**(1), pp. 94-100, (2004).

2.9 J. W. Chan, T. R. Huser, S. H. Risbud and D. M. Krol, “Structural changes in fused silica after exposure to focused femtosecond laser pulses,” *Optics Letters*, **26**(21), pp. 1726-1728, (2001).

2.10 S. C. Jones, P. Braunlich, R. T. Casper, X. A. Shen and P. Kelly, “Recent progress on laser-induced modifications and intrinsic bulk damage of wide-gap optical-materials,” *Optical Engineering*, **28** 1039–1068, (1989).

2.11 C. B. Schaffer, A. Brodeur and E. Mazur, “Laser-induced breakdown and damage in bulk transparent materials induced by tightly focused femtosecond laser pulses,” *Measurement Science and Technology*, **12**, pp. 1784–1794, (2001).

2.12 C. W. Carr, H. B. Radousky and S. G. Demos, “Wavelength Dependence of Laser-Induced Damage: Determining the Damage Initiation Mechanisms,” *Physical Review Letters*, **91**(12), pp. 127402-1 – 127402-4, (2003).

2.13 B. C. Stuart, M. D. Feit, S. Herman, A. M. Rubenchik, B. W. Shore and M. D. Perry, “Nanosecond-to-femtosecond laser-induced breakdown in dielectrics,” *Physics Review* B, **53**(4), pp. 1749–61, (1996).

2.14 X. Liu, D. Du, and G. Mourou, “Laser Ablation and Micromachining with Ultrashort Laser Pulses,” *IEEE Journal of Quantum Electronics*, **33**(10), pp. 1706-1716, (1997).

2.15 D. Du, X. Liu, G. Korn, J. Squier and G. Mourou, “Laser-induced breakdown by impact ionization in SiO_2 with pulse widths from 7 ns to 150 fs,” *Applied Physics Letters*, **64**(23), pp. 3071–3073, (1994).

2.16 T. Q. Jia, Z. Z. Xu, R. X. Li, D. H. Feng, X. X. Li, C. F. Cheng, H. Y. Sun, N. S. Xu and H. Z. Wang, “Mechanisms in fs-laser ablation in fused silica,” *Journal of Applied Physics*, **95**(9), pp. 5166-5171, (2004).

2.17 R. W. Boyd Nonlinear Optics, Second Edition, Academic Press, Rodchester, NY, 2003, pp. 518.

2.18 C. H. Fan and J. P. Longtin, “Modeling optical breakdown in dielectrics during ultrafast laser processing,” *Applied Optics*, **40**(18), pp. 3124-3131, (2001).

2.19 F. Korte, J. Koch, J. Serbin, A. Ovsianikov and B. N. Chichkov, “Three-Dimensional Nanostructuring With Femtosecond Laser Pulses,” *IEEE Transactions on Nanotechnology*, **3**(4), pp. 468-472, (2004).

2.20 L. Sudri, A. Couairon, M. Franco, B. Lamouroux, B. Prade, S. Tzortzakis and A. Mysyrowicz, “Femtosecond Laser-Induced Damage and Filamentary Propagation in Fused Silica,” *Physical Review Letters*, **89**(18), pp. 186601-1 – 186601-4, (2002).

2.21 C. W. Smelser, S. J. Mihailov and D. Grobnic, “Formation of Type I-IR and Type II-IR gratings with an ultrafast IR laser and a phase mask,” *Optics Express*, **13**(14), pp. 5377-5386, (2005).

2.22 K. M. Davis, K. Miura, N. Sugimoto and K. Hirao, "Writing waveguides in glass with a femtosecond laser" *Optics Letters*, **21**(21), pp. 1729-1731, (1996).

2.23 E. N. Glezer and E. Mazur, “Ultrafast-laser driven micro-explosions in transparent materials,” *Applied Physics Letters*, **71**(7), pp. 882–884, (1997).

2.24 E. Butkov, Mathematical Physics, Addison-Wesley Publishing Company, Reading, Massachusetts, 1968, pp. 297.

2.25 C. B. Schaffer, J. F. Garcia and E. Mazur, “Bulk heating of transparent materials using a high-repetition-rate femtosecond laser,” *Applied Physics A*, **76** pp. 351-354, (2003).

2.26 S. M. Eaton, H. Zhang, P. R. Herman, F. Yoshino, L. Shah, J. Bovatsek and A. Y. Arai, “Heat accumulation effects in femtosecond laser-written waveguides with variable repetition rate,” *Optics Express*, **13**(12), pp. 4708-4716, (2005).

2.27 D. Ashkenasi, G. Muller, A. Rosenfeld, R. Stoian, I. V. Hertel, N. M. Bulgakova and E. E. B. Campbell, “Fundamentals and advantages of ultrafast micro-structuring of transparent materials,” *Applied Physics A*, **77**, pp. 223-228, (2003).

2.28 W. Watanabe, T. Toma, K. Yamada, J. Nishii, K. Hayashi and K. Itoh, “Optical seizing and merging of voids in silica glass with infrared femtosecond laser pulses,” *Optics Letters*, **25**(22), pp. 1669-1671, (2000).

2.29 C. B. Schaffer, A. O. Jamison and E. Mazur, “Morphology of femtosecond laser-induced structural changes in bulk transparent materials,” *Applied Physics Letters*, **84**(9), pp. 1441-1443, (2004).

2.30 A. Kubota, M. J. Caturla, J. S. Stolken, and M. D. Feit, “Densification of fused silica due to shock waves and its implications for 351 nm laser induced damage,” *Optics Express*, **8**(11), pp. 611-616, (2001).

2.31 J. W. Chan, T. R. Huser, S. H. Risbud and D. M. Krol, "Waveguide fabrication in phosphate glasses using femtosecond laser pulses," *Applied Physics Letters*, **82**(15)**,** pp. 2371-2373, (2003).

2.32 U. Haken, O. Humbach, S. Ortner and H. Fabian, "Refractive index of silica glass: influence of fictive temperature," *Journal of Non-Crystalline Solids*, **265**(1), pp. 9-18, (2000).

2.33 R. Bruckner, "Properties and Structure of Vitreous Silica. I," *Journal of Non-Crystalline Solids*, **5**(2), pp. 123-175, (1970).

2.34 V. R. Bhardwaj, E. Simova, P. B. Corkum, D. M. Rayner, C. Hnatovsky, R. S. Taylor, B. Schreder, M. Kluge and J. Zimmer, "Femtosecond laser-induced refractive index modification in multicomponent glasses," *Journal of Applied Physics*, **97**, 083102, (2005).

2.35 J. W. Chan, T. R. Huser, S. H. Risbud and D. M. Krol, "Modification of the fused silica glass network associated with waveguide fabrication using femtosecond laser pulses," *Applied Physics A*, **76**, pp. 367-372, (2003).

2.36 A. E. Geissberger and F. L. Galeener, "Raman studies of vitreous SiO_2 versus fictive temperature" *Physical Review B*, **28**(6), pp. 3266–3271, (1983).

2.37 A. Pasquarello and R. Car, "Identification of Raman defect lines as signatures of ring structures in vitreous silica," *Physical Review Letters*, **80**(23), pp. 5145–5147, (1998).

2.38 M. Okuno, B. Reynard, Y. Shimada, Y. Syono and C Willaime, "A Raman spectroscopic study of shock-wave densification of vitreous silica," *Physics and Chemistry of Minerals*, **26**, pp. 304–311, (1999).

2.39 D. A. Skoog, F. J. Holler and T. A. Nieman, Principles of Instrumental Analysis, Fifth Edition, Harcourt Brace College Publishers, Orlando, FL, 1998, pp. 429.

Chapter 3

Experimental Equipment and Procedures

3.1 Chapter Overview

This chapter discusses the combined femtosecond fabrication / confocal spectroscopy microscope, and the general operating procedures used for conducting experiments. A detailed description of the components used in constructing the microscope system is followed by a description of the laser systems. The chapter concludes with a discussion of the confocal microscope and the spectroscopic analysis procedures.

Specific operating parameters for different experiments are described in later chapters with the results of each experiment.

3.2 Overview of the Combined Microscope System

A combined femtosecond laser writing setup / confocal microscope was built to both fabricate and analyze devices without removing the sample. The bulk of the microscope was assembled atop a flat optical table. However, a post system was used to construct a more complex sample mount to allow for viewing and scanning the glass from multiple orthogonal directions. A schematic diagram of the microscope (not to scale) is shown in figure 3.1.

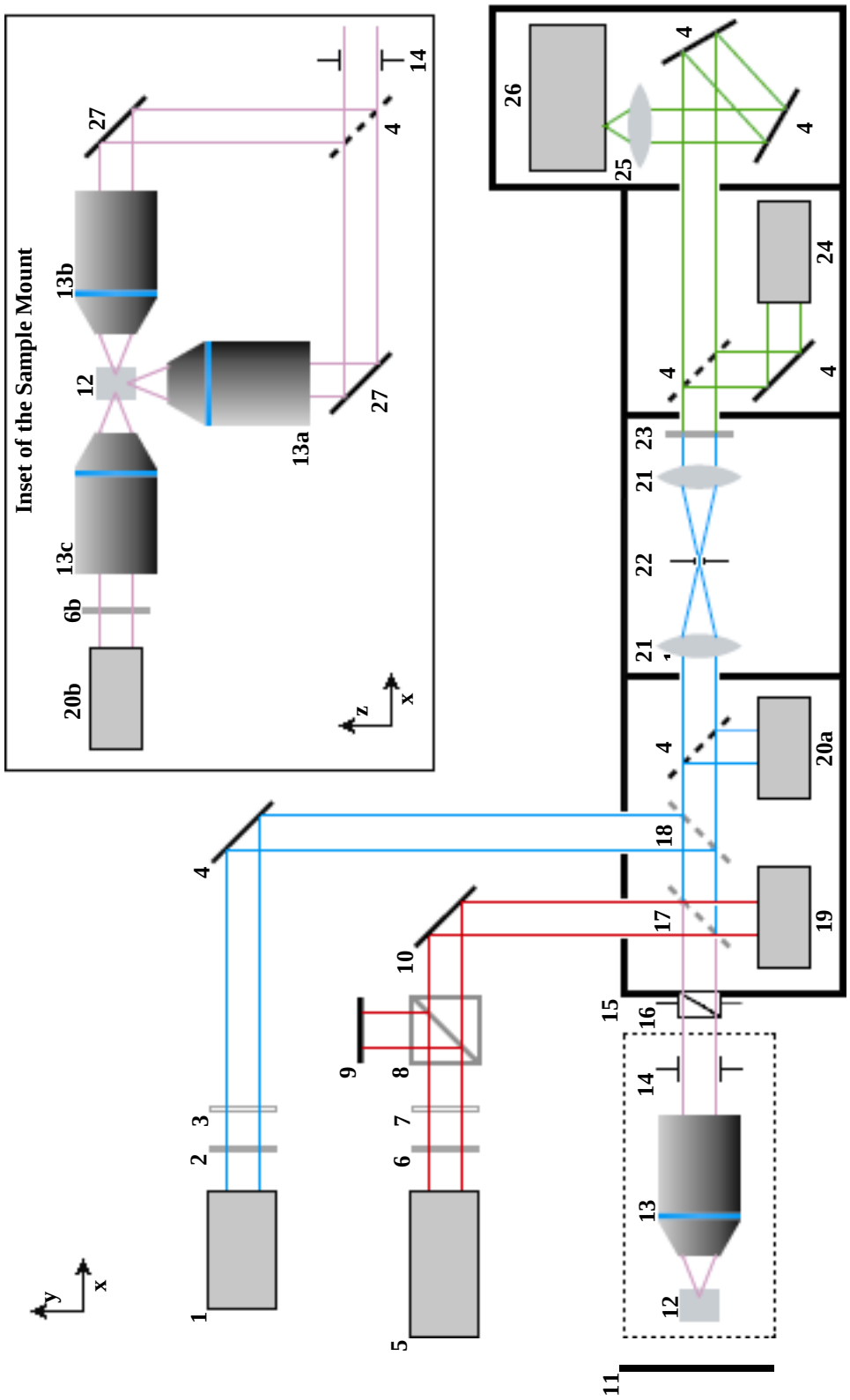

Figure 3.1 Schematic diagram of the combined femtosecond laser writing setup / confocal microscope. The bulk of the optical components are on a flat optical table, however the sample mount detailed in the inset, is mounted vertically. Note, the dashed lines indicate flip mounts that allow for easy removal of the optical element. This drawing is not to scale.

Descriptions of the numbered components in figure 3.1 are listed below. When these components are mentioned later in this chapter they are followed by the label (item #), where # is the number listed in figure 3.1. The components that are represented by a dashed line in figure 3.1 are mounted on flip mounts such that they can be removed and reinserted without disturbing the alignment of the microscope. Color coding is used to distinguish different laser beams: red, light from the Ti:Sapphire laser; blue, light from the argon ion laser; purple, overlapped beams from both laser systems; and green, signals from the sample after spectral filters remove the light from the argon ion laser laser.

1. A Uniphase, 2211-20SL, 488 nm, continuous wave argon ion laser. The laser was modified to increase its maximum output power from 20 to 50 mW. This change also resulted in weak emissions from other Argon lines.

2. An Omega Optical 488 nm notch filter, 488NB3, was used to eliminate the other emission lines from the argon ion laser.

3. A 488 nm, ¼ wave plate used to convert the laser from linear to circular polarization. This prevents possible polarization effects from interfering with the spectroscopy. Manufacture unknown.

4. Thor Labs, KM100-E02, 1” UV / Vis dielectric mirrors.

5. A Spectra Physics Ti:Sapphire pulsed laser system that operates at 1 kHz with 130 fs, 500 μJ pulses. The system consists of four lasers: a Millennia V, a Tsunami 3941-Mis, a Merlin, and a Spitfire LCX. This laser system is described in more detail in section 3.4.

6. Removable grey glass, neutral density filters that may be used to reduce the intensity of the laser. Manufacture unknown.

7. An 800 nm, ½ wave plate that is used to rotate the polarization of the femtosecond laser pulses. The pulses exiting the Spitfire start with 100:1 linear, horizontal polarization. Manufacture unknown.

8. A polarizing, cube beam splitter transmits horizontally polarized light and reflects vertically polarized light. It is used in conjunction with the ½ wave plate (item 7) to control the pulse energy. Manufacture unknown.

9. A beam block consisting of a stack of razor blades, that absorbs stray light from the spitfire. Constructed in house.

10. Thor Labs, KM100-E03, 1” near IR dielectric mirrors.

11. A far field barrier / target constructed of white poster board, located ~2 m beyond the sample mounts is used during the laser alignment procedures.

12. The sample / sample mount. The sample mount consists of a flat rod bolted to a Newport 562 series, five axis fiber positioning stage, atop two high precision, slow speed Newport 850G stepper motor stages. These stages travel in the "x" and "y" directions indicated in figure 3.1. The flat rod can be replaced to accommodate unusual sample shapes.

13. There are three objective mounts for looking at the sample from different directions. Mounts (a) and (b) are used for transverse and longitudinal waveguide writing respectively. Mounts (b) and (c) are used together to couple the Ar^+ laser (item 1) into the resulting waveguides. Various achromatic, air, infinity corrected, ELWD and XLWD series Nikon objectives ranging from 5 to 100X were used for different experiments.

14. A Newport ID – 1.0 iris was used for aligning both the Ti:Sapphire and the Argon Ion lasers. It was left open during experiments to prevent clipping.

15. A black box and several baffles were erected to prevent stray light from reaching any of the detectors. It was constructed in house using black eighth inch thick foam backing board, black duct tape, and black cloth.

16. A 1" Uniblitz shutter with a VMM-D1 driver was used to control the exposure of the sample to the lasers.

17. A 50/50 broadband dielectric beam splitter was used to direct the femtosecond laser into the sample, while simultaneously performing for transmission imaging in the back direction (from the sample to the microscope). Manufacture unknown.

18. A 488 Raman BS, beam splitter from Croma that reflects the 488 nm laser, and transmits the longer wavelength back scattered Raman and back emitted fluorescence signals.

19. An Ophir Nova II power meter with a PE 9 head was used to measure the pulse energy of the spitfire laser. The power meter was placed as shown in figure 3.1 during laser fabrication. A calibration procedure was performed to correlate the pulse energy at the sample with the pulse energy measured at the location of the power meter; the pulse energies at the sample are reported in this dissertation.

20. A Sony XC-75 charge couple device (CCD) camera was used for collecting both back-transmitted white light images in position (a), and near field waveguide coupling profiles in position (b).

21. Two Thor Labs LAC788-A, 150 mm, achromatic lenses were focused on each other such that there was no magnification or deviation of the laser from its original path after passing through both lenses.

22. A 75 μm pinhole was placed at the mutual foci of the two lenses (item 20) to construct the spatial filter in the confocal microscope, which is described in more detail in section 3.4.

23. Spectral filters were used to eliminate unwanted wavelengths of light before the signal reached the detectors. A 1" round Croma 488 Raman exit filter, 488hhqlp (488 nm, high quality long pass) was normally used for performing spectroscopy with the argon ion laser. Other filters were used for select experiments as specified in the experimental descriptions.

24. A UV enhanced Perkin Elmer photon counting module, MP 942 was used for rapid fluorescence imaging of several samples.

25. A 30 mm, Thor Labs LAC896-A, achromatic lens was used to couple light from the sample into the spectrometer (item 26).

26. An Oriel, MS257 spectrometer with 300 and 1200 groove / mm, 500 nm blaze gratings; and a Roper Spec-10:100B, liquid nitrogen cooled CCD camera were used to collect spectra of the sample.

27. Metal mirrors with greater than 90% reflectance at both 488 nm and 800 nm. Manufacture unknown.

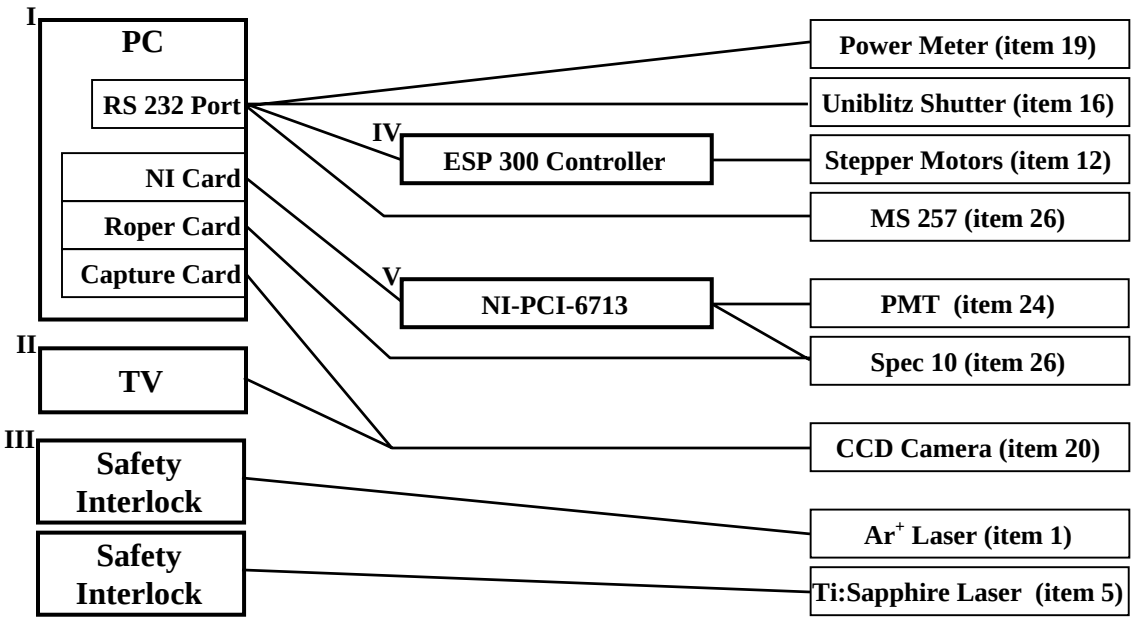

Figure 3.2 A sketch of the electrical components and connections used to operate the combined microscope described in section 3.2.

3.3 Electronic Control Systems

Most of the data acquisition and analysis were performed using a PC. Several Labview scripts were written to interface with commercial software packages that came with different instruments. The PC, and several other pieces of electrical equipment that were used to control the microscope are described below. A sketch of the electrical connections between this equipment and the optical components described in section 3.2 is presented in figure 3.2.

I. A 2.4 GHz PC with 524 MB RAM in a tower case was used to control most of the microscope. Four PCI cards enabled the computer to interface with a wide variety of devices: A National Instruments NI-PCI-8430/8 card added eight RS-232 serial

ports to the computer. A National Instruments NI-PCI-6713 card provided analog output, digital I/O, and counter-timer connections. A customized control card came with the Spec-10 camera. And, a capture card with AD signal conversion was added to record images from the Sony CCD camera.

Individual user accounts were created on the computer using MS Windows 2k Professional. Several hardware control programs were designated as being common to all users. These included: Winspec, a proprietary control program for the Spec-10 camera. NI measurement and automation, a proprietary program that enabled the computer to recognize devices connected to the NI cards. StarCom32, a proprietary program used to control the power meter. And Labview 6.0i scripts for operating the MS-257 spectrometer, the Spec-10 camera, the Uniblitz shutter, the PMT, and the stepper motors. These scripts were either written in-house or customized open-source operating scripts from the hardware suppliers.

II. A 15” Sony Trinitron TV was used to view the images from the Sony CCD camera, without taking up desktop space on the computer.

III. A safety interlock shutter blocked each laser. The shutters were set to close if someone opened the lab door without first entering a bypass pin-code.

IV. A Newport ESP-300 motion controller served as an interface between the computer and the stepper motor stages.

V. A NI-PCI-6713, analogue output board in a NI-CA-1000 enclosure with BNC connectors was used to coordinate the Spec-10 camera with scanning programs and to measure the signal from the photon counting PMT.

3.4 Femtosecond Laser Systems

Four different femtosecond laser systems were used for waveguide fabrication in different experiments: the amplified Ti:Sapphire laser listed above (item 5), a similar Spitfire, amplified Ti:Sapphire laser at the Communications Research Centre Canada, an in-house built amplified Ti:Sapphire laser at Harvard, and a Nd doped FPCA μJewel fiber laser at IMRA America, Inc.. These lasers have different pulse energies, pulse widths, pulse repetition rates, and wavelengths. The specific operating parameters for each laser are described with the experiments they were used for in later chapters.

3.4.1 Oscillators

All four of the lasers used for fabricating waveguides consist of an oscillator that generates femtosecond pulses, followed by an amplifier that increases the energy per pulse. In general terms, a femtosecond oscillator consists of a standard laser cavity with some mechanism of favoring mode-locked, pulsed operation over continuous wave (CW) operation. This mechanism could be intrinsic to the gain material, an intra-cavity saturable absorber, an acousto-optic modulator, the Kerr lens effect, or something else.

Regardless of how a laser is converted from CW to pulsed operation, the pulse repetition rate of the oscillator is determined by the cavity length, according to equation 3.1; where r is the repetition rate, L is the cavity length, and c is the speed of light.

$$r = \frac{c}{L} \qquad \text{Eq. 3.1}$$

All femtosecond, pulsed laser oscillators also have intra-cavity dispersion compensation. The uncertainty principle requires that ultra-short pulses have wide spectral bandwidths. As the pulses pass through air, the lasing medium, and various other optical elements different colors spectrally disperse, such that each color passes a set point in space at a different time. These spread out pulses are referred to as “chirped” pulses. Air and most optical elements induce positive dispersion or a positive chirp in the visible spectrum, meaning that the redder wavelengths precede the bluer. In dispersion compensation, a pair of prisms or gratings is used to induce negative dispersion, recompressing the pulses in time.

All of our in house waveguide fabrication was performed using a commercial titanium doped sapphire (Spectra Physics Tsunami Oscillator / Spitfire Amplifier) laser system. The Tsunami oscillator is actively mode locked at a rep rate of 82 MHz using an acousto-optic modulator (AOM). The AOM has a time dependent loss that is controlled by a radio frequency (rf) signal, which is set to match the intrinsic repetition rate of the laser based on its cavity length. Active mode locking allows for electronic synchronization

with other devices and helps stabilize the system against random disturbances. The Tsunami can also operate passively, without the AOM, because of the Kerr Lens effect.

The Tsunami can operate over a wide range of wavelengths, that are determined by the Ti:Sapphire laser rod and the mirrors in the cavity. Ti:Sapphire crystals have broad emission from 600 to 1080 nm. The lasing region is further restricted by a weak Ti^{4+} absorption band, and by losses elsewhere in the system. Our system is limited to 720 to 850 nm by its mirror set. The operating wavelength and bandwidth are controlled by an adjustable slit between two prism pairs. At least 13 nanometers of bandwidth are required for near transform limited <80 fs pulses, centered around 790 nm. Using a 5 W, 532 nm doubled Nd:YVO_4 Spectra Physics, Millennia pump laser, the Tsunami has an output energy per pulse of ~6 nJ [3.1]. This pulse energy is not high enough to modify most glasses directly so an additional amplifier is required.

3.4.2 Regenerative amplifiers

A 1 kHz repetition rate, Spitfire regenerative amplifier increases the energy per pulse from ~6 nJ to >500 μJ. This system uses "Chirped Pulse Amplification" to produce greater pulse amplification, without damaging the Ti:Sapphire crystal in the amplifier, as depicted in figure 3.3 [3.2]. There are three stages to the spitfire amplifier: a pulse stretcher, the regenerative amplifier, and a pulse compressor.

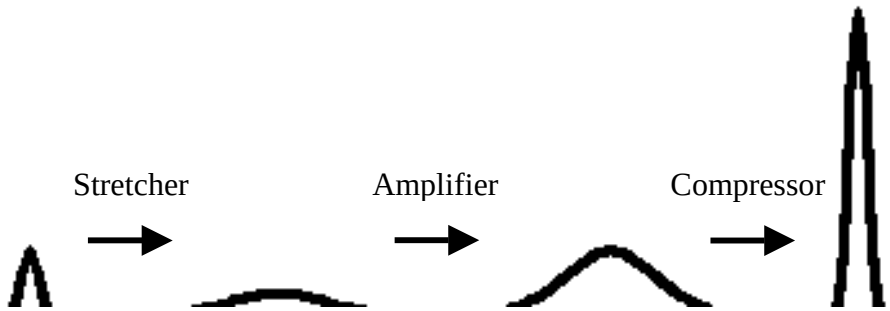

Figure 3.3 In chirped pulse amplification the seed pulse from the oscillator is stretched, amplified, and then recompressed. This prevents high intensity laser damage in the amplifier.

The pulse stretcher is designed to linearly chirp the pulse, while maintaining a small spatial profile. A linearly chirped pulse is temporally spread out such that there is a linear relationship between different colors and the time at which each color passes a set point in space. A schematic diagram of the pulse stretcher is given in figure 3.4. A femtosecond pulse from the oscillator is diffracted off of a grating, expanding it spatially. The pulse then reflects off of a second identical grating such that all of the colors are collinear. At this point some frequencies have traveled farther than others introducing temporal dispersion or a chirp. A second set of identical gratings reconstructs the pulse spatially, while doubling the temporal chirp. To minimize its cost and size, the actual amplifier only has one grating, using mirrors to reflect the pulse off of it four times.

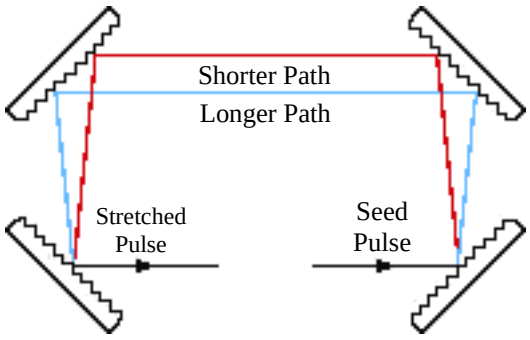

Figure 3.4 Four gratings are used to temporally stretch or chirp the seed pulses.

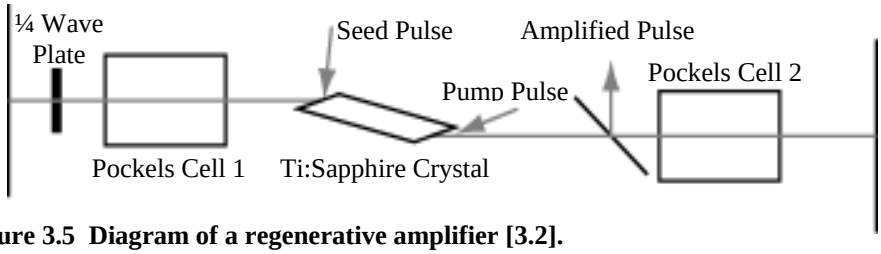

Figure 3.5 Diagram of a regenerative amplifier [3.2].

The regenerative amplifier uses polarization to isolate and amplify 1 seed pulse out of every ~80,000 pulses from the oscillator. The amplifier consists of a resonator that contains a quarter wave plate, 2 Pockels Cells, a polarizing beam splitter, and a Ti:Sapphire rod, as depicted in figure 3.5. The laser rod and the polarizing beam splitter are coated to reflect vertically polarized light while transmitting horizontally polarized light, such that only horizontally polarized pulses remain in the regenerative cavity. The timing of the 1st Pockels Cell is adjusted to choose a seed pulse from the oscillator that nicely overlaps with the pump pulse. Two passes through the quarter wave plate rotate the vertically polarized seed pulse from the oscillator to horizontal polarization. Turning on the Pockels Cell right after the desired pulse passes it, adds another quarter wave rotation per pass, trapping the chosen pulse in the cavity and rejecting all later pulses. After the chosen pulse completes ~20 cycles through the regenerative cavity, the second Pockels Cell is activated just before the pulse enters it coming from the laser rod. This rotates the pulse back to vertical polarization, and it is reflected out of the amplifier cavity by the polarizing beam splitter [3.2].

Finally, the compressor is a mirror of the stretcher. The stretcher induces a positive chirp; the compressor introduces an identical negative chirp; and a high energy pulse leaves the system.

Using a 10 mJ, 527 nm pulsed Nd:YLF Spectra Physics, Merlin pump laser for the regenerative cavity, the Spitfire emits 125 femtosecond pulses centered about 800 nm, with energies greater than 500 μJ per pulse. With proper focusing, this pulse energy is high enough to modify any glass.

3.4.3 Fiber Lasers

Fiber lasers have the same basic sections as conventional laser systems. The defining difference between conventional and fiber lasers is the nature of the active gain region. Conventional systems have small active crystals, a few centimeters long, with very high gain. In contrast, fiber lasers have large active regions, several meters long, with moderate gain. These differences lead to different pulse amplification and dispersion compensation schemes.

Unlike conventional systems that use regenerative amplifiers in which the pulse passes through the active region many times to increase its pulse energy, fiber lasers typically use linear amplifiers. The longer active region in fiber systems allows for linear pulse amplification in which a low energy pulse enters and a high energy pulse exits after a single pass. Linear amplifiers can operate at much higher pulse repetition rates than regenerative amplifiers, though linear amplifiers are also more susceptible to laser damage.

This risk of laser damage can be minimized by carefully controlling the pulse intensity within the laser, through adjustments to the temporal pulse width. Unlike conventional systems that use gratings to introduce a set chirp; fiber lasers use dispersive fibers to continually adjust the pulse width. Sections of positively and negatively dispersive fiber are coupled together to ensure that a relatively long pulse is maintained throughout the fiber laser. The pulse is only allowed to compress just before exiting the system, minimizing the risk of damage elsewhere.

3.5 The Confocal Microscope

Femtosecond laser writing is intrinsically limited to the focal volume of the microscope objective, as discussed in chapter 2. Unfortunately spectroscopy experiments that use an Ar^+ laser have a linear response. This means that while there will still be a greater response at the focus due to the higher intensity, all of the material the light passes through both before and after the focus will also give a response. There is an enormous amount of material relative to the size of the focal volume, as shown in figure 3.6. And, trying to detect changes within the focal volume is equivalent to looking for a needle in a haystack.

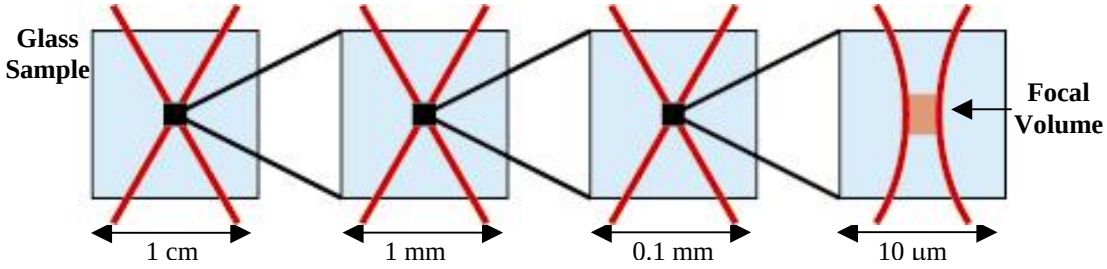

Figure 3.6 Image of a laser focused in a large block of material (left), relative to the actual size of the focal volume (progressing to the right).

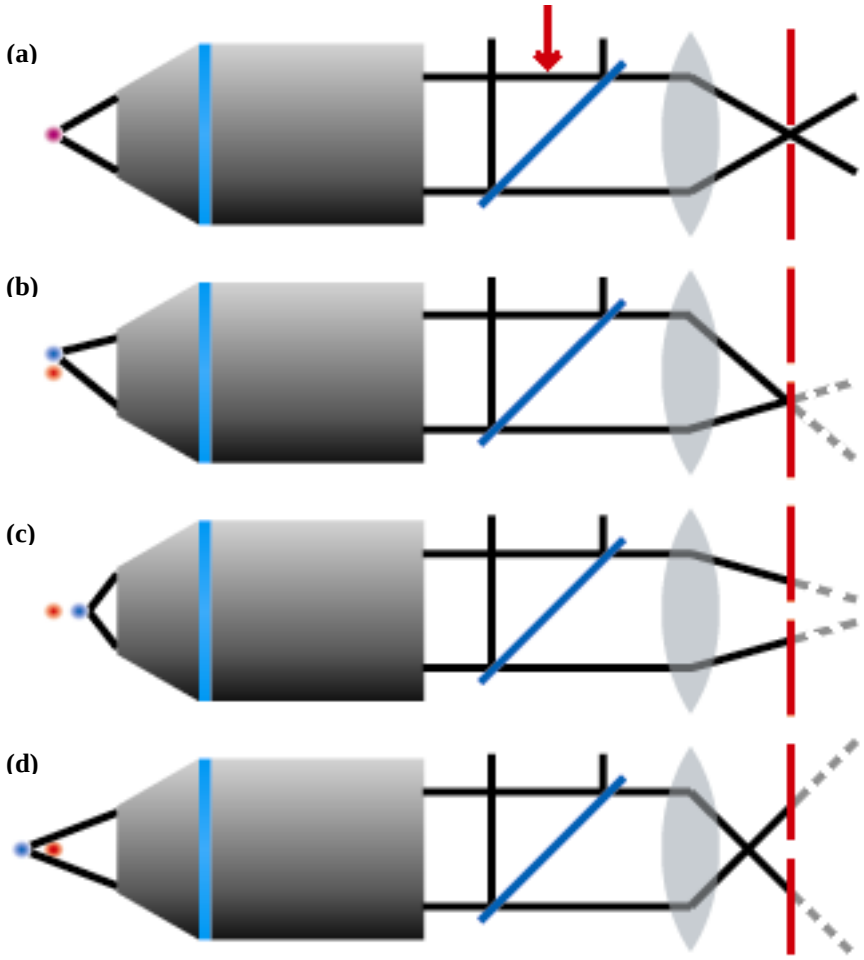

Figure 3.7 The spatial filtering effects of a confocal microscope. The red dot denotes the focal point of the microscope objective, and the blue dot denotes the point of origin for the light ray traces. a) shows light from the focal point passing through the spatial filter, while b, c & d) show light from surrounding points being eliminated. Note: the light between the microscope objective and the lens is only collimated for case (a).

A confocal microscope eliminates the vast majority of the light that does not originate from the focal volume of the microscope objective, allowing us to find the metaphoric needle. A spatial filter consisting of a pair of lenses focused on each other with a pinhole at their mutual focal point is the key element of a confocal microscope system. The focal, point of the lenses is where the real space image of an object at infinity, or the focal point of an infinity corrected microscope objective would condense to a point, as shown in figure 3.7a. The pinhole eliminates everything in the focal plane except the focus

enhancing the x, y resolution, as shown in figure 3.7b, and it substantially reduces light coming from points before or after the focal plane enhancing the z axis resolution, as shown in figures 3.7c & 3.7d.

3.6 Operating Procedures

The information presented in this dissertation was produced using three types of procedures: laser alignment, femtosecond laser waveguide fabrication, and confocal spectroscopy. This section discusses the experimental procedures in general; specific details are provided with the results for each experiment.

3.6.1 Alignment Procedures

To obtain good results that are comparable between experiments, it is necessary to align the microscope system before conducting each experiment. The beam paths from the Ti:Sapphire and argon ion lasers to the sample are aligned first. Afterwards, the laser back reflection is used to align the rest of the confocal microscope. The item numbers that follow many of the optical components in the following procedure refer to the schematic diagram, shown in figure 3.1.

Starting with the Ti:Sapphire beam line: A half wave plate (item 6) and a polarizing cube beam splitter (item 7) are centered in the path of the laser as it exits the Ti:Sapphire

system (item 5). After the beam splitter, two near IR mirrors (item 10, only 1 mirror is shown) are used to guide the beam to the dielectric beam splitter (item 17).

With the microscope objectives (item 13) removed, the dielectric beam splitter (item 17), and the mirror before it (item 10) are adjusted such that the laser beam passes through the center of the removable iris (item 14) and such that the beam illuminates a small target spot marked on a barrier several feet past the objective mounts (item 11). A low magnification (5X or 10X) microscope objective (item 13a or 13b) is inserted while blocking the beam. Unblocking the laser, the objective is moved perpendicular to the beam to until a circular far field image is centered at the same spot on the barrier as the unfocused beam. If the far field image is not circular, then the microscope objective is tilted with respect to the beam path.

After the microscope has been aligned with the femtosecond laser, the Ar^+ laser (item 1) is aligned such that it passes through the center of the iris (item 14) and the writing objective (item 13a or 13b), overlapping the femtosecond laser. A quarter wave plate (item 3) and a 488 nm notch filter (item 2) are centered in the path of the laser as it exits the laser head. A mirror (item 4) and a dielectric beam splitter (item 18) are then adjusted to couple the laser beam into the microscope. Note: it is also possible to align the argon ion laser first, and to then overlap the femtosecond laser with it.

Once both lasers have been aligned, the detection beam path is aligned using the back reflection of the argon ion laser off of a perpendicular mirror that is placed in the focal

plane of the microscope objective. The first confocal lens (item 21) is inserted, ensuring that the beam passes through the center of the lens and that the resulting spot is centered on the same point as the unfocused beam. The second confocal lens is inserted, making certain that the resulting spot precisely overlays the spot produced by the beam without the lenses. The pinhole (item 22) is inserted into the foci between the lenses using fine x, y, and z adjustments to maximize the power transmitted through the pinhole. Two mirrors are adjusted to guide the beam into the PMT (item 24). A final lens (item 25) and the last two mirrors before it are adjusted to couple the signal into the spectrometer (item 26). They are adjusted such that the beam fills the grating and the spectrometer entrance slit is ~12 μm wide. Note, minimizing the spectral line width of a narrow calibration source can be used to fine tune the distance between the lens and the entrance slit.

3.6.2 Waveguide Writing Procedure

The sample (item 12), a glass block, is attached to the sample mount using double sided tape, and either transmission imaging or the back reflection of the laser are used to ensure that the sample is orientated perpendicular to the objective (item 13a or 13b). The CCD camera (item 20a) is used to monitor both procedures. When using transmission imaging: the microscope is focused on the front surface of the sample (the surface closest to the microscope objective being used), the sample is back illuminated with a white light, and the sample is translated perpendicular to the laser beam path. If the sample is properly orientated its front surface will remain in focus while the sample is translated. When using the back reflection of the laser, the microscope is focused on the front

surface of the sample, and the sample is translated back and forth parallel to the beam path, bringing the front surface into and out of focus. If the sample is properly orientated, the reflected image of the laser will remain circular in shape as it expands and contracts about a fixed central point.

Once the microscope and the sample have been properly aligned, waveguides or other structures are fabricated by scanning the sample with respect to the focus of the microscope objective. Typically a 10, 20, or 50X objective is used with longitudinal scanning, though the system is capable of transverse scanning. The pulse intensity is adjusted by rotating the ½ wave plate (item 7), which controls the polarization of the femtosecond laser beam as it enters the polarizing beam splitter (item 8). The maximum and minimum powers transmitted relate to the initial intensity, and the approximately 100 to 1 horizontal polarization of the spitfire laser beam. Additional neutral density (ND) filters (item 6) can be added before the half wave plate if lower pulse energies are desired.

Transmission microscopy with the CCD camera (item 20a) is normally used to monitor the writing process. It can be used to quickly determine how the laser system is modifying the material, showing the effects of adjusting the pulse energy in real time.

3.6.3 Spectroscopy Procedure

The hardest part of performing high resolution spectroscopy is to locate the modified material. Three methods are used to ensure that the Ar^+ laser is precisely focused on the modified region. The first is to ensure that the focal spot of the Ar^+ laser exactly overlaps the focal spot of the femtosecond laser before writing any lines; and to then reposition the stages to regions that should have been modified, without observing the sample. This technique only works if the sample has not been manually repositioned since the lines were written, it is also necessary to accommodate for the effects of hysteresis in the stepper motors. The second method is to locate the modified area using the Ar^+ laser set to low power as a coherent light source for imaging the sample against a far field screen (item 11). The third method is to mark the point on the TV monitor at which the back reflection of the Ar^+ laser hits the CCD camera used for transmission imaging (item 20a). White light transmission images of the modified features can then be overlapped with that point to center the Ar^+ laser on those features, while the Ar^+ laser turned off. Comparing the 2^{nd} and 3^{rd} methods, the second method operates on the same principals as DIC microscopy and is the most sensitive method for locating small changes in the material. Unfortunately, any exposure to the Ar^+ laser can eliminate some of the fluorescent defects we would like to observe, in which case the third method is preferable.

After the modified material has been located spectra are collected using the spectrometer. The 300 grove per mm grating is used for fluorescence spectroscopy and the 1200 grove

per mm grating is normally used for Raman spectroscopy. Fluorescence spectra are typically collected before Raman spectra, because the fluorescent defects are more likely to photobleach (disappear) as a result of exposure to the Ar^+ laser. Once specific spectral features have been identified it is possible to use additional spectral filters with either the spectrometer or the PMT to create images of the spatial extent of that feature, by collecting data while raster scanning the sample; the sample is normally stopped to collect data for each point to avoid smearing in the final image. Both detectors have advantages: using the spectrometer provides detailed spectral information; using the PMT is roughly a hundred times faster.

References

3.1 Tsunami, Mode-Locked Ti:sapphire Laser, User's Manual, Spectra Physics Lasers, Mountain View, CA, 1995.

3.2 Spitfire LCX, User's Manual, Spectra Physics Lasers, Mountain View, CA, 1998.

Chapter 4

High Spatial Resolution Spectroscopy of Femtosecond Laser Modified Fused Silica

4.1 Motivation

In previous studies described in section 2.4, femtosecond lasers were used to modify large volumes of fused silica. Spectra of these regions revealed that the laser modification creates a large concentration of NBOHC defects, and causes an increase in the relative concentration of three-membered rings, indicating local densification. This raises an obvious issue: if one region has been densified, there has to be another region that has been rarified. Therefore, it is desirable to obtain information about the structural changes within individual waveguides in fused silica with high spatial resolution.

This would also help distinguish between the thermal diffusion and shockwave generation energy dissipation mechanisms. If a micro-explosion took place, it is predicted that the modified region would consist of a high-density shell surrounding a low-density core or even a void. On the other hand, rapidly quenching fused silica would result in a high-density central region, with low-density peripheral regions.

The results in this chapter are divided into three subsections. The first discusses Raman and fluorescence spectra collected from longitudinally written waveguides in bulk fused silica. The confocal microscope used to collect these spectra has ~1.5 μm spatial

resolution. In order to better measure spatial variations across regions modified with fs laser pulses data, it is desirable to have lines that are substantially larger than this resolution. In the second subsection spectra were collected from large diameter lines that were up to 40 μm across. In the third subsection spectra were collected from Bragg gratings produced with patterned writing in silica fibers. In these gratings periodic structural modifications occur on an even smaller length scale than in the small-diameter waveguides, allowing us to experimentally assess the resolution of the confocal microscope.

4.2 Experiment

Waveguides were directly written in fused silica (Corning 7940) using the in-house, amplified, 1 kilohertz, Ti:Sapphire femtosecond laser, described in chapter 3. The laser operated at 800 nm with ~125 fs pulses, a repetition rate of 1 kHz, and 0 to 5 μJ pulse energies. It was focused into silica cubes using a 50X 0.55 NA objective, and the sample was moved longitudinally at 20 μm/s. To create larger-diameter modified lines the microscope objective was replaced with a 6 centimeter focal length singlet lens resulting in a spot size of ~10 μm. The energy of the femtosecond laser pulses was increased up to 35 μJ to maintain an intensity at the focal point similar to the intensity used for fabricating regular, small-diameter waveguides. All other processing variables remained the same as when using the microscope objective.

A second 1 kHz, 800 nm, 125 fs Ti:sapphire laser was used by our collaborators in Canada (Dr. S. Mihailov and C. Smelser) to fabricate Bragg gratings in all-silica-core optical fibers using an interference pattern. Two-beam interference was used with a 4.284 μm-pitch phase mask to create 2.142 μm-pitch gratings. A stationary fiber was exposed to approximately 10,000 pulses with an average intensity of $1.3 * 10^{13}$ W / cm^2 to fabricate each grating [4.1].

A scanning confocal microscope was used to simultaneously collect Raman and fluorescence spectra of the samples. All of the waveguides and the interference patterns were analyzed by focusing a 50 mW, 488 nm Argon ion (Ar^+) laser into the sample using a 100X 0.73 NA microscope objective. The backscattered Raman and back-emitted fluorescence spectra were collected using the same objective; and a 0.25 m spectrometer with a 300 groove mm^{-1} grating and a liquid nitrogen cooled CCD array detector, with a 5 minute acquisition time for the Raman spectra and a 1 second acquisition time for the fluorescence spectra. At least three spectra were collected from different points along the center of each waveguide. The spatial profiles of select waveguides and of the fiber Bragg gratings were measured by scanning the sample with respect to the objective focus with a 1 μm step size traveling perpendicular to (across) the waveguides, and a 3 μm step size traveling along the waveguides. Images of the fiber Bragg gratings were generated using the PMT with a collection time of 0.1 s per point and scanning the sample with 161, 1-μm steps across the fiber and 41, 0.5-μm steps along the fiber.

Spectra of the large-diameter modified lines were collected using a 50X 0.55 NA microscope objective to focus the Ar^+ laser. A 1200 grooves mm^{-1} grating with a 30 min acquisition time was used for Raman spectroscopy, and a 300 grooves mm^{-1} grating with a 2 min acquisition time was used for fluorescence spectroscopy.

4.3 Results and discussion

The results are divided into three subsections based on the nature of the features being observed: 1) Waveguides longitudinally written in bulk fused silica, 2) Large-diameter lines longitudinally written in bulk fused silica, and 3) Bragg gratings produced using a phase mask in silica fibers.

4.3.1 Waveguides in bulk fused silica

Both Raman and fluorescence spectra were collected for individual waveguides fabricated in fused silica using our in-house femtosecond laser. These waveguides were fabricated with a 50X microscope objective and pulse energies varying from 0.5 to 5 μJ; they had diameters ranging from 4 to 8 μm. Qualitatively these spectra, samples of which are shown in figure 4.1, closely match those previously obtained for large modified volumes of fused silica.

Quantitative calculations of the Raman and fluorescence peak areas were performed on the waveguides, for a more exact comparison with the earlier results. The areas of the

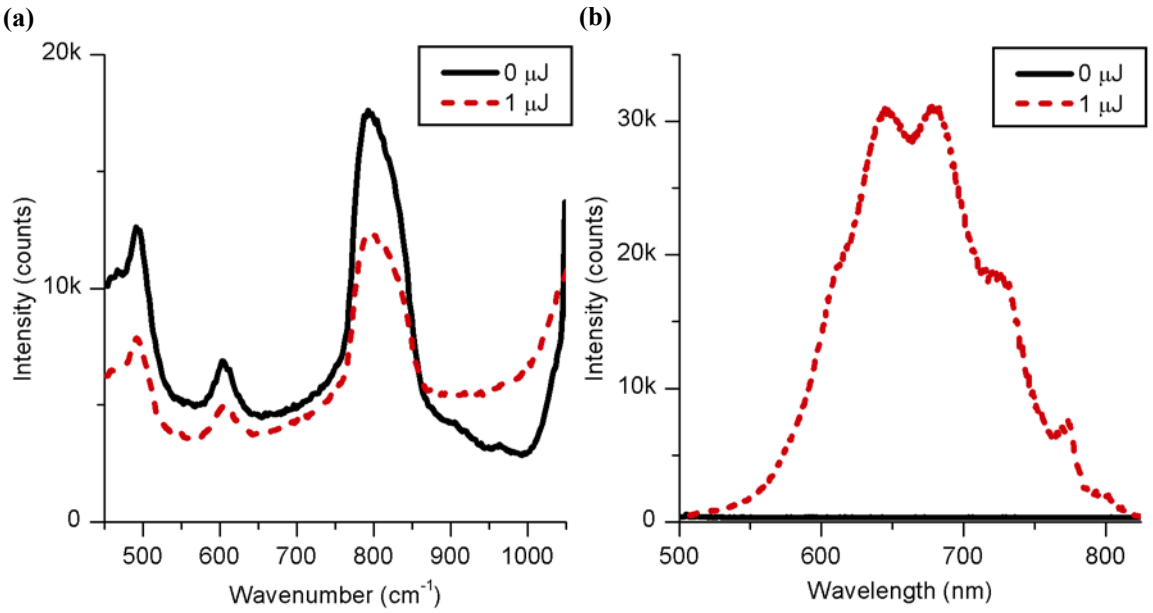

Figure 4.1 a) Raman and b) fluorescence spectra of modified and unmodified fused silica.

605 cm^{-1} and 800 cm^{-1} peaks were calculated using a straight-line baseline from 570 to 645 cm^{-1} for the 605 cm^{-1} peak, and from 750 to 870 cm^{-1} for the 800 cm^{-1} peak. The ratio of the 605 cm^{-1} Raman peak divided by the 800 cm^{-1} Raman peak was calculated to provide a measure of the relative concentration of 3-membered rings. The total fluorescence was calculated as the area under the spectrum from 555 to 800 nm, with a zero intensity baseline. The peak areas for each waveguide were normalized to the peak areas in unmodified glass. These results are listed in Table 4.1. Comparing them to the earlier results for large modified volumes listed in section 2.4, the fluorescence intensities are similar, but the relative concentration of 3-membered rings was less. This decrease indicates that the spectral signal for single lines comes from a mixture of modified and unmodified material. The data from single waveguides thus represents a minimum value, rather than an exact value. As such, relative comparisons of waveguides in the same sample should be valid, but care must be taken when comparing Raman spectra collected

Table 4.1 Normalized 605 / 800 cm^{-1} Raman peak ratios and fluorescence intensities for individual waveguides written using a 50X 0.55NA objective.

Pulse Energy (μJ)	Raman Signal (a.u.)	Fluorescence signal (a.u.)
0	1.0	1
0.5	1.1	170
2.5	1.4	500
5	1.8	1050
10	2.0	1300

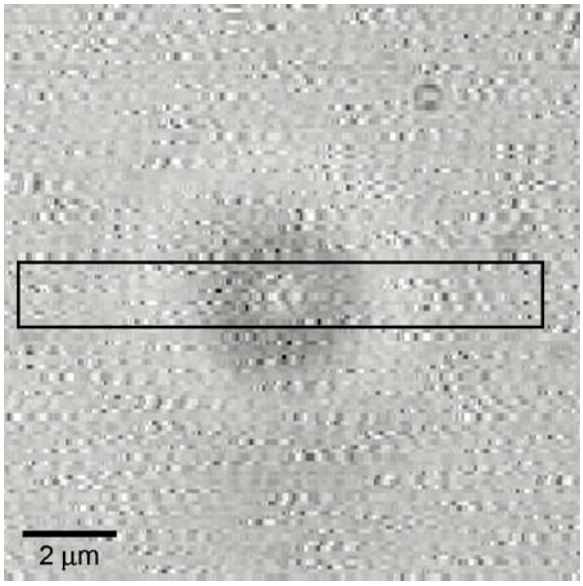

Figure 4.2 A white light microscope image of the end-face of a waveguide written using a 50X objective and a pulse energy of 0.5 mJ. The black box indicates the region from which spectra were collected to produce the spatial cross-sections shown in figure 4.3.

from different samples. There is almost no intrinsic fluorescence in pure fused silica; therefore the fluorescence signal only comes from the modified material.

Additional spectra were collected scanning across the end-faces of several modified lines, as indicated in figure 4.2. There is a slight rise in the relative concentration of 3-membered rings, in the line written with a pulse energy of 1.7 μJ, indicating that local densification occurred in the center of the modified line, shown in figure 4.3c. This increase was largely the result of a decrease in the total signal from the silica network represented by the intensity of the 800 cm^{-1} Raman peak, shown in figure 4.3b. An

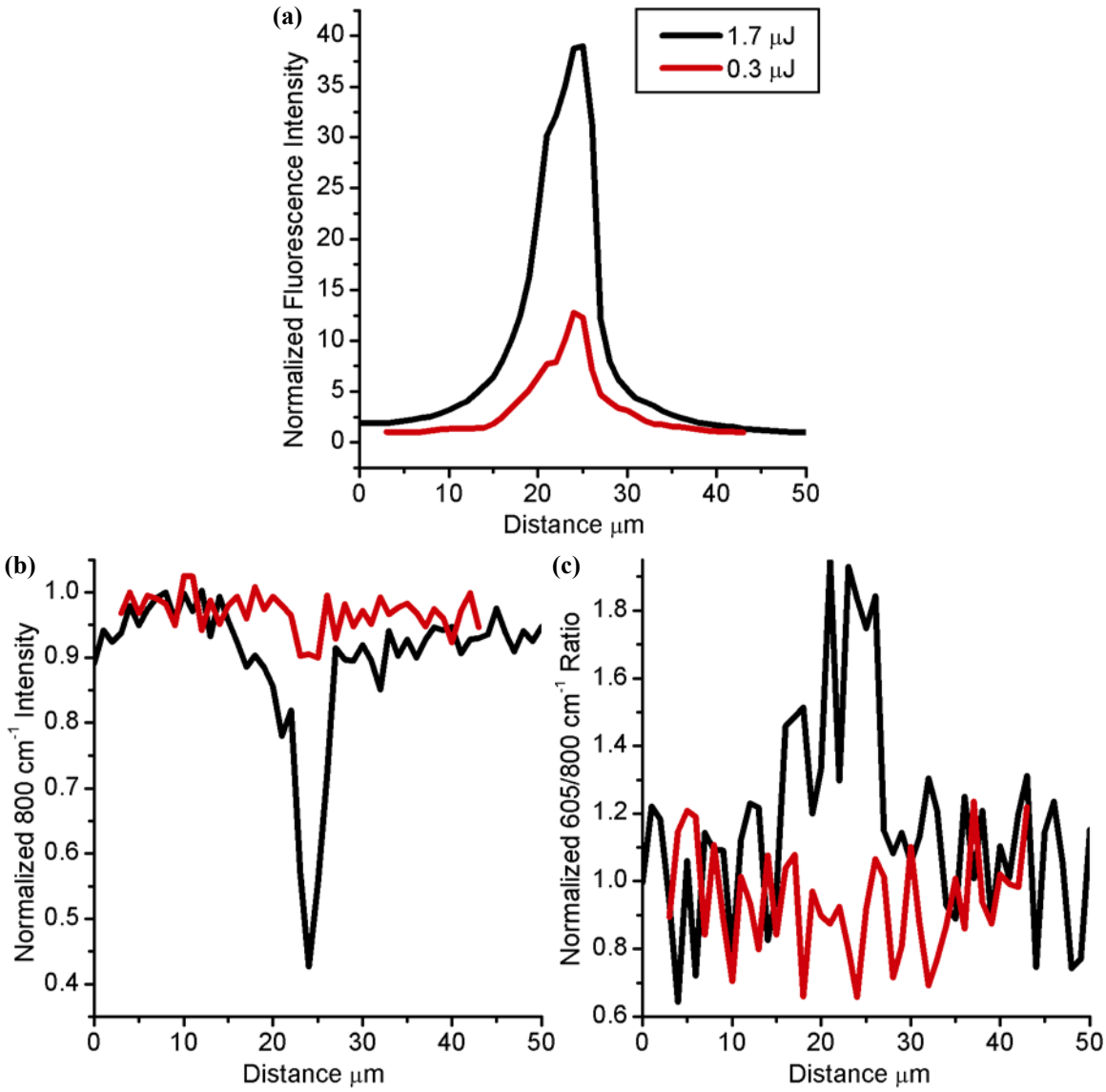

Figure 4.3 The intensity of several spectral features as a function of spatial position collected while scanning across the waveguide shown in figure 4.2: a) the area of the fluorescence peak, b) the area of the 800 cm^{-1} Raman peak, and c) the ratio of the 605 / 800 cm^{-1} Raman peaks.

increase in the fluorescence from non-bridging oxygen hole center (NBOHC) defects was observed across the same region, as shown in figure 4.3a. It appears that the width of the fluorescent signal is slightly larger than the width of the Raman signal indicating that defects may form beyond the densified region, though this assertion is uncertain because of the limited scan resolution of the confocal microscope.

4.3.2 Large-diameter lines in bulk fused silica

Large diameter modified lines were created and analyzed in order to obtain more meaningful information about the spatial profile of the modified regions [4.2]. The diameter of these lines varied from 6–7 μm using 9 μJ laser pulse energy, which is slightly smaller than the 10 μm diameter of the laser focus, to roughly 40 μm using 25 μJ laser pulse energy. Spectra were collected from the cross-sectional regions outlined in yellow on figure 4.4. The fluorescence and total Raman cross-sections have similar intensity profiles to those observed for the narrow waveguides, as shown in figure 4.5.

The fluorescence results from the large lines indicate that there is a large concentration of NBOHC defects in the center of the modified regions. For the Raman spectra, the results are more complicated. Unlike the narrow waveguides, the large lines do not have an increase in the concentration of 3-membered rings, as noted in figure 4.6. This disparity raises some concerns about directly comparing the normal and large waveguides. If we use the 605 cm^{-1} / 800 cm^{-1} peak intensity ratio as a measure of the local density; then the

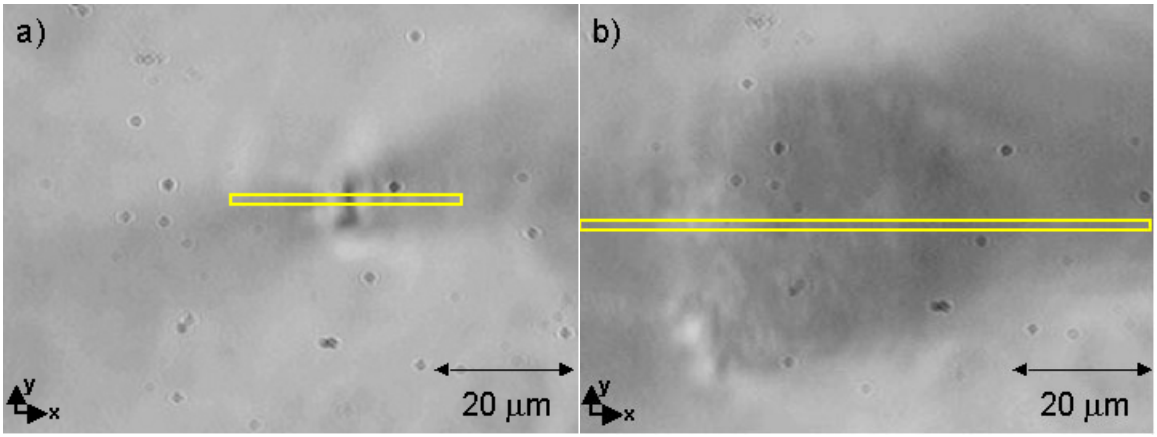

Figure 4.4 White light microscope images of the cross-sections of modified lines written in fused silica with a 6 cm focal length lens and (a) 9 μJ and (b) 25 μJ fs laser pulse energy.

(a)

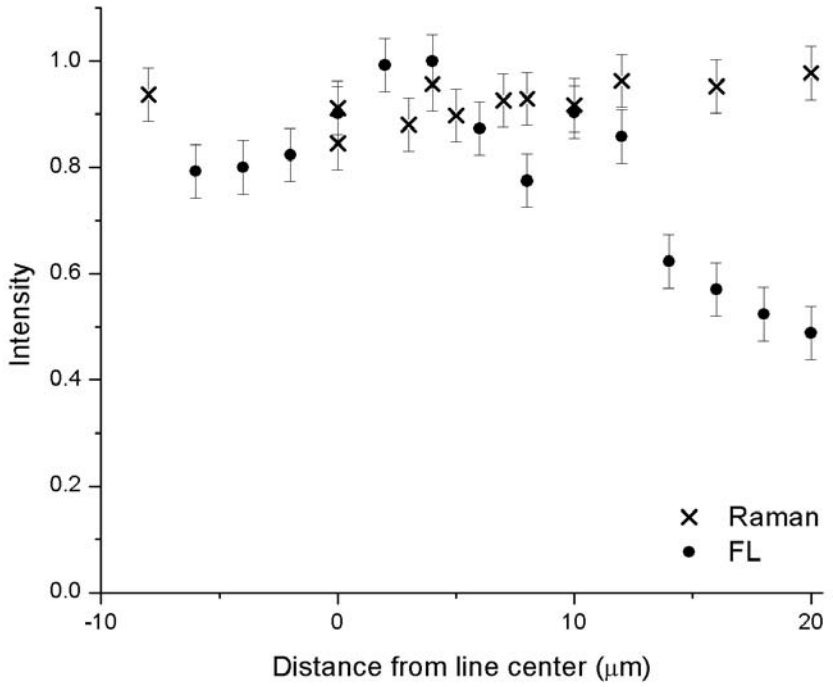

(b)

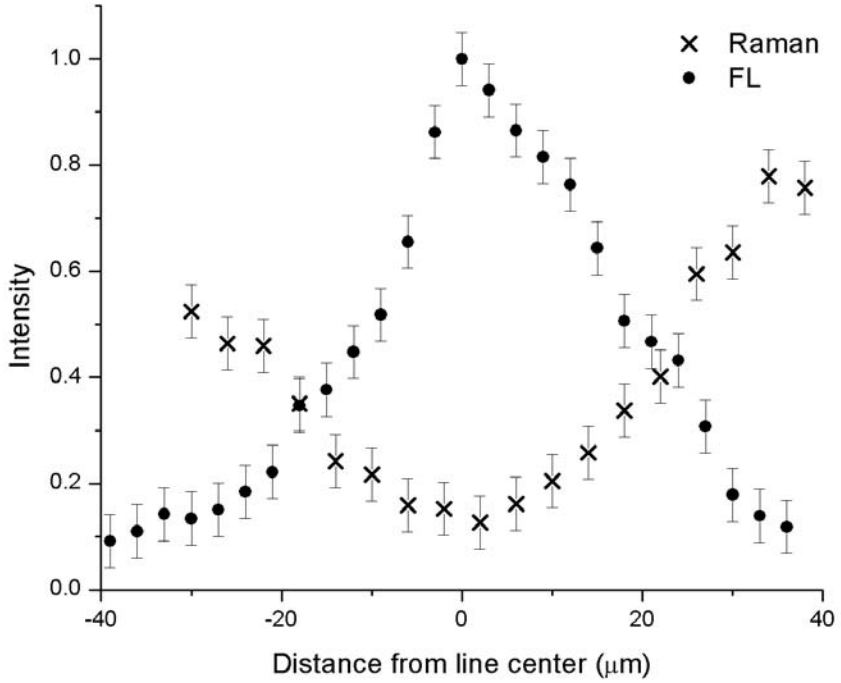

Figure 4.5 Fluorescence (●) and Raman (x) intensity as a function of distance from the line centre for lines written in fused silica with a 6 cm focal length lens and (a) 9 μJ and (b) 25 μJ fs laser pulse energy.

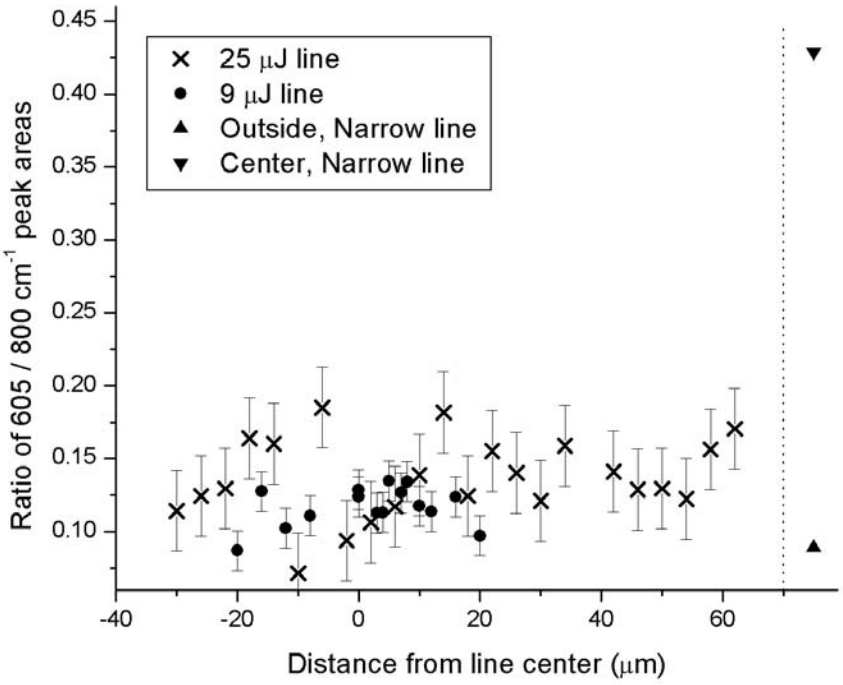

Figure 4.6 The intensity ratio of the 605 and 800 cm−1 Raman peaks as a function of distance from the line centre for lines written in fused silica with a 6 cm focal length lens and 9 μJ (●) and 25 μJ (x) fs laser pulse energy. For comparison the 605 cm−1/800 cm−1 ratio in the centre of (▼) and outside (▲) a narrow line written with a 50×, 0.55NAobjective and 4 μJ fs laser pulse energy is also shown.

density in the center of the large diameter lines is only slightly higher than that of the unmodified glass, and there is no variation in the local density across the modified regions. That still leaves the decrease in overall Raman intensity seen in figure 4.5 to be explained. One could argue that the central region contains a rarefied amorphous material. The overall Raman intensity can be thought of as resulting from the product of the number of 'bonds' and the 'bond polarizability'. A rarefied material with a high concentration of broken bonds could account for a decrease in Raman intensity together with an increase in fluorescence intensity. However, the change in Raman signal could also be the result of the fact that a substantial fraction of the signal is lost due to elastic scattering/absorption, as it travels through the sample from the plane of observation

(focal plane) to the detector. This loss will be higher in the modified region since it is optically less homogeneous especially for higher fs laser fluences. The total loss will scale with the laser fluence, and will increase as the focal plane of observation moves deeper into the sample. Further experiments in which the focal plane (plane of observation) was moved deeper into the sample indicate that this decrease is at least partially due to scattering/absorption. These effects were enhanced by the use of greater pulse energies. Of course in this scenario, the fluorescence signal would experience a similar loss, and taking this into account means that the concentration of NBOHC defects generated in the modified region is even higher than what was detected.

All together these results do not show an unambiguous indication of density variations across the larger-diameter modified lines. A recent study by Taylor et al. [4.3], in which an ultrahigh-resolution (20 nm) spatial profiling technique—based on a combination of selective chemical etching and atomic force microscopy—was used to probe index/structural variations across a fs laser-modified line of 2 μm diameter, also did not find any low-density region. It is possible that the focusing conditions used in our writing experiments may have led to self-focusing [4.4] which could have resulted in a less effective deposition of the laser energy in the focal volume, but for the writing conditions used in [4.3] self-focusing does not play a role.

4.3.3 Bragg gratings in silica fibers

The fiber Bragg grating, shown in figure 4.7, was fabricated with similar peak intensities to the lowest intensities used in waveguide fabrication, such that we can compare the results. The white outline in figure 4.7a indicates the area scanned using the spectrometer, and the black outline indicates the area scanned using the PMT. Both fluorescence and Raman data were collected. The Raman results for the fiber gratings were inconclusive. They didn't show a substantial change in either the total Raman intensity or in the concentration of 3-membered rings as measured by the ratio of the 605 cm^{-1} / 800 cm^{-1} Raman peak. It is difficult to say whether this null result actually indicates that no change occurred or if there was a change that was too small to measure.

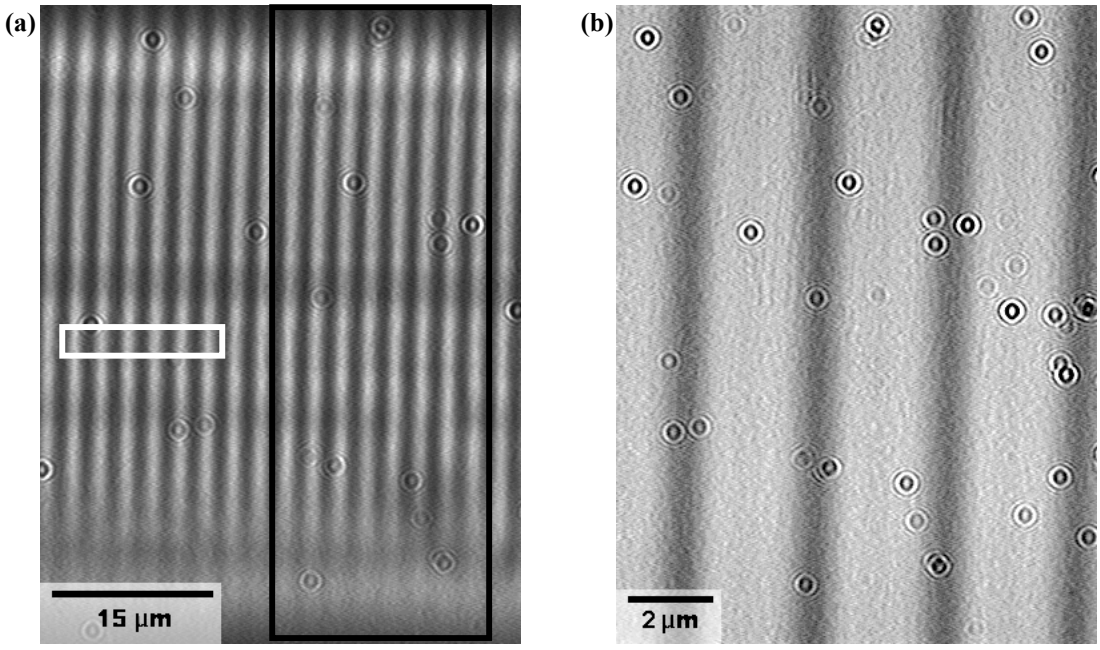

Figure 4.7 White light microscope images of a fiber grating collected with a) a 20X objective, and b) a 100X objective. Spectra were collected from the outlined regions.

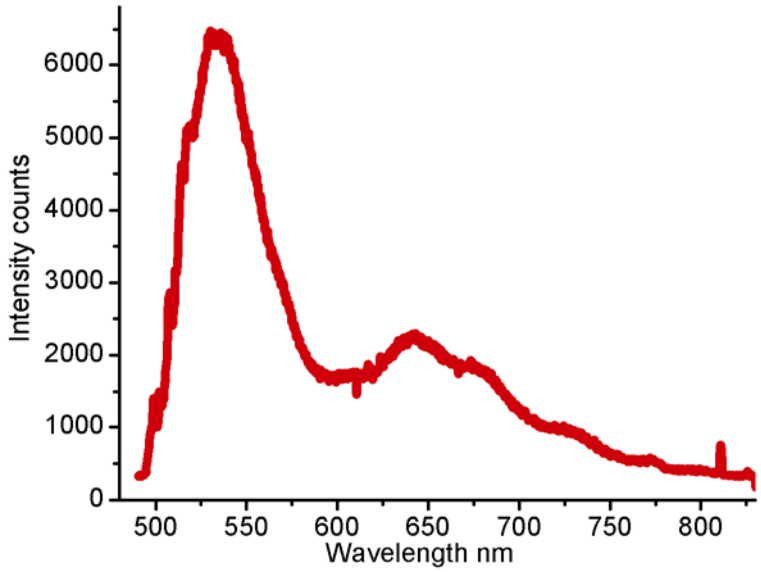

Figure 4.8 A sample fluorescence spectra from the fiber grating. Note that there are two peaks at 540 and 650nm.

There was a clear correlation between the modification pattern and the fluorescence signal from the fiber gratings. Two distinct sources of fluorescence were observed in the spectra of the fiber gratings, shown in figure 4.8. The peak centered around 650 nm is a result of the NBOHC defects discussed earlier [4.5]. The peak centered around 540 nm matches the characteristics of self trapped exciton ($E_{\delta}^{'}$) defects from very small silicon nano-clusters that several groups have reported seeing in γ-irradiated fused silica [4.6-4.8]. The fluorescence photobleaching rate can be used to further distinguish the two types of defects, because the $E_{\delta}^{'}$ defects bleach about 25% faster than the NBOHC defects as shown in figure 4.9. Looking back at earlier data the fluorescent peak from the $E_{\delta}^{'}$ defects are predominant in many of the waveguides produced using low pulse energies, which are barely sufficient to modify the material.

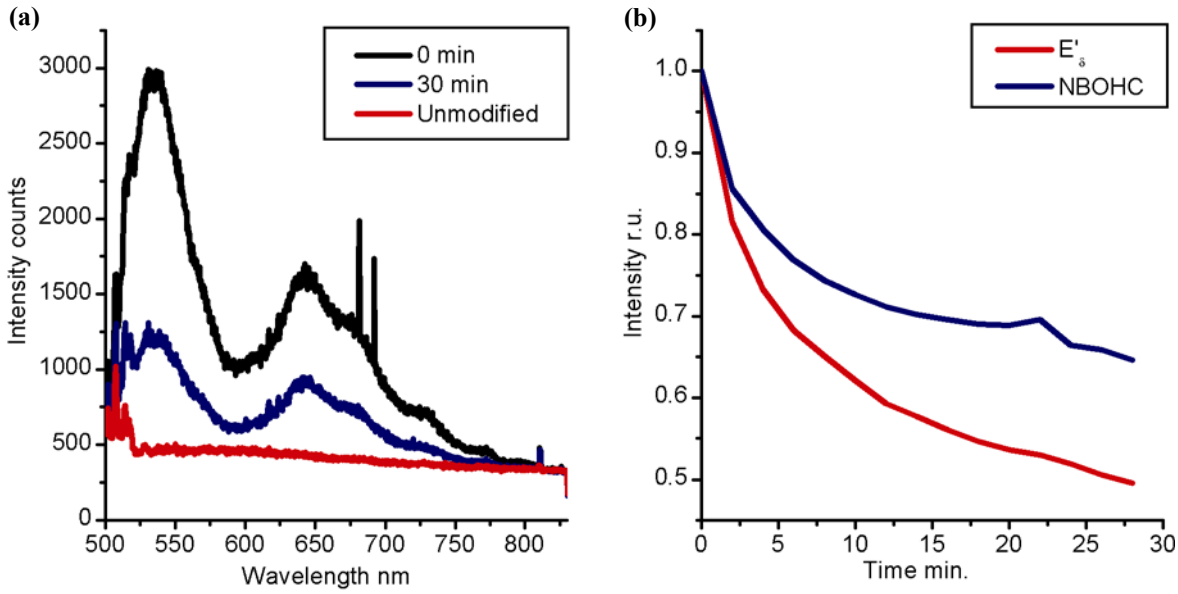

Figure 4.9 Fluorescence photobleaching of fiber gratings written with a fs laser: (a) shows the full spectra before / after bleaching, and (b) shows the normalized peak intensities as a function of time.

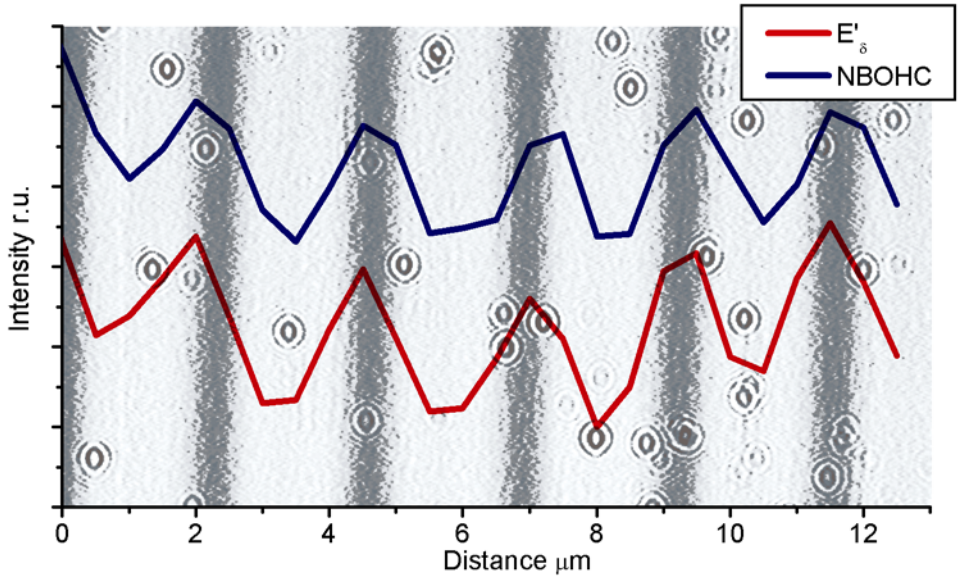

Figure 4.10 Intensity of the fluorescence peaks as a function of spatial position, overlaid by a white light image of the grating.

Looking at the fluorescence as a function of spatial position, the structure of the grating is easily visible. Figure 10 shows that both the concentrations of NBOHC and $E_{\delta}^{'}$ defects mirror the 2.14 micrometer line spacing, visible in the white light image. It is also possible to quickly map the grating structure across the entire fiber using the total fluorescence intensity, as in figure 4.11a, or using the fluorescence from one type of

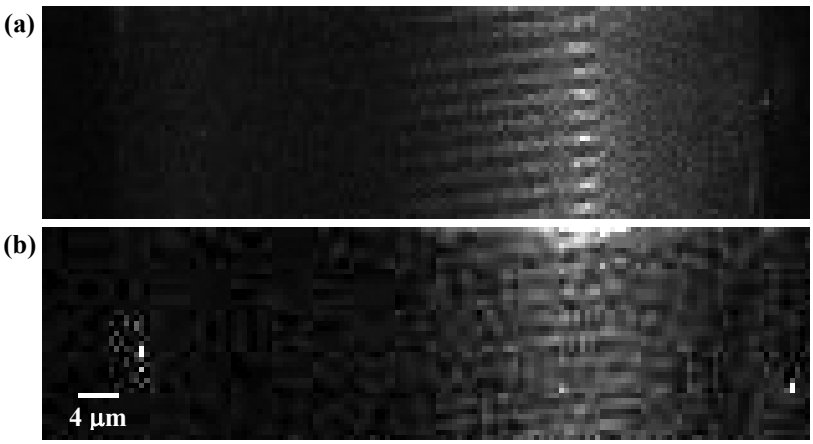

Figure 4.11 Fluorescence images of the fiber bragg grating: (a) the total fluorescence, and (b) the fluorescence from NBOHC defects.

defect, as in figure 4.11b. This rapid mapping of the modified pattern could potentially be used as a quality control method.

The grating profiles can be used to experimentally estimate the resolution of the confocal microscope. Here the resolution is defined as the minimum distance between two identical points, at which the individual points can be distinguished. The resolution of our microscope is clearly better than 2.14 μm because the grating lines shown in figure 4.10 are easily distinguishable; however it is hard to precisely say how much better because we do not have any finer patterns. It is possible to roughly estimate the resolution of the microscope using the pattern in figure 4.10 because it is only partially resolved; meaning that while the grating lines are clearly distinguishable, the signal does not return to its background level between the lines. A convolution of a 2.14 μm spaced comb pattern and a Gaussian peak was used to simulate the grating pattern, approximating the grating lines as having a Gaussian profile. The width of the grating lines in the white light images (figure 4.7b) was measured to be ~0.73 μm; this width was used as the full width at half maximum (FWHM) of the Gaussian peak. The fluorescence

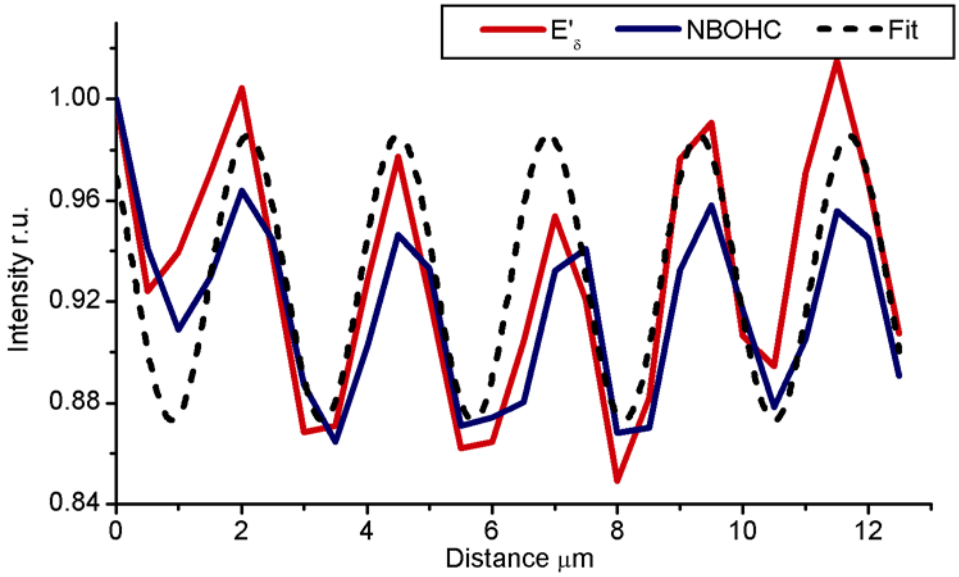

Figure 4.12 Intensity of the fluorescence peaks in the grating as a function of spatial position, overlaid by the best fitting pattern produced assuming that the grating lines are delta functions.

pattern was simulated by a second convolution of the simulated grating pattern and a Gaussian microscope focus. A least square fit was used to match the simulated fluorescence pattern with the measured patterns in figure 4.10. Both of the spectral patterns in figure 4.10 were normalized to their intensity at x = 0 to more easily fit both patterns. In the fitting process the amplitude and the full width at half maximum of the Gaussian microscope focus were allowed to vary as free parameters. The best fit yielded a resolution of ~1.2 μm for the confocal microscope. It is possible that the apparent grating line width in the optical image is also broadened by the microscope system used to collect the white light image. In that case the actual grating pattern has lines that are narrower than 0.73 μm; this would result in the fit giving a poorer (lower) resolution for the confocal microscope. A second calculation was performed to find the minimum resolution of the confocal microscope, by using a delta function to represent the individual grating lines. This calculation yielded a resolution of ~1.4 μm, with the fit shown in figure 4.12.

4.4 Summary

Spectra were collected from the center of individual waveguides fabricated using a 1 kHz pulse repetition rate femtosecond laser. The fluorescence and Raman signals match those observed for larger modified regions, showing an increase in the concentrations of non-bridging oxygen hole center (NBOHC) defects and 3-membered rings. It is worth noting that the observed increase in the concentration of 3-membered rings is less for individual waveguides than for larger modified regions. This is probably a result of the Raman signal coming from a mixture of modified and unmodified material.

Additional spectra were collected from waveguides, larger modified lines, and Bragg gratings to observe the spatial extent of the femtosecond laser modification. The Raman results showed an increase in the concentration of 3-membered rings as measured by the ratio of the 605 / 800 cm^{-1} Raman peaks in the waveguides, but not in the larger modified lines or the Bragg gratings. It was further noted that the increase in this ratio was primarily the result of a decrease in the 800 cm^{-1} peak across the modified regions. The fluorescence results showed an increase in the defect concentration, measured by the total fluorescence signal, in all of the samples. The shape of the spatial fluorescence profiles closely matches the shape of the Gaussian focus used for writing the features. It was also determined that two types of fluorescent defects were present in the Bragg gratings: NBOHC defects with a peak around 650 nm, and $E_{\delta}^{'}$ defects with a peak around 540 nm. A review of earlier data revealed that $E_{\delta}^{'}$ defects were predominant in many waveguides

fabricated using low laser pulse energies, and NBOHC defects were predominant in waveguides fabricated using high laser pulse energies.

References

4.1 C. W. Smelser, S. J. Mihailov and D. Grobnic, "Formation of Type I-IR and Type II-IR gratings with an ultrafast IR laser and a phase mask," *Optics Express*, **13**(14), pp. 5377-5386, (2005).

4.2 W. Reichman, J. W. Chan and D. M. Krol, "Confocal fluorescence and Raman microscopy of femtosecond laser-modified fused silica," *Journal of Physics: Condensed Matter*, **15**, pp. S2447–S2456, (2003).

4.3 R. S. Taylor, C. Hnatovsky, E. Simova, D. Rayner, M. Mehandale, V. R. Bhardwaj and P. B. Corkum, "Ultra-high resolution index of refraction profiles of femtosecond laser modified silica structures," *Optics Express*, **11**(7), pp. 775–81, (2003).

4.4 C. B. Schaffer, A. Brodeur, J. F. Garcia and E. Mazur, "Micromachining bulk glass by use of femtosecond laser pulses with nonojoule energy," *Optics Letters*, **26**(2), pp. 93-95, (2001).

4.5 J. W. Chan, T. R. Huser, S. H. Risbud and D. M. Krol, "Modification of the fused silica glass network associated with waveguide fabrication using femtosecond laser pulses," *Applied Physics A*, **76**, pp. 367-372, (2003).

4.6 H. Nishikawa, E. Watanabe, D. Ito, Y. Sakurai, K. Nagasawa and Y. Ohki, "Visible photoluminescence from Si clusters in γ-irradiated amorphous SiO_2," *Journal of Applied Physics*, **80**, pp. 3513-3519, (1996).

4.7 S. Demos, M. Staggs, K. Minoshima and J. Fujimoto, "Characterization of laser induced damage sites in optical components," *Optics Express*, **10**, pp. 1444-1450, (2002).

Chapter 5

Understanding the Effects of the Pulse Repetition Rate.

5.1 Motivation

As discussed in Chapters 1 and 2.2.2, several groups recently have reported a large dependence of the localized modification on the laser pulse repetition rate (described in section 2.2.2). Traditionally, kilohertz repetition (rep) rate, amplified fs lasers have been used for fs device fabrication, but the recent development of high power oscillators and other high rep rate, fs sources has opened up the possibility of writing waveguides with repetition rates greater than 1 MHz. The principle differences reported when using high rep rate lasers are an increase in the perceived line diameter, and a potentially greater refractive index modification [5.1]. These differences are related to the fact that with high rep rate lasers there is insufficient time between pulses for the heat to diffuse out of the focal region and as a result heat accumulation occurs [5.2-5.3]. Additionally, it has been observed that megahertz systems provide better quality waveguides in some transparent glasses, while kilohertz systems are favored by other materials. Currently, it is unknown why some materials respond better with one laser or the other.

In order to better understand the differences in how kilohertz and megahertz repetition rate laser systems modify transparent materials, we used Raman and fluorescence

spectroscopy to compare fused silica modified with the 1 kHz, 10-250 kHz, and 1 MHz repetition rate femtosecond lasers discussed in chapter 3.

5.2 Experiment

Waveguides were fabricated in fused silica (Corning 7940) using the in house amplified, 1 kilohertz, Ti:Sapphire femtosecond laser, the amplified 10-250 kilohertz, Ti:Sapphire femtosecond laser at Harvard, and the 1 megahertz, frequency-doubled Yb-fiber laser at IMRA America, Inc.. Both of the kilohertz lasers operated at 800 nm with ~130 fs pulses, and 0 to 5 μJ pulse energies. The 1 kilohertz laser was focused into silica cubes using a 50X 0.55 NA objective, and the sample was moved longitudinally at 20 μm/s. The 10-250 kilohertz laser was focused into silica plates using a 20X 0.4 NA objective, and the sample was moved transversely at 4 to 400 μm/s. The megahertz laser was operated at 522 nm with ≤500fs pulses, using 90 and 115 nJ pulse energies. It was focused into silica plates using a 100X 0.85NA objective, and the sample was moved transversely at 0.05 to 5 mm/s. These conditions are summarized in Table 5.1.

Table 5.1 Repetition Rate Study Writing Conditions

Rep Rate	Wavelength	Pulse Energies	Scan Speed
1 kHz	800 nm	0.5 – 5 μJ	20 μm/s
10 kHz	800 nm	1 – 3.5 μJ	4 – 400 μm/s
50 kHz	800 nm	1 – 3.0 μJ	4 – 400 μm/s
250 kHz	800 nm	1 – 2.3 μJ	4 – 400 μm/s
1 MHz	522 nm	90 – 115 nJ	0.05 – 5 mm/s

The in-house scanning confocal microscope was used to simultaneously collect Raman and fluorescence spectra from all of the samples. A 50 mW, 488 nm Argon ion laser was focused into the sample using a 100X 0.73 NA microscope objective. The backscattered

Raman and back-emitted fluorescence were then collected using the same objective; and a 0.25 m spectrometer with a 300 groove mm^{-1} grating and a liquid nitrogen cooled CCD array detector, with a 5 minute acquisition time. Three spectra were collected from different points along the center of each waveguide. The spatial profiles of select waveguides were measured by scanning the sample with respect to the objective focus with a 1 μm step size traveling perpendicular to (across) the waveguides, and a 3 μm step size traveling along the waveguides. Fluorescence photobleaching was studied by continuously exposing stationary spots to the Ar^{+} laser for 14 hours while collecting spectra every half hour.

Finally, the emissions generated while writing lines with the 1 kHz laser were collected using the spectrometer and the 300 groove mm^{-1} grating. In this case a 750 nm short pass exit filter was used to eliminate extra light from the 800 nm femtosecond laser.

5.3 Results and discussion

White light microscope images were collected for the waveguides written with the MHz laser. Two examples (side view) are shown in Figure 5.1. For scan speeds below 2 mm/s smooth lines were observed, whereas scan speeds above 2 mm/s yielded macroscopically rougher lines, with micron scale variations. These micron scale variations are substantially larger than the pulse to pulse separation, and are similar to features observed by others with MHz writing [5.3].

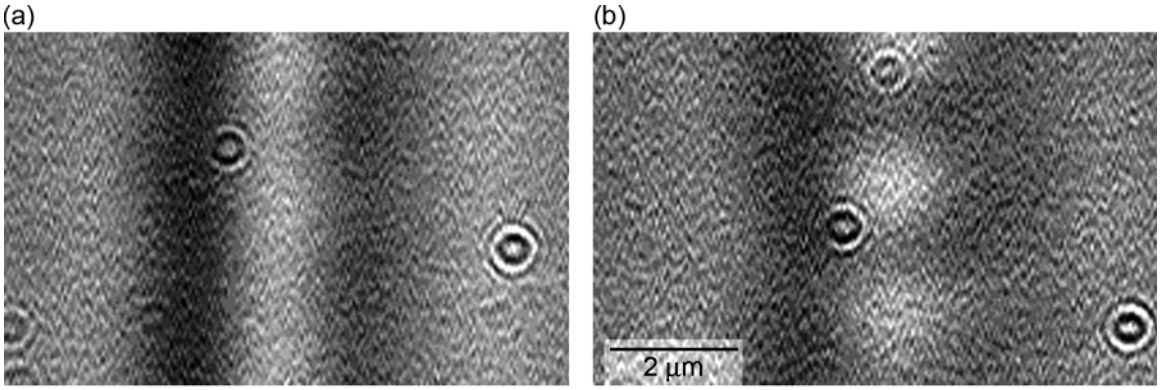

Figure 5.1 White light images of lines written with the MHz system using a pulse energy of 115 nJ, and scanning the sample transversely at a) 0.05 mm/s and b) 5 mm/s. The circular fringes are artifacts from the microscope.

All of the lines written with the MHz laser that were used in this study match those written with the highest cumulative dose in ref. 5.3, and exhibited good, low-loss, single-mode optically guiding with symmetric beam a profile. For lines written with the 1 kHz laser, such good waveguides were only obtained for laser pulse energies below 1 μJ. Lines written with the 1 kHz laser at pulse energies greater than 1 μJ showed substantial damage, and tended to scatter light [5.4-5.5]. The guiding behavior was not tested for the lines written with the 10-250 kHz laser.

Raman and fluorescence spectra were collected for each line written with the MHz laser, for each line written with the 10-250 kHz laser and from one high pulse energy (5 μJ) and one low pulse energy (0.5 μJ) line written using the 1 kHz laser. Figure 5.2 shows part of the Raman spectra of which the peaks at 605 cm^{-1} and 800 cm^{-1} are of particular interest. The areas of these Raman peaks were calculated using a straight line baseline from 570 to 645 cm^{-1} for the 605 cm^{-1} peak, and from 750 to 870 cm^{-1} for the 800 cm^{-1} peak. The ratio of the 605 cm^{-1} / 800 cm^{-1} peaks was then calculated as a measure of the relative intensity of the 605 cm^{-1} peak for the lines written with the 1 kHz and 1 MHz lasers.

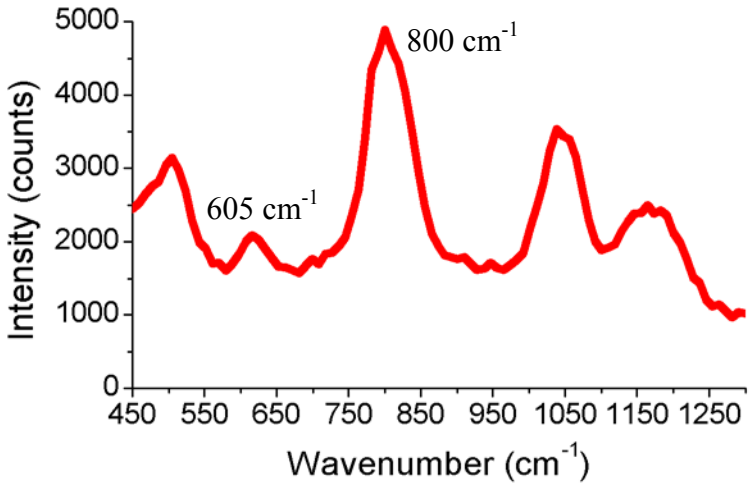

Figure 5.2 Raman spectrum of a waveguide written with the 1 MHz system using a pulse energy of 115nJ, and scanning the sample transversely at 0.5 mm/s.

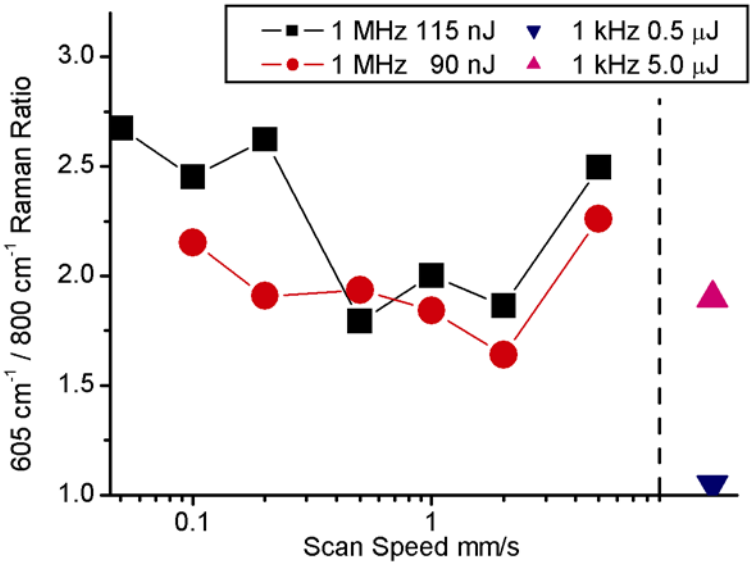

Figure 5.3 Normalized 605 cm^{-1} / 800 cm^{-1} Raman peak ratios for lines written using a 1 kHz rep rate laser system at a scan speed of 20 µm/s and a 1 MHz rep rate laser system at different scan speeds and pulse energies. The data is normalized with respect to the unmodified glass.

There was some contamination in the spectra for the lines written with the 10-250 kHz laser, such that area of the 605 cm^{-1} peak could not be calculated.

Figure 5.3 depicts the ratio of each line normalized to that of the unmodified glass. The increase in the 605 cm^{-1} / 800 cm^{-1} Raman peak ratio indicates an increase in the relative concentration of 3-membered rings [5.6-5.7]. The behavior is similar for lines written

using both the 1 MHz and the 1 kHz laser. However, the absolute magnitude of the change is twice as great for the MHz lines, as for the low pulse energy 1 kHz line. The concentration of 3-membered rings observed in the high pulse energy 1 kHz line is similar to the concentration observed in the MHz waveguides, but the 1 kHz waveguide shows significantly more light scattering and does not exhibit good waveguiding. Since a greater concentration of 3-membered rings is associated with an increased local refractive index [5.4-5.7] our results support the contention that in fused silica high rep rate modification yields good quality waveguides with a greater refractive index increase than low rep rate modification. It is also worth noting that for the MHz lines the concentration of 3-membered rings is not dependence on scan speed or pulse energy. In contrast for lines written with the kHz laser, the concentration of 3-membered rings has a strong dependence on pulse energy.

Both of the fluorescence peaks identified in chapter 4 were observed in different samples. The low pulse energy 1 kHz line has a fluorescence peak near 540 nm, which is attributed to the presence of self trapped exciton ($E_{\delta}^{'}$) defects from very small silicon nano-clusters that several groups have reported seeing in γ-irradiated fused silica [5.8-5.9]. In contrast, all of the 1 MHz waveguides exhibit a broad, low intensity fluorescence band centered around 650 nm from non-bridging oxygen hole center (NBOHC) defect [5.4-5.5]. Sample spectra for each type of fluorescence are shown in figure 5.4, however several lines also showed both types of fluorescence. The area under the, fluorescence curve from 555 to 800 nm was calculated using a zero intensity baseline as a measure of the total fluorescence intensity for each of the modified lines and for the unmodified glass.

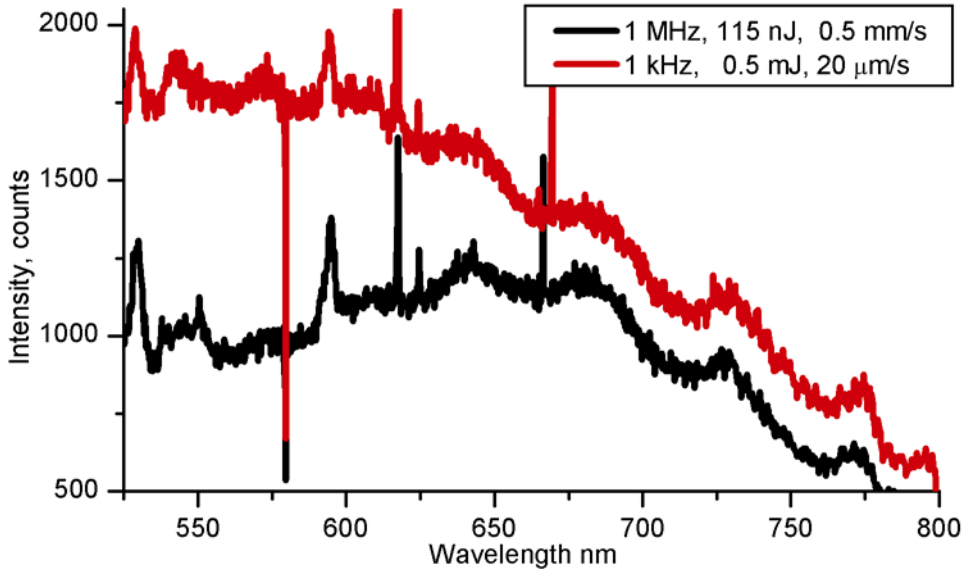

Figure 5.4 Fluorescence spectra of waveguides written with the 1 kHz laser system using a laser pulse energy of 0.5 μJ, and scanning the sample longitudinally at 20 μm/s, and the 1 MHz system using a pulse energy of 115nJ, and scanning the sample transversely at 0.5 mm/s.

Figure 5.5 depicts the fluorescence peak area of each line, divided by the peak area of the unmodified glass. All of the lines written with the 1 MHz laser have substantially more fluorescence (~5x) than the unmodified material. However, the fluorescence intensities for lines written the 1 kHz laser system are 2 to 3 orders of magnitude higher than those for the MHz laser system. Lines written with the 10-250 kHz laser system have intermediate intensities, as indicated by the different intensity scales used in figure 5.5.

To understand the different material responses associated with different writing conditions it is important to determine which writing parameters (e.g. pulse fluence, peak intensity, total exposure) control defect formation and structural changes. For a constant pulse energy and pulse repetition rate, increasing the scan speed leads to less fluorescence, though this trend decreases with increasing pulse repetition rate and

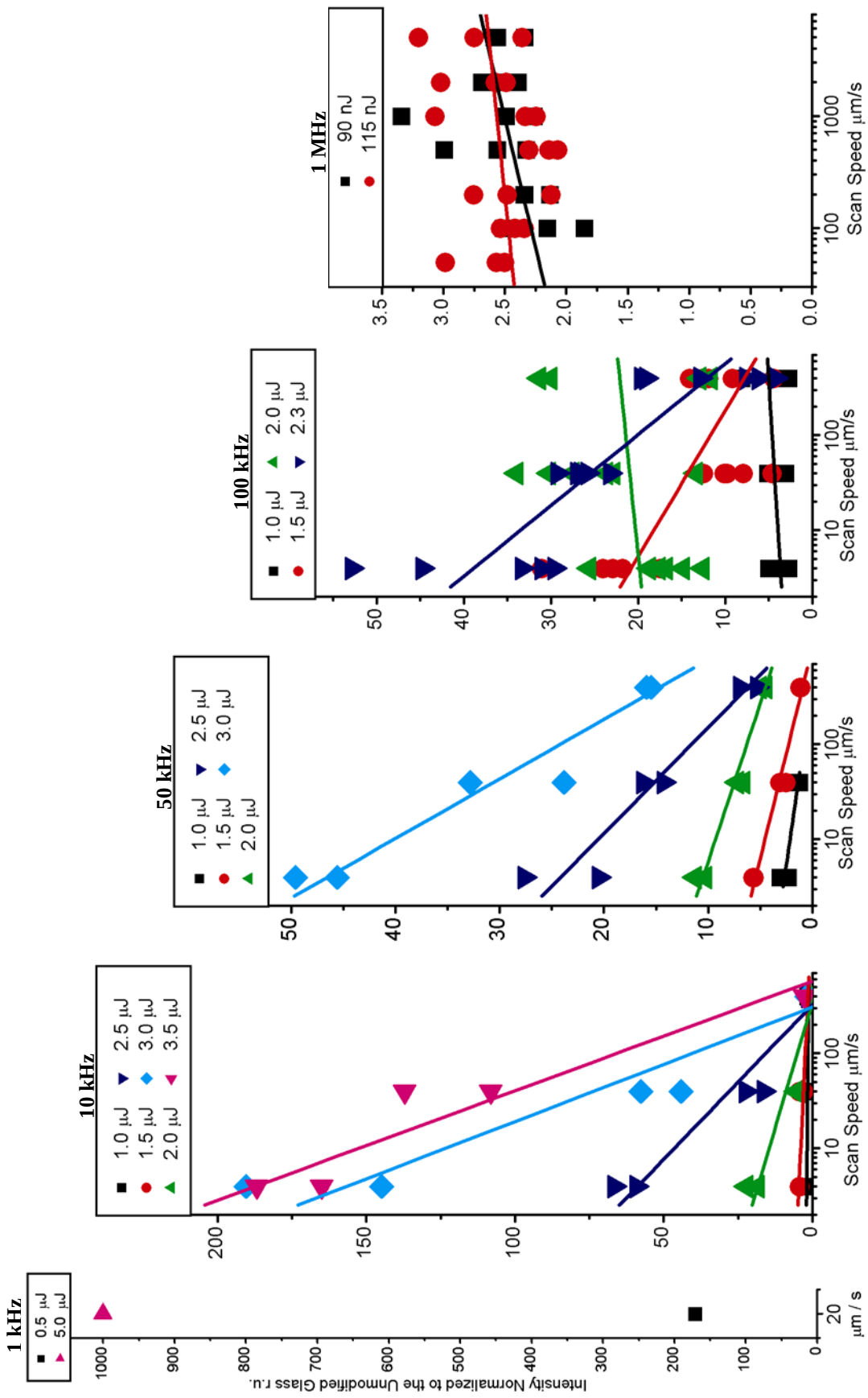

Figure 5.5 Fluorescence intensities for lines written at different rep rates (graphs), scan speeds (x axes), and pulse energies (see legends).

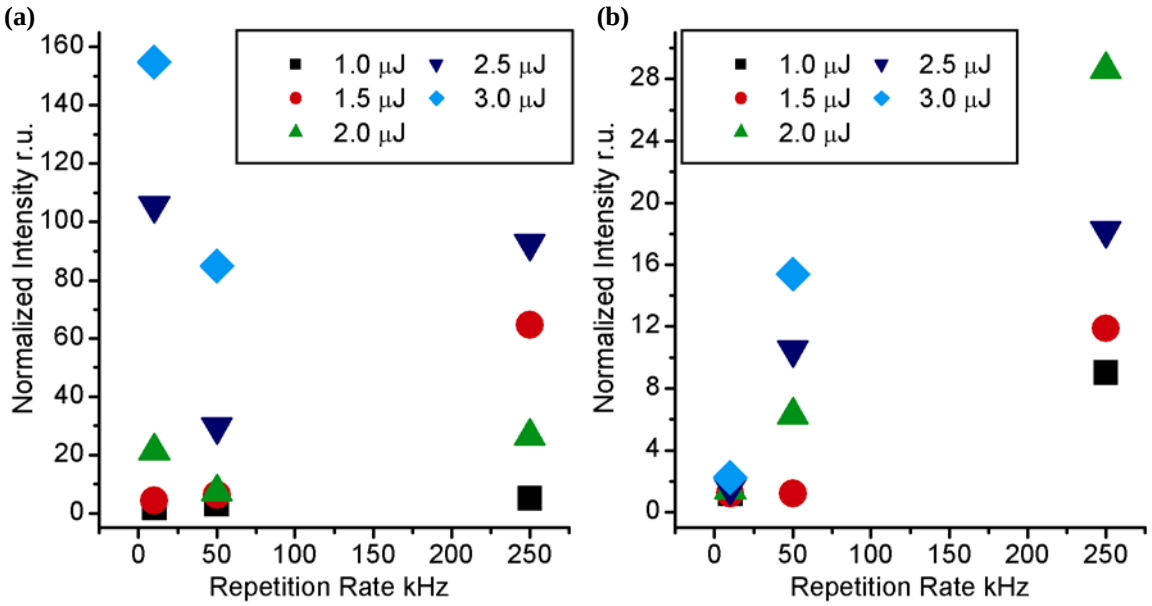

Figure 5.6 Fluorescence intensities for lines written with scan speeds of (a) 4 mm/s and (b) 400 mm/s. Note, the points plotted as being written with 2.5 µJ and 250 kHz were actually written using 2.3 µJ and 250 kHz.

decreasing pulse energy. It is difficult to determine whether the massive decrease in fluorescence with increasing repetition rate shown in figure 5.5 is a result of increasing the repetition rate or a result of decreasing the pulse energy, because the lasers with the highest repetition rates also have the lowest pulse energies. Figure 5.6 shows that increasing the repetition rate causes a decrease in the fluorescence for lines written with slow scan speeds and high pulse energies, and that it causes an increase in the fluorescence intensity for lines written with higher scan speeds. In an attempt to resolve this inconsistency, the fluorescence and Raman results for several extreme writing conditions are analyzed in terms of a larger variety of laser parameters, in Table 5.2. The data in the Table shows that neither the fluorescence nor the Raman signal scales linearly with pulse fluence, peak intensity, or total dose. As expected, increasing the peak intensity causes a greater material change leading to more defects and greater fluorescence.

Table 5.2. Comparison of laser modification with MHz and KHz lasers.

Writing conditions							**Spectroscopy**	
Pulse energy E (μJ)	Spot size[1)] A (μm^2)	Rep rate r (s^{-1})	Scan speed v (mm/s)	**Pulse fluence F (J/cm^2)**	**Peak intensity[2)] I (TW/cm^2)**	**Total dose[3)], D (MJ/cm^3)**	**Fluor. signal (a.u)**	**Raman signal (a.u)**
0.115	0.27	10^6	0.05	**43**	**85**	**8500**	**5.4**	**2.7**
0.115	0.27	10^6	5	**43**	**85**	**85**	**6.5**	**2.5**
0.5	1.51	10^3	0.02	**33**	**250**	**16**	**170**	**1.1**
5.0	1.51	10^3	0.02	**330**	**2500**	**160**	**1000**	**1.9**

[1)] The spot size A was calculated as $A= \pi w_0^2$; w_o (the spot radius) = $M^2\lambda/(\pi NA)$, where $M^2 = 1.5$ is the beam quality factor, λ is the laser wavelength, and NA is the numerical aperture of the focusing objective.
[2)] The pulse intensity was calculated as $I = F/\tau$; for the kHz laser the pulse duration, τ, is 130 fs. For the MHz laser the pulse duration is less accurately known, an upper limit of 500 fs was used in our calculations.
[3)] For the case of longitudinal writing (with the kHz laser) the total dose, D = Fr/v; for the case of transverse writing (with the MHz laser) D = Fr(NA)/v.

A second interesting trend in figures 5.3 and 5.5 is that the total fluorescence and Raman intensities become less dose dependent with increasing rep rates. Surprisingly, in the cases of the 1 MHz and the 1 μJ, 250 kHz lines increasing the total exposure (slower scan speeds) actually leads to slightly less fluorescence, indicating fewer defects. We believe that the decrease in the fluorescence with increasing exposure in the high rep rate cases is the result of thermal accumulation partially annealing the modified region while writing. The low thermal conduction in glasses prevents the absorbed laser energy from diffusing out of the focal region during the interval between pulses while writing with high rep rate lasers. Other groups have reported large diameter modified regions forming in other glasses as another result of thermal accumulation [5.2-5.3].

Additional fluorescence and Raman scans were performed across several of the waveguides written with the MHz laser to provide information on the spatial extent of the structural changes. These measurements were designed to test if the diameter of the

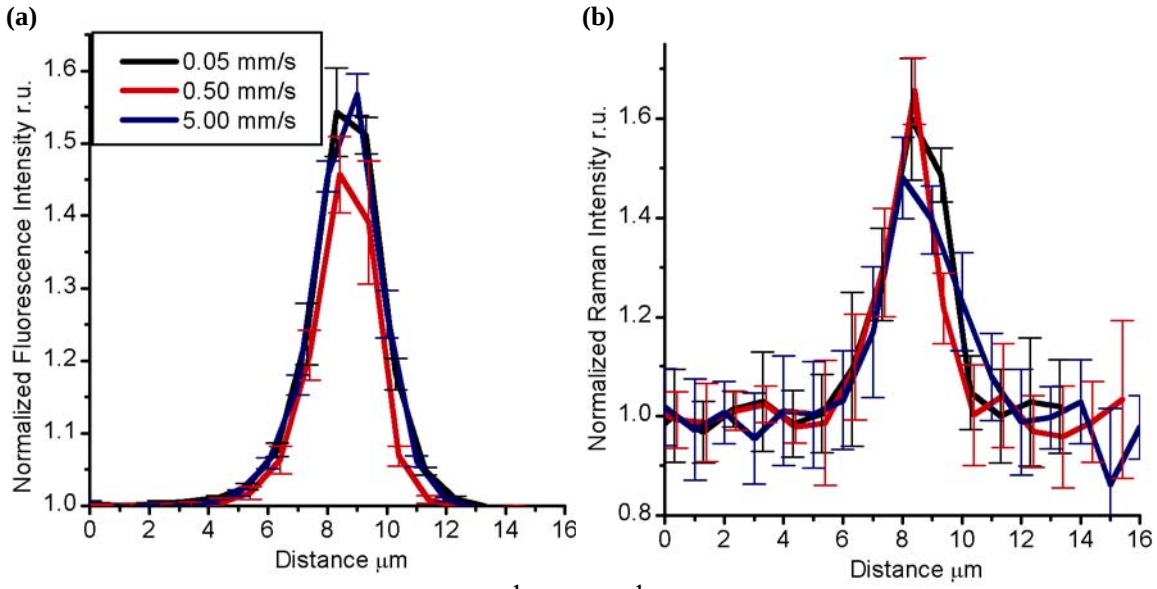

Figure 5.7 a) Fluorescence, and b) 605 cm^{-1} / 800 cm^{-1} Raman peak ratio intensity cross-sections for waveguides written with a 1 MHz laser and 115nJ pulse energy. Both plots are normalized to the data for unmodified glass.

waveguides increased as a result of greater thermal accumulation with increasing dose (slower scan speeds). The graphs presented in figure 5.7 are the result of averaging 6 scans for each line. The data in figure 5.7 is normalized to the signal from the unmodified glass. Both fluorescence and Raman spatial profiles have a FWHM of about 2.0 ± 0.5 microns. This is in good agreement with the line-width obtained from the white light micrographs in figure 5.1. However, an increase in diameter was not observed with increasing total dose in our sample, for the range of processing conditions studied [5.10]. This indicates that there is not sufficient thermal accumulation to modify the material beyond the focal volume.

Finally, it is worth taking a closer look at the two different types of fluorescent defects that were shown in figure 5.4. All of the lines created using 1 MHz and 250 kHz exhibit NBOHC defects. For a 50 kHz laser repetition rate, lines created using pulse energies less than 1.5 μJ and a scan speed of 400 μm / s have $E_{\delta}^{'}$ defects, while the lines created

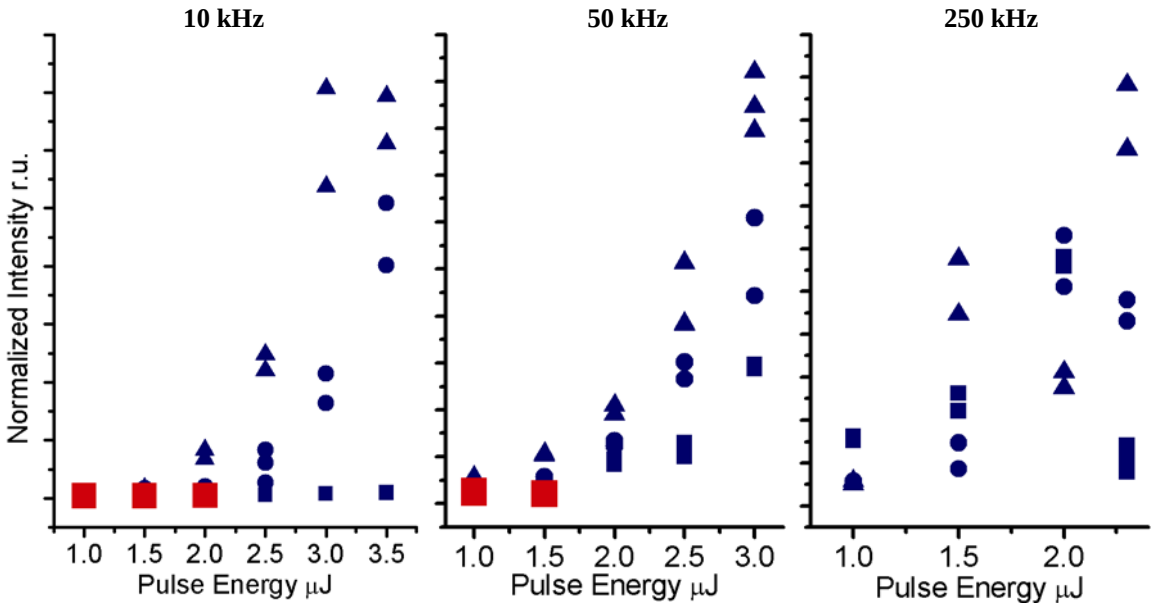

Figure 5.8 Two types of fluorescent defects were observed for different writing conditions. Several of the graphs from figure 5.5 have been rearranged to emphasize the effects of changing the pulse energy on the resulting defect types. Points at which the fluorescence is dominated by NBOHC defects are in blue, points where it is dominated by E'$_\delta$ defects are in red. The different shapes indicate the scan speed: 4 μm / s for triangles, 40 μm / s for circles, and 400 μm / s for squares.

with greater doses have NBOHC defects, as shown in figure 5.8. For a 10 kHz repetition rate the threshold is increased to 2 μJ, at 400 μm/s. And for a 1 kHz repetition rate it increases to 1 μJ at 20 μm/s.

Fluorescence photobleaching studies were performed for waveguides formed by various laser writing conditions by using a low power (30 mW) Ar^+ laser to probe the fluorescence from fs-laser induced defects. During exposure to the low power Ar^+ beam the fluorescence intensity continuously decreased, as previously observed for lines written with the 1 kHz laser system [5.5]. The photobleaching results are shown in figure 5.9. Each graph shows the spectrum of the unmodified glass, the spectrum of the waveguide region and the spectrum of the same waveguide region after prolonged exposure to the low power Ar^+ laser. Figure 5.9a shows that that the fluorescence

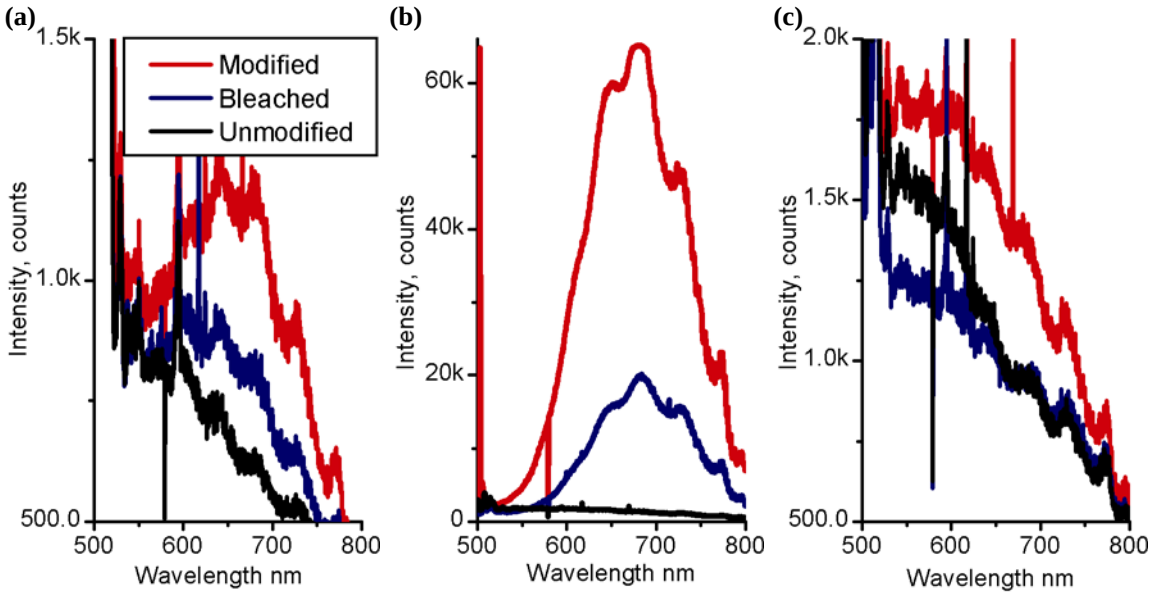

Figure 5.9 Fluorescence of fs-laser modified lines after 14 hours of exposure to 30 mW of Ar^+ laser light.. The intial fs laser modification conditions were a) 1 MHz repetition rate, 115nJ pulse energy, 0.5 mm/s scan speed b) 1 kHz, 5 μJ, 20 μm/s c) 1 kHz, 0.5 μJ, 20 μm/s. All spectra were recorded with a 5 minute acquisition time.

decreases by about two-thirds after 14 hours for the 115 nJ, 0.5 mm/s MHz waveguide. This is typical for all of the lines written with the MHz rep rate, and for all of the kHz rep rate lines, which had NBOHC defects (figure 5.9b). This indicates that the local environment around the defects is independent of the rep rate, however, the kHz lines had a far greater initial intensity indicating more defects were formed. The low pulse energy E_δ' containing 1 kHz line (figure 5.9c) bleached completely within 14 hours of Ar^+ laser exposure, even though the initial fluorescence intensity was similar to that from waveguides formed by the MHz laser.

The absence of E_δ' defects in both higher dose kHz damage lines and MHz waveguides can again be accounted for by photobleaching while writing. Alternatively, for the high pulse energy kHz lines there is so much fluorescence from the NBOHC defects that it may overshadow the fluorescence from E_δ' centers. Since these defects form at lower

pulse energies than the NBOHC defects, the $E_{\delta}^{'}$ centers have a lower energy barrier for formation as well as for bleaching.

The waveguides written with all of the laser systems appear to retain good guiding behavior after Ar^{+} laser photobleaching of the NBOHC or $E_{\delta}^{'}$ defects. This indicates that the fluorescent defects are not responsible for the refractive index changes that result in guiding behavior. This contention is further supported by the earlier observation that the waveguides written with the 1 MHz system appear to have a greater refractive index change based on the 3-membered ring concentration, despite having less fluorescence than the waveguides written with the kHz systems.

In order to gain further insight into the physical processes associated with the modification process, we measured the light emitted from the sample while fabricating waveguides. The emissions were collected while writing lines with the 1 kHz repetition rate laser. For low pulse energies there is a narrow "blue" emission centered around 475 nm that is shown in figure 5.10a. At higher pulse energies there is a stronger "white" emission with a maximum around 540 nm, shown in figure 5.10b. Comparing the emission spectra in figure 5.10c, it is clear that the spectrum shown in figure 5.10b is a superposition of the "blue" emission band shown in fig 5.10a and a second band centered at 540 nm. The relative intensity of the 540 nm band increases with increasing femtosecond pulse energy, as shown in fig. 5.10c. The pulse fluence above which the "white" 540 nm emission is observed is approximately 42 J cm^{-2}. This is around the same fluence at which the transition between the two fluorescent defect types occurs, as

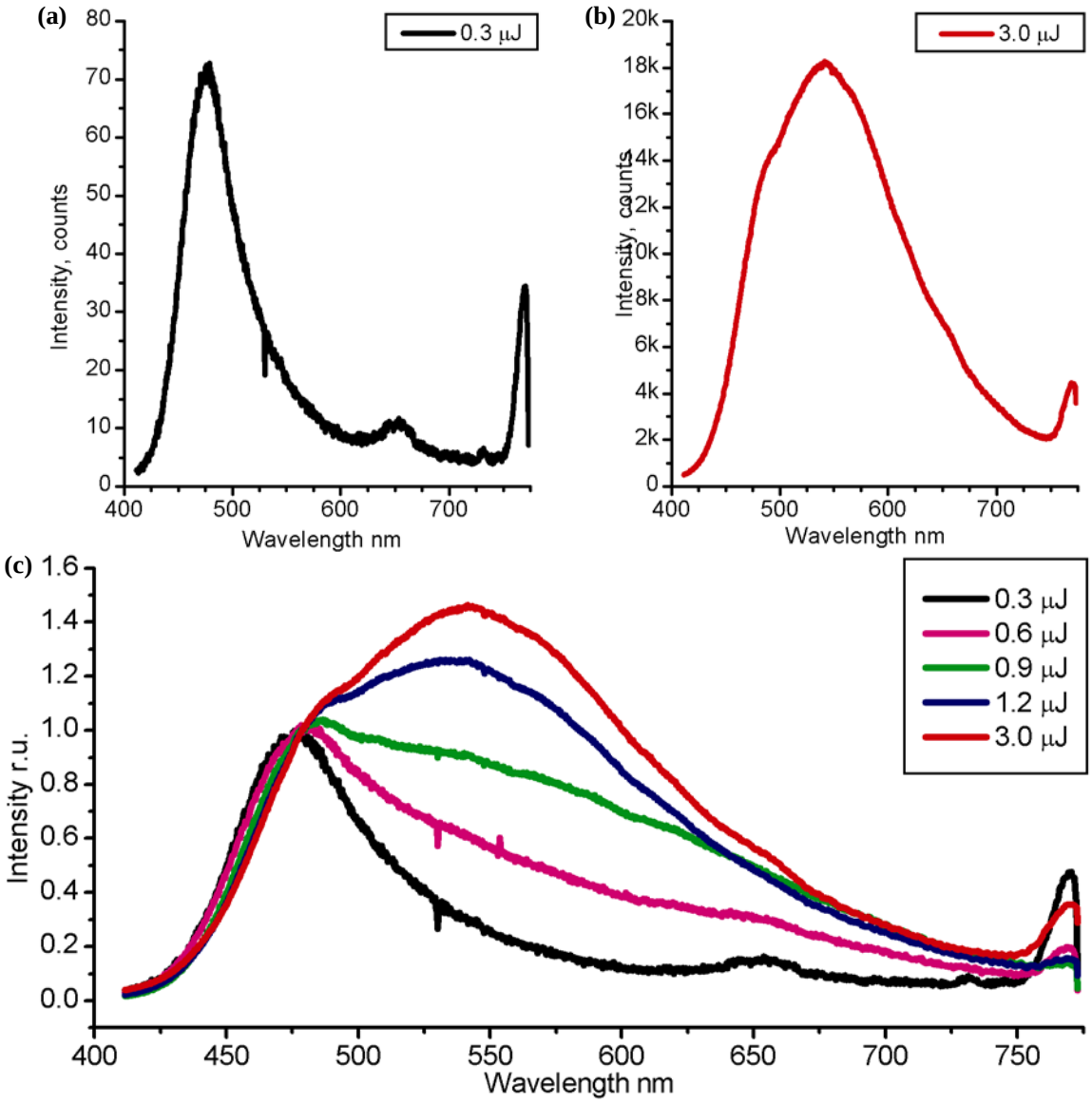

Figure 5.10 Emission spectra collected while writing lines with the 1 kHz laser, a 20X microscope objective, and a) 0.3 μJ to b) 3.0 μJ. All of the lines in c) are normalized to their intensity at 475 nm to accentuate changes in the shape of the emission spectra.

well as the transition between controlled modification (which produces good waveguides) and uncontrolled damage when writing with the 1 kHz repetition rate laser.

These observations suggest that there are two modification regimes that correspond to different pulse fluences, at least when writing with the 1 kHz laser. The first is a low pulse fluence regime, which is characterized by "blue" emissions while writing, the

presence of $E_{\delta}^{'}$ defects after writing, and the formation of good waveguides. The second is a high pulse fluence regime, which is characterized by "white" emissions while writing, the presence of NBOHC defects after writing, and the formation of damaged lines. The origin of the emission bands at 475 and 540 nm is uncertain. Another group, Carr et al., has measured the emission generated during femtosecond laser exposure under slightly different conditions. They suggested three potential emission mechanisms to explain their results: nonlinear second-harmonic generation, super-continuum generation, and plasma emissions [5.11]. The emission bands that they observed had different peak positions than those seen in our results, which indicate that our emissions may result from a slightly different processes. We tentatively assign the 475 nm band to nonlinear frequency-mixing, based on the fact that it is observed for all pulse fluences. The band at 540 nm is only observed at higher pulse energies where other experiments have shown plasma forms [5.12], thus we believe that it relates to plasma emission.

We have not been able to collect emission spectra while writing with higher repetition rates. Visual observations of the sample during high repetition rate writing show a "blue" emission at low pulse energy writing conditions that are barely capable of modifying the material, and a "white" emission when using higher pulse energies.

5.4 Summary

Our results show that fluorescent defects are formed during the femtosecond laser modification process when using lasers with repetition rates ranging from 1 kHz to

1 MHz. Higher repetition rates favor the formation of NBOHC defects over $E_{\delta}^{'}$ defects, with only NBOHC defects being present for all lines fabricated with the 250 kHz and 1 MHz laser systems. Far fewer defects were formed with the 1 MHz laser than with the higher pulse energy kHz lasers. This is probably a result of the higher rep rate system having lower pulse energies, though it is also possible that the defects are bleached during high rep rate fabrication. We also observed an increase in the relative intensity of the 605 cm^{-1} Raman peak, corresponding to an increase in the concentration of 3-membered rings. The lines fabricated with the MHz laser system had a substantially larger increase than the line low pulse energy 1 kHz lines, indicating that the MHz laser system may cause a greater increase in the refractive index. Finally, both the fluorescence and Raman signals become less dose dependent at higher rep rates.

References

5.1 L. Shah, A. Y. Arai, S. M. Eaton, and P. R. Herman, "Waveguide writing in fused silica with a femtosecond fiber laser at 522 nm and 1 MHz repetition rate," *Optics Express*, **13**(6) 1999-2006, (2005).

5.2 C. B. Schaffer, A. Brodeur, J. F. Garcia and E. Mazur, "Micromachining bulk glass by use of femtosecond laser pulses with nonojoule energy," *Optics Letters*, **26**(2), pp. 93-95, (2001).

5.3 R. Osellame, N. Chiodo, V. Maselli, A. Yin, M. Zavelani-Rossi, G. Cerullo, P. Laporta, L. Aiello, S. De Nicola, P. Ferraro, A. Finizo and G. Pierattini, "Optical properties of waveguides written by a 26 MHz stretched cavity Ti:sapphire femtosecond oscillator," *Optics Express*, **13**(2), pp. 612-620, (2005).

5.4 J. W. Chan, T. R. Huser, S. H. Risbud and D. M. Krol, "Structural changes in fused silica after exposure to focused femtosecond laser pulses," *Optics Letters*, **26**(21), pp. 1726-1728, (2001).

5.5 J. W. Chan, T. R. Huser, S. H. Risbud and D. M. Krol, "Waveguide fabrication in phosphate glasses using femtosecond laser pulses," *Applied Physics Letters,* **82**(15)**,** pp. 2371-2373, (2003).

5.6 A. E. Geissberger and F. L. Galeener, "Raman studies of vitreous SiO_2 versus fictive temperature" *Physical Review B*, **28**(6), pp. 3266–3271, (1983).

5.7 A. Pasquarello and R. Car, "Identification of Raman defect lines as signatures of ring structures in vitreous silica," *Physical Review Letters*, **80**(23), pp. 5145–5147, (1998).

5.8 H. Nishikawa, E. Watanabe, D. Ito, Y. Sakurai, K. Nagasawa and Y. Ohki, "Visible photoluminescence from Si clusters in γ-irradiated amorphous SiO_2," *Journal of Applied Physics*, **80**, pp. 3513-3519, (1996).

5.9 S. Demos, M. Staggs, K. Minoshima and J. Fujimoto, "Characterization of laser induced damage sites in optical components," *Optics Express*, **10**, pp. 1444-1450, (2002).

5.10 S. M. Eaton, H. Zhang, P. R. Herman, F. Yoshino, L. Shah, J. Bovatsek and A. Y. Arai, "Heat accumulation effects in femtosecond laser-written waveguides with variable repetition rate," *Optics Express*, **13**(12), pp. 4708-4716, (2005).

5.11 C. W. Carr, M. D. Feit, A. M. Rubenchik, P. De Mange, S. O. Kucheyev, M. D. Shirk, H. B. Radousky, and S. G. Demos, "Radiation produced by femtosecond laser–plasma interaction during dielectric breakdown," *Optics Letters*, **30**(6), pp. 661-663, (2005).

5.12 D. Du, X. Liu, G. Korn, J. Squier and G. Mourou, "Laser-induced breakdown by impact ionization in SiO_2 with pulse widths from 7 ns to 150 fs," *Applied Physics Letters,* **64**(23), pp. 3071–3073, (1994).

Chapter 6

Understanding the Effects of the Material Composition.

6.1 Motivation

Waveguide fabrication using femtosecond laser pulses has been most thoroughly studied in fused silica. Many devices including waveguides and various other optical devices have been fabricated in this material. However fused silica is a poor material choice for producing active devices including lasers and amplifiers. The reason for this is that active devices typically require the use of glasses doped with rare-earth ions and in fused silica such doping is limited to very low concentrations. To expand the versatility of femtosecond waveguide fabrication to other glass compositions it is necessary to know how the composition affects the modification process. Preliminary studies of producing waveguides in different glasses, discussed in section 2.3.4.3, show that two types of guiding behavior can result from the modification process [6.1]. Our group proposed that the different guiding behaviors could be explained by differences in how the different materials behave when they are rapidly cooled or quenched, as discussed in section 2.3.4.4. However, the glasses used in the preliminary studies, fused silica and Schott IOG-1 (a phosphate glass), have different chemical, optical, and physical properties. To test the validity of the model proposed by our group, referred to as the rapid quenching model, it is desirable to study the femtosecond-laser writing behavior in a glass system where the composition can be systematically varied.

To this end, we have examined the waveguiding behavior of soda lime silicate glasses in the xNa_2O $xCaO$ $(1-2x)SiO_2$ series. It is known that rapid quenching of glasses with high alkali content will result in a lower refractive index [6.2], similar to IOG. By observing the type of waveguides produced and comparing this to the relationship between cooling rate and refractive index at various values of x, it should be possible to determine if the rapid quenching model is valid. In addition, we will use spectroscopy to examine the local microstructure changes that occur within the glasses.

6.2 Experiment

The three glasses studied were Corning 7940 type III silica glass (fused silica), Schott Company Glass 6 ($15Na_2O$ $15CaO$ $70SiO_2$), and Schott Company Glass 4-2 ($20Na_2O$ $20CaO$ $60SiO_2$). The in-house amplified Ti-sapphire laser operating at 800 nm with a 130 fs pulse width, and a 1kHz repetition rate was focused through a Nikon 20X 0.4 NA ELWD objective using pulse energies from 0.15 to 20 μJ after the objective. The sample was moved at 20 $\mu m\ s^{-1}$, parallel to the laser beam (longitudinally) to create the modified lines. Care was taken to ensure that the focal spot never reached the sample surface.

After fabricating the waveguides the 488 nm Argon ion laser, set to low power (5 mW), was coupled into the resulting waveguides by adjusting either the 5-axis stage the sample was mounted on (item 12 in chapter 3), or the 3-axis stage supporting the 1^{st} microscope objective (item 13b in chapter 3). The far field image was observed on a screen 70” from

the sample, and the near field image was collected using a 2nd microscope objective and a CCD camera. Spectroscopy was performed by increasing the power of the Ar^+ laser to 50 mW, and collecting the back scattered / emitted light using the integrated confocal microscope; a 488 nm long-pass filter was used to eliminate the excitation laser. Either a PMT or a 0.25m spectrometer with a 300 groove per mm, 500 nm blaze grating were used to collect the light. The PMT was used to rapidly measure the total scattering and emission from the sample as a function of spatial position with an acquisition time of 0.1 s per point. The spectrometer was used to measure changes in the fluorescence spectra as a function of spatial position with an acquisition time of 5 min per point.

6.3 Results and discussion

Figure 6.1 shows the white light images of waveguides in both of the soda lime silicate glasses. The waveguide behavior is similar to the behavior of IOG-1. There is a non-guiding central region that appears black, bounded by guiding peripheral regions that appear white in the white light images. This pattern is observed for all lines that exhibit guiding behavior. It was found that a wide range of laser pulse energies produced such waveguides in both soda lime silicate samples. Lines created with 5 to 10 μJ pulse energies had regions with good guiding behavior. Lines created with more power exhibit a larger black damaged central region, without the white guiding peripheral regions. Lines created with less power had a smaller, grey (not black) damaged central region that faded to invisibility with pulse energies less than 0.25 μJ, without the white guiding peripheral regions. Guiding was not observed within the central, exposed region for lines

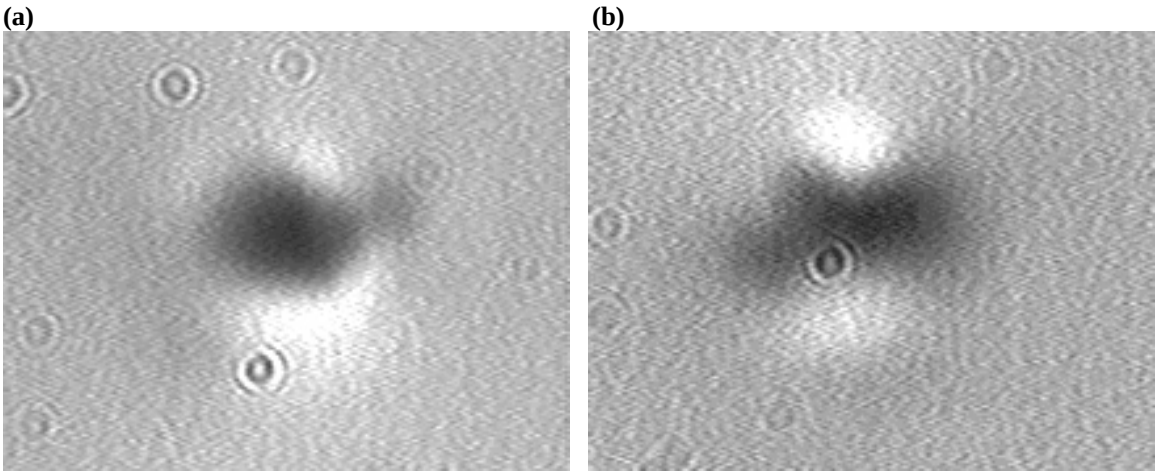

Figure 6.1 a) White light images of the endfaces of a 9.3 μJ line in $15Na_2O$ 15Ca2O $70SiO_2$, and b) $20Na_2O$ 20CaO $60SiO_2$

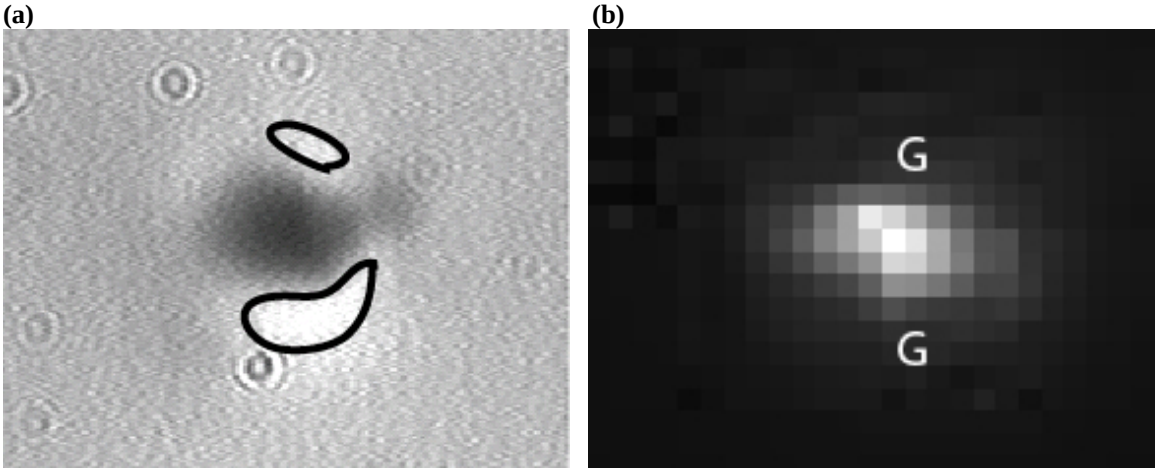

Figure 6.2 a) White light image and b) fluorescence image of the endface of a 9.3 μJ line in $15Na_2O$ 15Ca2O $70SiO_2$. The black circles in the white light image, and the "G"s in the fluorescence image denote where waveguide coupling was achieved.

written with any pulse energy. This is different from fused silica in which the lowest power lines that are visible exhibit guiding within the exposed region.

Figures 6.2a and 6.2b show a white light image and cross-section image of the total emission intensity of the same waveguide shown in figure 6.1a under identical magnification. Each pixel in the fluorescence image is 0.5 μm. By comparing this image with the coordinates where waveguide coupling is possible we can determine that guiding

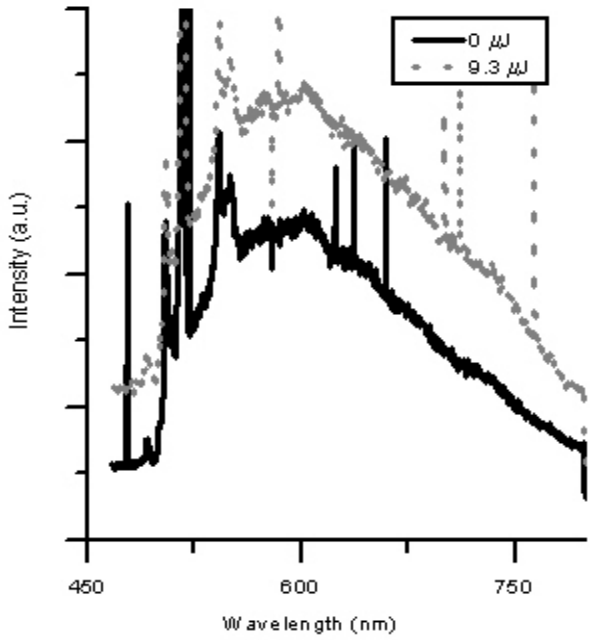

Figure 6.3 Fluorescence spectra of a 9.3 μJ line, and unmodified glass in $15Na_2O$ 15Ca2O $70SiO_2$.

takes place in regions (marked with "G") on either side of the exposed central region, from which the fluorescence is observed. Spectroscopy was used to determine the nature of the modified region's emission. Spectra of the center of the exposed region and of unmodified glass are shown in figure 6.3. An increase in the broad fluorescence centered around 610 nm is observed for the modified region. This fluorescence band is due to NBOHC defects that are formed in the region exposed to the fs laser. The contrast between modified and unmodified regions is less pronounced in the fluorescence spectra (figure 6.3) than in the fluorescence image (figure 6.2b) because of photobleaching that occurs during the longer acquisition time used to collect the spectra. Similar photobleaching of NBOHC defects has been observed in fused silica [6.3].

Near field images were collected for each guiding region to evaluate the waveguide quality. Figure 6.4 shows that for the $15Na_2O$ 15CaO $70SiO_2$ sample, there is very nice,

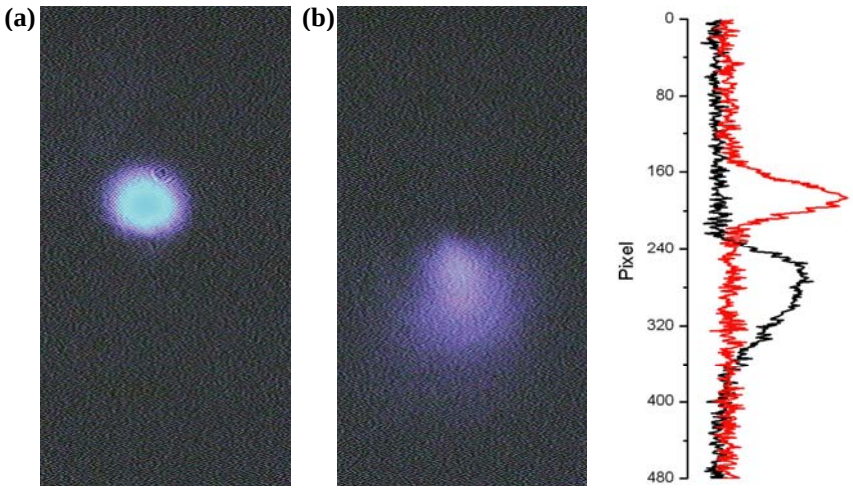

Figure 6.4 Near field profiles of 9.3 μJ waveguides a) above the modified region, and b) below the modified region in 15Na_2O 15CaO 70SiO_2 glass and the intensity distribution.

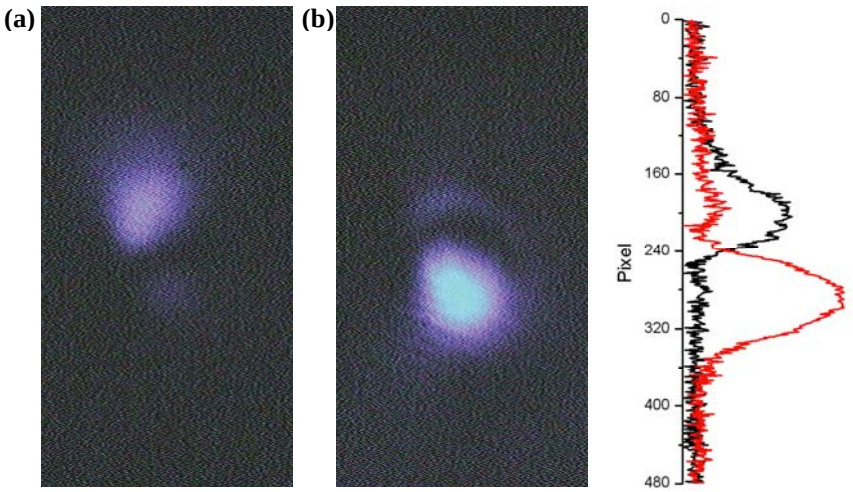

Figure 6.5 Near field profiles of 9.3 μJ waveguides a) above the modified region, and b) below the modified region in 20Na_2O 20CaO 60SiO_2 glass and the intensity distribution.

almost circular, guiding behavior in the upper waveguide. The lower waveguide is far more diffuse and elongated to one side. The 20Na_2O 20CaO 60SiO_2 sample (figure 6.5) shows the opposite behavior with better confinement in the lower waveguide than in the upper, with both profiles being slightly elongated. This difference is a result of minor positioning adjustments of the writing beam passing through the objective. Note, for comparing figures 6.2 and 6.4 it is necessary to invert the images because of the second microscope objective used to collect the near field profiles.

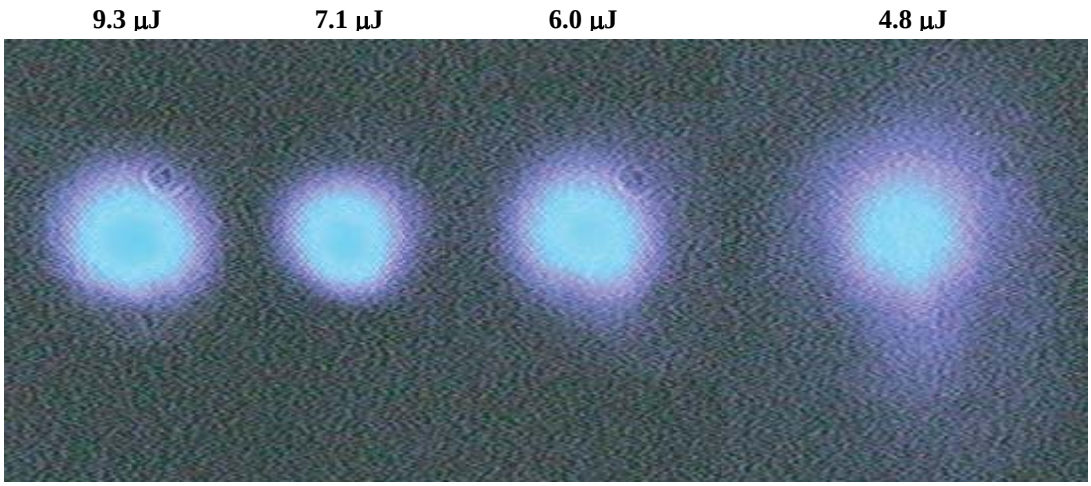

Figure 6.6 Composite image of the near field profiles of "top" waveguides in $15Na_2O$ $15CaO$ $70SiO_2$ glass.

The near field profiles are arranged as a function of writing energy in figure 6.6. Pulse energies greater than 10 μJ gave rise to excessive scattering resulting in no well-defined waveguides. Some guiding was evident at lower powers between 1.5 and 5 μJ, however, the spot size rapidly increased indicating poor beam confinement. It is our belief that while some modification clearly occurred, the refractive index change induced is not sufficient to produce good quality waveguides.

The far-field profiles were used to calculate approximate values for the refractive index by calculating the NA of the spreading cone, and comparing this value to the theoretical NA for total internal reflection of a step index change, using equations 6.1 and 6.2 respectively,

$$NA \sim \tan(\theta) = \frac{d}{2z} \qquad \text{Eq 6.1}$$

$$NA = \sqrt{2n_o \Delta n} \qquad \text{Eq 6.2}$$

where d is the far-field waveguide diameter, z is the distance over which the far-field profiles were measured (70”), n_o is the refractive index of the unmodified glass, and Δn is the change in the refractive index. Equation 1 assumes $d << 2z$, and equation 2 assumes $\Delta n << n_o$.

All of the waveguides had Δn values within a factor of 4 of 10^{-4}. No significant trends were observed between the refractive index change and the writing power, though this may be due to large errors in the far-field measurements.

Taken together these results clearly show that waveguides written in soda lime silicate glasses ($15Na_2O$ $15CaO$ $70SiO_2$ and $20Na_2O$ $20CaO$ $60SiO_2$) guide around the modified region. This is similar to the behavior observed in IOG-1, and supports the rapid quenching model of waveguide formation because both the soda lime silicate glasses and IOG-1 have a lower bulk refractive index with increased quenching rate. High-resolution refractive index profiles of femtosecond laser fabricated lines in various glasses provide additional support for the rapid quenching model [6.4].

6.4 Summary

Waveguides were fabricated in soda lime silicate glasses with compositions of xNa_2O $xCaO$ $(1-2x)SiO_2$ where x = 15, and 20. The resulting waveguides exhibit the same behavior our group first observed in IOG-1 glass; the waveguides are around but not

within a central modified line. This result has been confirmed using white light imaging, fluorescence imaging, and by measuring the near field profiles of the waveguides. Both the soda lime silicate glasses, and IOG-1 have a lower bulk refractive index with increased quenching rate, supporting the fast quenching model for femtosecond laser waveguide fabrication.

References

6.1 J. W. Chan, T. R. Huser, S. H. Risbud and D. M. Krol, "Waveguide fabrication in phosphate glasses using femtosecond laser pulses," *Applied Physics Letters,* **82**(15)**,** pp. 2371-2373, (2003).

6.2 H. Scholze, Glass: Nature, Structure, and Properties, New York State College of Ceramics, Alfred, NY, pp 211, 1991.

6.3 J. W. Chan, T. R. Huser, S. H. Risbud and D. M. Krol, "Modification of the fused silica glass network associated with waveguide fabrication using femtosecond laser pulses," *Applied Physics A,* **76**, pp. 367-372, (2003).

6.4 V. R. Bhardwaj, E. Simova, P. B. Corkum, D. M. Rayner, C. Hnatovsky, R. S. Taylor, B. Schreder, M. Kluge, and J. Zimmer, "Femtosecond laser-induced refractive index modification in multicomponent glasses," *Journal of Applied Physics*, **97**, pp. 083102-1 – 083102-9, (2005).

Chapter 7

Revised Modification Mechanisms

7.1 Overview

This chapter discusses how the results from the experiments described in chapters 4-6 help elucidate the mechanisms by which femtosecond lasers can be used to cause permanent refractive index changes in glass. The chapter starts by reviewing the current view of how the modification process works; it then discusses several results and how they relate to the underlying mechanisms; finally it concludes by putting forth a revised modification process.

7.2 Current view of femtosecond laser modification mechanisms in glass

The modification mechanisms by which a femtosecond laser can induces a permanent refractive index change in glass were discussed in chapter 2. In brief, it is generally agreed upon that the laser energy is rapidly absorbed through a combination of multiphoton absorption and avalanche photo-ionization. There are two viewpoints regarding how much energy must be absorbed to cause permanent changes within the glass. The more popular view is that enough energy must be absorbed to form plasma within the glass [7.1-7.5]. The second view is that rough damage features that scatter light result within the glass after plasma forms, and that slightly less energy is required to

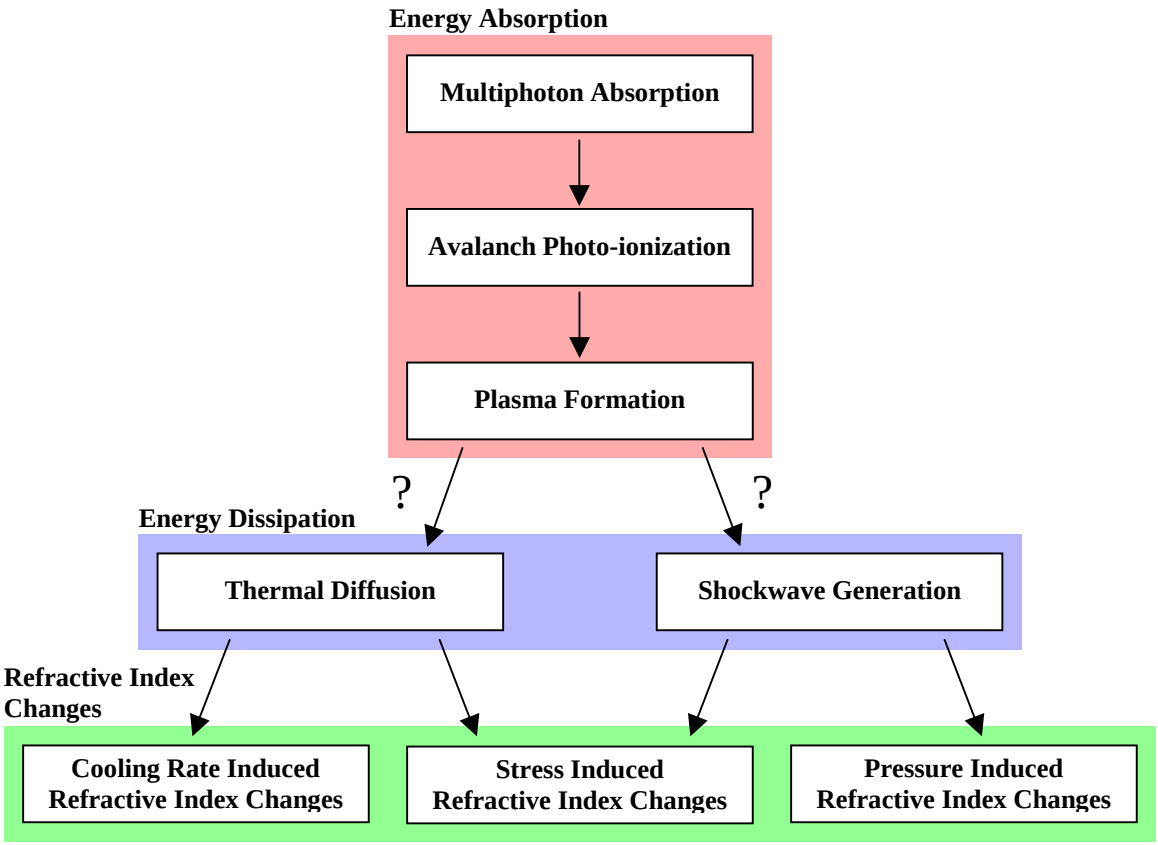

Table 7.1 Current theory of femtosecond laser modification mechanisms. Question marks indicate areas of uncertainty.

cause a controlled change in the material [7.6]. The energy dissipates through either thermal diffusion or shockwave generation, though there is substantial uncertainty regarding which mechanism is dominant. This leads to uncertainty regarding what causes the observed refractive index changes. Thermal diffusion would result in a combination of cooling rate-induced structural changes and stress-induced refractive index changes. A shockwave would result in a combination of pressure-induced structural changes, and stress-induced refractive index changes. Note, any structural changes would also be associated with refractive index changes. These mechanisms are summarized in figure 7.1.

7.3 Important results

Several results were particularly helpful in revising the modification mechanisms; these results are briefly restated here.

Chapter 6 showed that waveguides fabricated in fused silica and soda-lime silicate glasses with a 1 kHz femtosecond laser have different guiding behaviors. They differ in both the location of the waveguides relative to the exposed area and the laser intensity required to create good waveguides relative to the minimum intensity required to cause a noticeable change in the glass. In fused silica good waveguides are formed within the exposed material when using the lowest intensities that can cause a noticeable change in the glass; and higher intensities lead to damage that scatters light, as illustrated in figure 7.2a. In both soda lime silicate glasses low intensities cause a noticeable change but do not result in the formation of waveguides; moderate intensities produce a damaged central region with good waveguides around it; and higher intensities lead to damage that scatters light, as illustrated in figure 7.2b. It is also worth noting that good waveguides form over a larger range of laser intensities in the soda lime silicate glasses than in fused silica. And, that the spatial Raman profiles of individual waveguides in fused silica, which were presented in chapters 4 and 5, showed an increase in the density of the glass within the center of the waveguides.

In chapters 4 and 5, it was observed that two distinct types of fluorescent defects form in fused silica during the laser modification process depending upon the intensity (or pulse

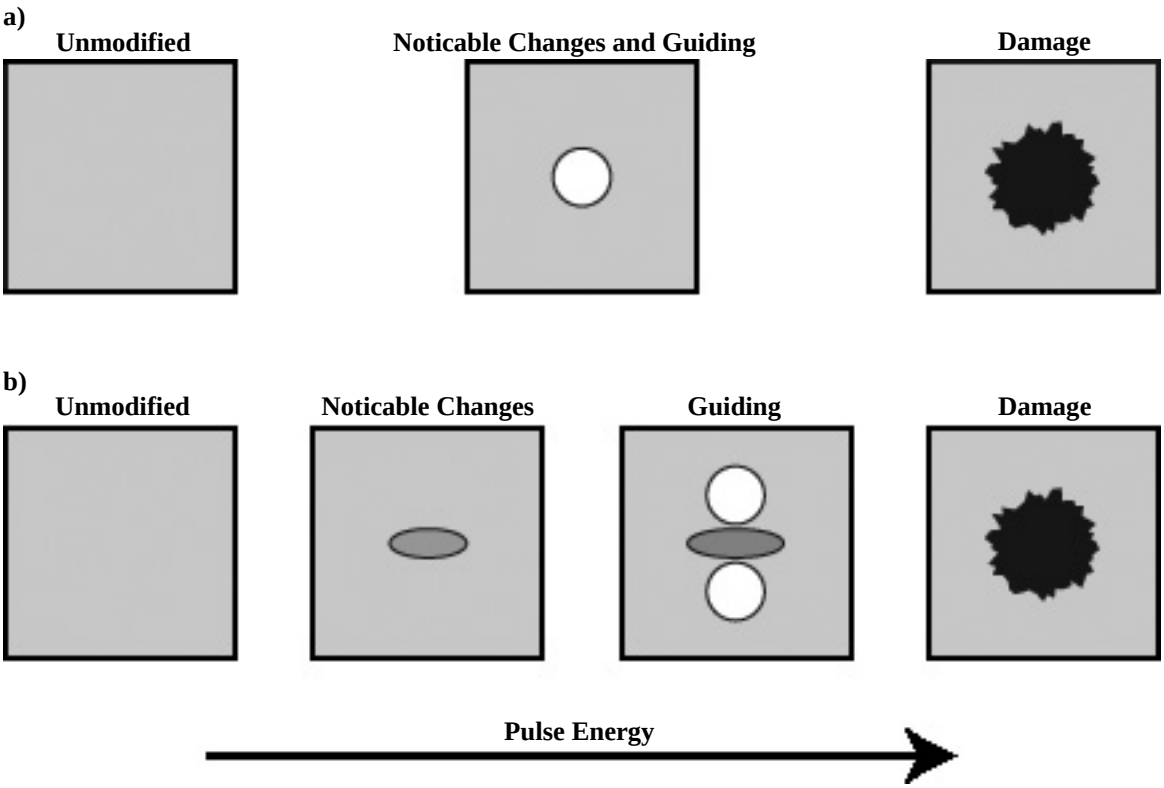

Figure 7.2 A cartoon of the results of laser modification with a 1 kHz pulse repetition rate femtosecond laser in a) fused silica and b) soda-lime silicate glasses as a function of pulse energy. The darker grey regions have a lower refractive index than the bulk glass; the white regions have a higher refractive index than the bulk glass, allowing them to function as waveguides.

fluence) of the writing laser. At low intensities E'_{δ} defects are predominant; at high intensities NBOHC defects are predominant. In chapter 5, it was also observed that two distinct emissions were produced while writing depending upon the intensity of the writing laser. At low intensities a "blue" emission is observed; at high intensities a second "white" emission is also observed. When using a 1 kHz laser, the intensity at which the predominant fluorescent defect type changes and the intensity at which the second emission appears both roughly correlate to the intensity at which damage begins to arise.

These results indicate that there are two regimes in which different modification processes occur, depending on the intensity of the femtosecond laser. At low intensities there is a regime that is characterized by "blue" emissions while writing, the presence of E'_{δ} defects after writing, and the formation of smooth modified lines that function as good waveguides in fused silica. At high intensities there is a regime that is characterized by "white" emissions while writing, the presence of NBOHC defects after writing, and the formation of damaged lines that eventually become voids.

7.4 Revised modification mechanisms

The observations that there are different guiding behaviors in fused silica and soda-lime silicate glasses, and that there is a denser region in the center of waveguides in fused silica favor the rapid quenching model of waveguide formation. In this model, thermal diffusion is the dominant energy dissipation mechanism, and the relationship between the cooling rate and the resulting density of the glass is responsible for the observed refractive index changes. Two factors would contribute to this refractive index change, the changes in the local microstructure and secondary stress effects. For fused silica, the rapid quenching model predicts a greater local density and refractive index in the center of the exposed region, because the density of silica increases with increased cooling rate. For the soda-lime silicate glasses which have a lower density with increasing cooling rate, the rapid quenching model predicts a lower local density and refractive index in the center of the exposed region, with stress-induced increases in the refractive index of the surrounding material. These predictions agree well with the Raman profile and

waveguide coupling results for low pulse energies in our experiments, and with waveguide coupling and refractometry results collected by us and other groups [7.7-7.8]; however these predictions do not explain why damage occurs at higher pulse energies. Thus, it can be concluded that the rapid quenching model controls the formation of waveguides in the low intensity regime, and that a second mechanism is dominant at high intensities.

The results discussed in this dissertation focused on lower intensity writing conditions that produce good waveguides; as such they are of limited utility for explaining the modification process at high intensities. Other groups have conducted extensive investigations of the femtosecond laser modification process at high intensities. Two important features of their results are that they clearly show the formation of plasma within the glass during the modification process [7.9-7.10], and they show the formation of voids at very high intensities [7.11-7.12]. The shockwave generation model, discussed in chapter 2, can explain these results.

Together, the rapid quenching and shockwave generation models fit well with all of the experimental results for low repetition rate (1 kHz) writing. They are incorporated into the following revised modification mechanisms for femtosecond laser writing with low pulse repetition rates, illustrated in figure 7.3. The energy is initially absorbed through a combination of multiphoton absorption and avalanche photo-ionization. For low laser intensities, the glass is heated by each pulse and rapidly cools through thermal conduction between pulses. The resulting refractive index change is determined by the relationship

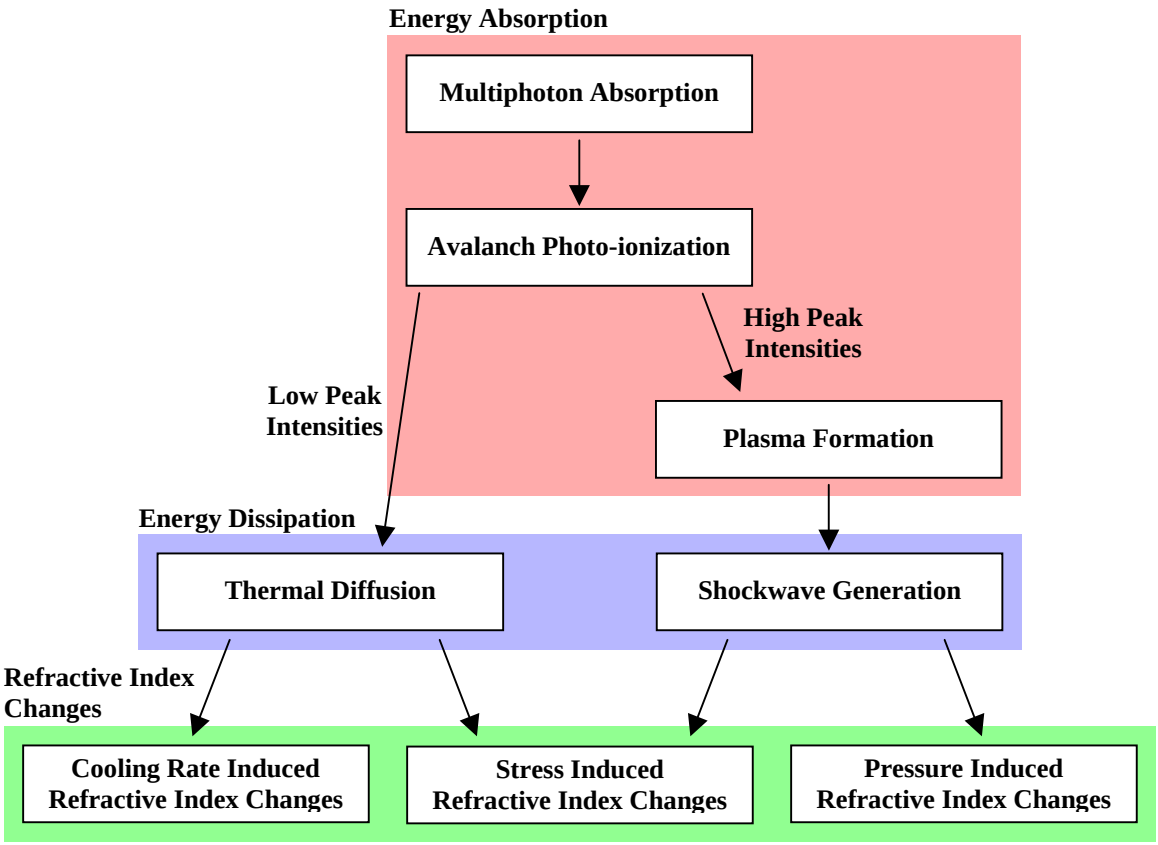

Table 7.3 Revised model of femtosecond laser modification mechanisms.

between the density of the glass and the cooling rate, and by residual stresses caused by this density gradient. For high laser intensities, plasma forms within the glass creating a large charge separation that leads to a coulomb explosion. This results in a shockwave that produces pressure induced refractive index changes with an inhomogeneous redistribution of the material within the modified region, and stress induced refractive index changes in the surrounding material.

For the case of high repetition rate writing in which thermal accumulation occurs, similar divisions likely exist but more information will be required to accurately describe them. Preliminary evidence indicates that the amount of thermal accumulation is at least as important as the pulse intensity. With moderate thermal accumulation a heated region

forms beyond the focal volume of the laser. This region then rapidly cools from the outside in, resulting in good waveguides within glasses similar to the soda-lime silicates. With greater thermal accumulation molten glass persists between laser pulses. The refractive index change associated with the molten glass substantially distorts the focused femtosecond laser resulting in uneven globular structures. There is also some evidence that thermal accumulation retards the generation of damage that scatters light, though more research is necessary to confirm this effect.

References

7.1 S. C. Jones, P. Braunlich, R. T. Casper, X. A. Shen and P. Kelly, "Recent progress on laser-induced modifications and intrinsic bulk damage of wide-gap optical-materials," *Optical Engineering*, **28**, pp. 1039–1068, (1989).

7.2 X. Liu, D. Du, and G. Mourou, "Laser Ablation and Micromachining with Ultrashort Laser Pulses," *IEEE Journal of Quantum Electronics*, **33**(10), pp. 1706-1716, (1997).

7.3 C. B. Schaffer, A. Brodeur and E. Mazur, "Laser-induced breakdown and damage in bulk transparent materials induced by tightly focused femtosecond laser pulses," *Measurement Science and Technology*, **12** 1784–1794, (2001).

7.4 B. C. Stuart, M. D. Feit, S. Herman, A. M. Rubenchik, B. W. Shore and M. D. Perry, "Nanosecond-to-femtosecond laser-induced breakdown in dielectrics," *Physics Review* B, **53**(4), pp. 1749–61, (1996).

7.5 D. Du, X. Liu, G. Korn, J. Squier and G. Mourou, "Laser-induced breakdown by impact ionization in SiO_2 with pulse widths from 7 ns to 150 fs," *Applied Physics Letters*, **64**(23), pp. 3071–3073, (1994).

7.6 C. W. Smelser, S. J. Mihailov and D. Grobnic, "Formation of Type I-IR and Type II-IR gratings with an ultrafast IR laser and a phase mask," *Optics Express*, **13**(14), pp. 5377-5386, (2005).

7.7 J. W. Chan, T. R. Huser, S. H. Risbud and D. M. Krol, "Waveguide fabrication in phosphate glasses using femtosecond laser pulses," *Applied Physics Letters*, **82**(15)**,** pp. 2371-2373, (2003).

7.8 V. R. Bhardwaj, E. Simova, P. B. Corkum, D. M. Rayner, C. Hnatovsky, R. S. Taylor, B. Schreder, M. Kluge, and J. Zimmer, "Femtosecond laser-induced refractive index modification in multicomponent glasses," *Journal of Applied Physics*, **97**, pp. 083102-1 – 083102-9, (2005).

7.9 Z. Wu, H. Jiang, Q. Sun, H. Yang, and Q. Gong, "Filamentation and temporal reshaping of a femtosecond pulse in fused silica," *Physical Review A*, **68**(6), pp. 063820-1 – 063820-8, (2003).

7.10 S. H. Cho, H. Kumagai, K. Midorikawa, "In situ observation of dynamics of plasma formation and refractive index modification in silica glasses excited by a femtosecond laser," *Optics Communications*, **207**, pp. 243-253, (2002).

7.11 D. Ashkenasi, G. Muller, A. Rosenfeld, R. Stoian, I. V. Hertel, N. M. Bulgakova and E. E. B. Campbell, "Fundamentals and advantages of ultrafast micro-structuring of transparent materials," *Applied Physics A*, **77**, pp. 223-228, (2003).

7.12 W. Watanabe, T. Toma, K. Yamada, J. Nishii, K. Hayashi and K. Itoh, "Optical seizing and merging of voids in silica glass with infrared femtosecond laser pulses," *Optics Letters*, **25**(22), pp. 1669-1671, (2000).

Chapter 8

Summary

8.1 Overview

The work discussed in this dissertation explores how femtosecond laser modification of glasses works. Specifically, it focuses on using high spatial resolution confocal fluorescence and Raman spectra spectroscopy to analyze the effects of pulse repetition rate and glass composition on the writing process. These results are then used to explain the femtosecond laser modification process.

8.2 High spatial resolution spectroscopy

In previous studies of large volumes modified by femtosecond lasers, spectra have revealed that the laser modification creates a large concentration of non-bridging oxygen hole center (NBOHC) defects, and causes an increase in the relative concentration of three-membered rings, indicating local densification. We used a confocal microscope with high spatial resolution to collect spectra as a function of spatial position while scanning across individual waveguides (6-10 μm in diameter) and fiber Bragg gratings. The shape of the spatial Raman and fluorescence profiles closely matches the shape of the Gaussian focus used for writing the waveguides; indicating that the greatest densification and defect concentrations are in the

center of the modified region. This result supports the rapid quenching model, which predicts a greater density within the center of waveguides fabricated in fused silica.

There was some concern that the Gaussian Raman and fluorescence profiles were a result of the Gaussian focus of the confocal microscope used to collect the spectra, rather than the focus used to write the waveguides. Spectra collected while scanning across a 2.14 μm pitch fiber Bragg gratings were used to experimentally determine that our confocal microscope has a minimum feature size of less that 1.4 μm. This resolution is fine enough that the waveguide profiles should be an accurate representation of the focus used to create them.

It was also observed that two types of fluorescent defects were present in the fiber Bragg gratings: NBOHC defects with a peak around 650 nm, and self trapped exciton (E'_{δ}) defects with a peak around 540 nm. A review of earlier data revealed that E'_{δ} defects were predominant in many waveguides fabricated using low laser pulse energies, and that NBOHC defects were predominant in waveguides fabricated using high laser pulse energies.

8.3 Effects of changing the pulse repetition rate

It has been reported that using high repetition rate femtosecond lasers results in waveguides that have larger diameters and potentially greater refractive index changes than waveguides fabricated with low repetition rate lasers. It is believed that these effects are the result of thermal accumulation while writing. To test these assertions, we produced waveguides in fused silica using several pulse repetition rates ranging from 1 kHz to 1 MHz and a wide

range of scan speeds; Raman and fluorescence spectra were then collected from the center of each waveguide, and as a function of spatial position scanning across select waveguides.

The spectra collected from the center of each line showed different concentrations of NBOHC defects, E'_{δ} defects, and 3-membered rings depending on the writing conditions. The broad fluorescence band, centered at 650 nm that is associated with NBOHC defects, was the only fluorescence observed in waveguides fabricated at repetition rates higher than 250 kHz. For lower repetition rates NBOHC defects were only observed for waveguides written with higher total doses, where the total dose is determined by the laser repetition rate, the speed at which the sample was moved while writing, and the energy per pulse. An example of this dependence is that for a 1 kHz laser and a scan speed of 20 μm / s, NBOHC defects formed at pulse energies above 1 μJ. Far fewer NBOHC defects were formed with the 1 MHz laser than with the kHz lasers. This could be a result of thermal annealing driven by heat accumulation effects at higher repetition rates, or it could be an effect of the higher repetition rate lasers having less energy per pulse. Self trapped excition (E'_{δ}) defects were dominant for conditions with low total doses, such as using a 1 kHz laser with a scan speed of 20 μm /s and pulse energies less than 1 μJ. We also observed an increase in the intensity of the 605 cm^{-1} Raman peak relative to the total Raman intensity, corresponding to an increase in the concentration of 3-membered rings, and therefore an increase in density, within the lines fabricated with both laser systems. The magnitude of this increase in waveguides fabricated with a 1 MHz laser was nearly twice the increase observed in waveguides fabricated with a 1 kHz laser. This supports the contention that writing with higher repetition rates may result in a greater refractive index change.

The shape of spatial profiles produced from the spectra collected as a function of spatial position while scanning across select waveguides matches the Gaussian focus used to fabricate the waveguides for all conditions. It is of particular interest that there was no variation in the waveguide width for waveguide fabricated with the 1 MHz repetition rate laser and scan speeds ranging from 50 μm / s to 5 mm / s. This indicates that greater thermal accumulation did not lead to an increased waveguide diameter, contrary to observations reported by other groups in other glass systems.

8.4 Effects of changing the glass composition

Work by my predecessor indicated that distinctly different guiding behavior occurs in different materials as a result of femtosecond laser modification. Waveguides written in IOG-1 appear to have a lower refractive index core surrounded by a higher refractive index shell; in contrast the waveguides written in fused silica appear to have a higher refractive index core. Our group proposed that these different behaviors are determined by the relationship between the cooling rate used to produce the glass and the resulting density of the glass. However, IOG-1 and fused silica belong to drastically different glass systems, between which too many material properties change to draw firm conclusions about the validity of our explanation.

To examine the cooling rate dependence, waveguides were fabricated in soda lime silicate glasses with similar compositions of xNa_2O xCaO $(1-2x)SiO_2$ where x = 0, 15, and 20. The

location of the resulting, guiding regions was observed relative to the regions exposed to the 1 kHz femtosecond laser. As expected, waveguides formed in fused silica guided light within the exposed material. In contrast, the waveguides produced in both soda lime silicate glasses exhibit the same behavior our group first observed in IOG-1, in which the waveguides form around but not within a central exposed line. Fused silica has a higher bulk refractive index with increased quenching rate, while both of the soda lime silicate glasses and IOG-1 have lower bulk refractive indices with increased quenching rate. This supports our group's contention that the relationship between the cooling rate and the resulting density of the glass can be used to determine the type of waveguides that will be produced within the glass.

8.5 Revised modification mechanisms

Taken together the results of the experiments discussed in this dissertation indicate that for low laser repetition rates, there are two regimes in which different mechanisms control the femtosecond laser modification process. In both regimes, the laser is absorbed through a combination of multiphoton absorption and avalanche photo-ionization. The resulting modification process depends on how much energy is absorbed. For high energy levels, plasma forms within the glass leading to a coulomb explosion. The resulting shockwave produces stress induced refractive index changes and damage. For low energy levels, the glass cools off rapidly through thermal diffusion. The ensuing refractive index changes are determined by the relationship between the cooling rate used to produce the glass and the density of the glass.